Anisotropic Electronic Transport of the Two-Dimensional Electron System in Al_2O_3/$SrTiO_3$ Heterostructures

Zur Erlangung des akademischen Grades eines
DOKTORS DER NATURWISSENSCHAFTEN
an der Fakultät für Physik am
Karlsruher Institut für Technologie (KIT)
genehmigte

DISSERTATION

von

Karsten Wolff

Institute for Solid State Physics

Reviewer:	Prof. Hilbert v. Löhneysen
Co-Reviewer:	Prof. Matthieu le Tacon
Advisor:	Dr. Dirk Fuchs

Tag der Prüfung – 06.07.2018

"DON’T PANIC!"

The Hitchhiker’s Guide to the Galaxy
Douglas Adams

Abstract

The two-dimensional electron system (2DES) formed at the interface between the two insulating oxides $LaAlO_3$ (LAO) and $SrTiO_3$ (STO), shows many interesting properties like superconductivity, magnetism and tunable spin-orbit coupling (SOC). Heterostructures of aluminum oxide (AO) thin films prepared by pulsed laser deposition on STO substrates form a 2DES as well. In contrast to the epitaxial LAO/STO heterostructures, AO can be deposited in amorphous form, therefore allowing AO film deposition even at room temperature. In addition, AO is chemically robust and can act as surface passivation, protecting the buried 2DES with respect to oxygenation or hydration. These properties make AO/STO very attractive with respect to large scale applications.

The electric field due to polar discontinuity at the LAO/STO interface gives rise to Rashba-type SOC and is expected to have a strong influence on the interfacial conductivity. Nonetheless, doping of STO with oxygen vacancies can also act as a possible source for itinerant charge carriers. An anisotropic striped, filamentary electronic structure due to mesoscopic inhomogeneities has been reported in the 2DES of epitaxial $LaTiO_3$/STO and LAO/STO [1–5]. Possible explanations for the electric inhomogeneity could be extrinsic defects and impurities, or a net surface charge at step edges [6]. Strong Rashba coupling may also lead to charge segregation and intrinsic electronic phase separation, even in flawless, defect free and homogeneous LAO/STO [7]. To gain a better understanding of emerging non-local resistance phenomena in 2DES of STO-based heterostructures, conducting microbridges along different crystallographic directions of (001), (110) and (111)-oriented $Al_2O_3/SrTiO_3$ (AO/STO) heterostructures were prepared and characterized with respect to anisotropic electronic transport.

Independent of the crystal orientation, the temperature dependence of the sheet resistance can be described by phonon mediated electron-electron and impurity scattering. The appearance of weak antilocalization (WAL) below 10 K confirms the two-dimensional nature of the electron system.

For (001) AO/STO, anisotropic contributions to the electronic transport for $T \leq 30\,\mathrm{K}$ are due to dislocations and scattering by step edges. Increasing the number of step edges by increasing the substrate miscut results in a distinct increase of resistance anisotropy

below 30 K, which even allows to manipulate electronic anisotropy in the low-temperature region. The magnetoresistance (MR) is dominated by classical Lorentz scattering for $T \geq 10\,\mathrm{K}$. For $T < 10\,\mathrm{K}$, WAL emerges. Anisotropic contributions to the WAL csn be attributed to the impurity-driven Elliot-Yafet spin-relaxation mechanism. Nevertheless, dominant contributions to WAL are very likely caused by Rashba-type SOC as indicated by measurements of the anomalous magnetoresistance (AMR) for magnetic fields parallel to the conducting interface.

In contrast to (001) AO/STO, the (110) AO/STO heterostructures show anisotropic transport in the complete temperature range. Electronic band structure calculations via linear combination of atomic orbitals in combination with semi-classical Boltzmann theory (carried out by R. Eder, IFP) confirm anisotropic electronic transport as a result of intrinsic electronic band structure. Experimental AMR data could be modeled by theory. Backgating experiments on (110) AO/STO display a strong influence on the AMR behavior, indicating a strong impact of the sheet carrier density and the magnetic field strength on the magnetotransport. The obtained results demonstrate that electronic anisotropy is dominated by intrinsic properties of the 2DES in AO/STO and not due to extrinsic - defect induced - effects as it has been observed in (001) AO/STO. The reason for the negligible defect-induced electronic anisotropy in (110) AO/STO could be related to a more homogeneous distribution of dislocations (note that the isotropic resistance $R_0(5\,\mathrm{K})$ of (110) AO/STO is distinctly larger compared to that of (001) AO/STO), the sample orientation or differences between growth batches of the STO single crystals.

The 2DES formed in (111) AO/STO shows MR comparable to the in-plane MR of (001) and (110) AO/STO. AMR measurements on (111) AO/STO indicate a rather complicated behavior of magnetotransport with respect to in-plane magnetic field orientation. Besides an intrinsic anisotropic electronic behavior, extrinsic electronic anisotropy has to be taken into account alike. This may further complicate the data evaluation. To differentiate and disentangle contributions to the electronic anisotropy, modeling of the electronic transport by theory is needed to obtain a better understanding of the AMR behavior in (111) AO/STO.

Zusammenfassung

Das zweidimensionale Elektronensystem (2DES), das an der Grenzfläche zwischen den beiden isolierenden Oxiden $LaAlO_3$ (LAO) und $SrTiO_3$ (STO) entsteht, zeigt viele interessante Eigenschaften wie Supraleitung, Magnetismus und einstellbare Spin-Bahn-Kopplung (SOC). Heterostrukturen aus dünnen, mit gepulster Laserablation hergestellten, Aluminiumoxid (AO)-Schichten auf STO-Substraten bilden ebenfalls ein solches 2DES. Da AO im Gegensatz zu epitaktischen LAO/STO-Heterostrukturen auch amorph aufgebracht werden kann, ist eine Herstellung der dünnen Schichten auch bei Raumtemperatur möglich. Darüber hinaus ist AO chemisch unempfindlich, passiviert die Oberfläche und schützt dadurch das tiefer liegende 2DES vor Oxidation und Hydration. Diese Eigenschaften machen AO/STO im Gegensatz zu LAO/STO für Anwendungen in industriellem Maßstab interessant.

Das durch die polare Unstetigkeit an der LAO/STO-Grenzfläche erzeugte elektrische Feld hat Rashba-artige SOC zur Folge und lässt einen starken Einfluss auf die Leitfähigkeit der Grenzfläche erwarten. Ebenso kann das STO mit Sauerstoffleerstellen als Quelle für bewegliche Ladungsträger dotiert werden. In der Literatur wurde eine anisotrop gestreifte, faserartige elektronische Struktur aufgrund mesoskopischer Unregelmäßigkeiten im 2DES von epitaktischem $LaTiO_3$/STO und LAO/STO gefunden [1–5]. Mögliche Erklärungen für die elektronischen Unregelmäßigkeiten könnten extrinsische Defekte und Störstellen oder eine verbleibende Oberflächenladung an Stufenkanten sein [6]. Starke Rashba-Kopplung kann zu Ladungsentmischung und zu intrinscher elektronischer Phasentrennung führen. Dies ist selbst in perfekten, defektfreien und homogenenen LAO/STO Systemen möglich. Um ein besseres Verständnis der aufkommenden nicht-lokalen Widerstandsphänomene in den 2DES von STO-basierten Heterostrukturen zu bekommen, wurden leitfähige Mikrobrücken entlang verschiedener kristallographischer Richtungen präpariert und hinsichtlich des anisotropen elektrischen Transports charakterisiert.

Die Temperaturabhängigkeit des Flächenwiderstandes kann unabhängig von der Kristallorientierung durch Elektron-Elektron- und Defektstreuung beschrieben werden. Dabei wird der zweidimensionale Charakter der elektronischen Systeme durch das Aufreten von schwacher Antilokalisierung (WAL) unter 10 K bestätigt.

In (001)-AO/STO werden die anisotropen Beiträge zum elektronischen Transport unterhalb von $T \leq 30\,\mathrm{K}$ durch Versetzungen und Streuung an Stufenkanten verursacht. Eine höhere Anzahl an Stufenkanten durch einen größeren Winkel im Fehlschnitt des Substrates vergrößert so direkt die Anisotropie des Widerstandes unterhalb von 30 K. Dies ermöglicht die Manipulation der elektronische Anisotropie bei tiefen Temperaturen. Der Magnetowiderstand (MR) ist für $T \geq 10\,\mathrm{K}$ durch klassische Lorentz-Streuung dominiert, WAL tritt für $T < 10\,\mathrm{K}$ auf. Anisotrope Beiträge zur WAL konnten der durch Defekte induzierten Elliot-Yafet Spinrelaxation zugeordnet werden. Dabei werden die Hauptbeiträge zur WAL wahrscheinlich durch Rashba-SOC verursacht, worauf Messungen des anomalen Magnetowiderstandes (AMR) für Magnetfelder parallel zur leitfähigen Grenzfläche hinweisen.

Im Gegensatz zu (001)-AO/STO weisen (110)-AO/STO-Heterostrukturen anisotropen elektronischen Transport im gesamten gemessenen Temperaturbereich auf. Berechnungen der elektronischen Bandstruktur durch Linearkombination der Atomorbitale in Verbindung mit semi-klassischer Boltzmann-Theorie (durchgeführt von R. Eder, IFP) bestätigen den anisotropen elektronischen Transport als Folge der intrinsischen anisotropen elektronischen Bandstruktur. Mit dieser Theorie konnten Daten aus AMR-Messungen erfolgreich modelliert werden. Experimente mit einer Gate-Elektrode auf der Rückseite von (110)-AO/STO zeigen einen starken Einfluss des angelegten elektrischen Feldes auf den AMR. Dies weist auf starke Auswirkungen der Ladungsträgerdichte und des magnetischen Feldes auf den Magnetotransport. Die erhaltenen Ergebnisse weisen auf überwiegend intrinsische Ursachen für die Anisotropie des elektrischen Transportes hin, im Gegensatz zu den extrinsischen, durch Defekte verursachten Effekten in (001)-AO/STO. Der Grund für die vernachlässigbare Anisotropie durch Defekte in (110)-AO/STO könnte in einer gleichmäßigen Verteilung der Versetzungen (der isotrope Anteil des Widerstands $R_0\,(5\,\mathrm{K})$ in (110)-AO/STO ist größer als der in (001)-AO/STO), der kristallographischen Orientierung der Probe oder in unterschiedlichen Chargen der Einkristallzucht des STO liegen.

Das 2DES von (111)-AO/STO zeigt MR vergleichbar mit dem planaren MR der (001)- und (110)-AO/STO-Grenzfläche. AMR Messungen an (111)-AO/STO weisen auf ein eher kompliziertes Verhalten des Magnetotransportes hinsichtlich der Orientierung des Magnetfeldes in der Ebene hin. Da neben dem intrinsisch anisotropen elektronischen Verhalten auch die extrinsische elektronische Anisotropie berücksichtigt werden muss, wird die Datenanalyse weiter erschwert. Um Beiträge zur elektronischen Anisotropie zu differenzieren und zu trennen und um ein besseres Verständnis des AMR-Verhaltens in (111)-AO/STO zu erhalten ist eine theoretische Modellierung des elektronischen Transports erforderlich.

Contents

1. Introduction

Low-dimensional electron systems have become a subject of interest in recent times, since they can be formed at the interface of two oxide insulators like $LaAlO_3$ (LAO) and $SrTiO_3$ (STO) [8]. These two dimensional electron systems show many interesting properties like superconductivity, magnetism and a strong influence of external magnetic fields in the electronic transport [2, 9–12]. Theory predicts topologically protected superconductivity [13–15]. An anisotropic electronic structure due to mesoscopic inhomogeneities has been reported for epitaxial $LaTiO_3$ and LAO on STO [1–5]. The electronic inhomogeneities could be due to extrinsic causes like impurities, defects or an inhomogeneous distribution of net surface charges by step edges [6]. Anisotropic electronic transport has been reported in $LaAlO_3/SrTiO_3$ (LAO/STO) heterostructures for different magnetic field directions [16] and different crystallographic orientations where an intrinsic anisotropy of the electronic band structure might be the cause for anisotropic transport [17–19]. These properties make oxide heterostructures an ideal candidate for future electronic devices like all-oxide field effect transistors [20, 21].

Heterostructures formed by aluminum oxide on STO display most of the features mentioned above. In comparison to the well known LAO/STO, the formation of the two-dimensional electron-system (2DES) is not expected to be dominated by electronic reconstruction. Instead, doping via oxygen vacancies is the main cause of conductivity which also should lead to drastically reduced Rashba-type spin-orbit coupling (SOC) with compared to LAO/STO [22–26].

In comparison to LAO, aluminium oxide (Al_2O_3) shows several advantages for sample preparation and handling. Al_2O_3 thin films can be deposited at room temperatures, e.g. via pulsed laser deposition (PLD), while LAO needs temperatures of several hundred degrees Celsius for epitaxial growth. The lower deposition temperatures of Al_2O_3 reduce the risk of unwanted side effects like material intermixing at the interface and also would make future industrial production of oxide heterostructure devices less expensive in terms of energy. Al_2O_3 surfaces are mostly passive to the ambient conditions during sample handling. In the course of this work, the life time of the prepared AO/STO heterostructures could not be exceeded and enabled extensive measurements, while in contrast LAO/STO samples might degrade at ambient conditions.

The goal of this work was to get a better understanding of the anisotropic electronic transport properties of AO/STO heterostructures with respect to its extrinsic and intrinsic causes. For this, AO/STO samples with (001), (110) and (111) substrate orientation were produced and examined with respect to direction- and magnetic-field dependent electronic transport properties. In this chapter, some of the basic principals and models used to explain the electronic transport of the AO/STO heterostructures are introduced.

1.1. The Two-Dimensional Electron System in LAO/STO

At room temperature, Strontium titanate ($SrTiO_3$) has a cubic perovskite structure with transparent to pale yellow appearance. At 105.5 K, STO undergoes a phase transition to a tetragonal structure due to a rotation of the oxygen octahedra [27]. The lattice constant of cubic STO at room temperature is 3.905 Å.

STO is an incipient ferroelectric material at the verge of a ferroelectric phase transition which is suppressed by quantum fluctuations [28]. Hence, the dielectric constant is rather high and strongly temperature dependent, ranging from 300 at room temperature to around 24000 at 5 K [29–31]. The dielectric constant can be altered by the application of pressure or epitaxial strain. Strained STO films can become ferroelectric even at room temperature [32, 33].

Undoped bulk STO is insulating with an indirect band gap of 3.25 eV and a direct band gap of 3.75 eV [34]. STO becomes conducting when it is doped, either by substituting Ti^{4+} or Sr^{2+} by, e.g. Nb^{5+} or La^{3+}, respectively. Oxygen deficient STO also becomes conducting. Band structure calculations by linear combination of atomic orbitals tend to give lower values of the band gap than experiments [35, 36], but it is clear that the minimum of the conduction band is at the Γ-point. The orbitals relevant for the doping induced conductivity are the Ti-3d orbitals [37]. Their degeneracy is lifted by the cubic crystal field.

Crystal field splitting results in the doublet of $d_{3z^2-r^2}$ and $d_{x^2-y^2}$ orbitals (referred to as e_g orbitals) and the triplet of the d_{xy}, d_{yz} and d_{zx} orbitals (the t_{2g} orbitals, see Figure 1.1). Spin-orbit coupling and the tetragonal transition lift the degeneracy of the t_{2g} orbitals by 18 meV and 1.54 meV [38, 39]. Itinerant electrons from Ti^{3+} states usually populate the t_{2g} orbitals [40, 41].

At the interface between two insulating oxides, i.e. LAO and STO, such a 2DES can be formed. LAO has a rhombohedrally distorted perovskite structure with a pseudo-cubic (perovskite) lattice parameter of 3.787 Å at room temperature [42].

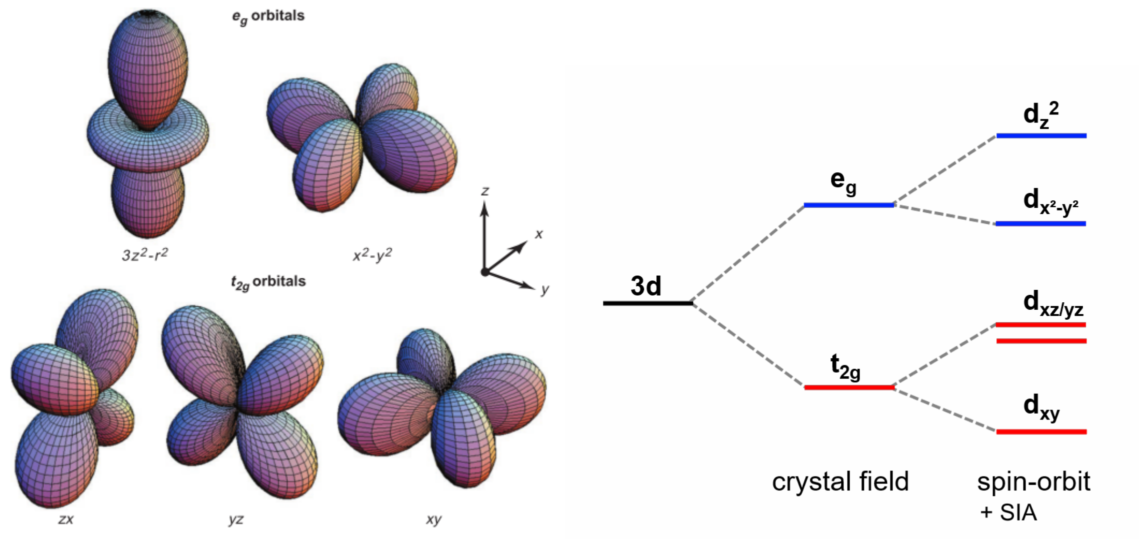

Figure 1.1.: Symmetry of the five d-orbitals of Ti. The cubic crystal field and SOC and the structure inversion asymmetry (SIA) at the interface lift the degeneracy of the two e_g and three t_{2g} orbitals. Reproduced from [39].

In order to consider an electrical conducting system as two-dimensional, one of its spatial dimensions (commonly defined as z) has to be of the order of or smaller than the electron mean free path $\langle l_m \rangle = \tau_m \cdot v_F$ of the itinerant electrons. Hereby the Fermi velocity in two dimensions is given by $v_F = \frac{\hbar}{m}\sqrt{2\pi n}$, where n is the charge carrier density and m their effective mass. τ_m is the mean relaxation time.

For LAO/STO three possible doping mechanisms for the formation of a 2DES are discussed: electronic reconstruction due to a polar mismatch of the constituent materials, doping via oxygen vacancies, and La/Sr intermixing at the interface [23, 24, 43].

The electronic reconstruction is shown in Figure 1.2. In this model, it is assumed that LAO layers with an alternating net charge are placed on top of the neutral layers of STO. Fixed charge distribution leads to a build up of potential with increasing thickness of the LAO film. To avoid this scenario of the so called *'polar catastrophe'*, the charges at the atomically sharp interface have to be redistributed. In contrast to many semiconductor structures, in oxide heterostructures it is energetically favorable to transfer charge carriers instead of rearranging the ionic structure.

The transfer of half an electron per surface unit cell depicted in Figure 1.2 should ideally lead to a charge carrier concentration of $n_s = 3.3 \times 10^{14}\,\mathrm{cm}^{-2}$ for TiO-terminated (001) LAO/STO heterostructures. In contrast, SrO-terminated structures result in hole doping due to the transfer of positive charge, but the holes are found to be localized in deep Sr-derived states [8].

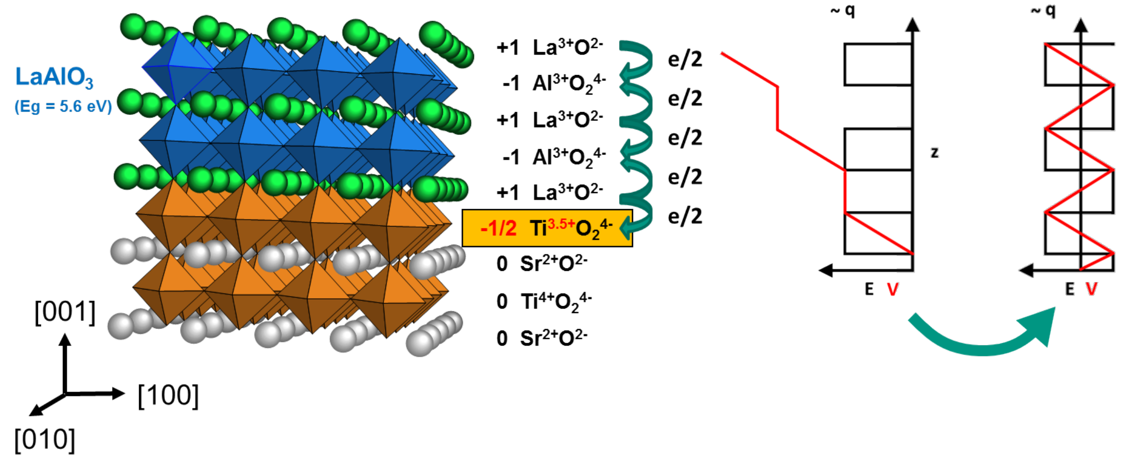

Figure 1.2.: Schematic drawing of the electronic reconstruction in the LAO/STO heterostructure. Half an elementary charge per surface unit cell is transferred from the top to the interface. This prevents a potential build-up (*'polar catastrophe'*) an leads to the reconstructed potential shown on the right side [8].

The band offset between LAO and STO used for TiO-terminated STO can be further minimized by transferring an extra 1/4 electron per surface unit cell to the TiO interface in combination with the addition of 1/8 oxygen vacancy to the SrO layer underneath. A critical thickness of four LAO monolayers is needed to build up a potential large enough to make the system conducting by the charge transfer [9].

The process of doping via oxygen vacancies in oxide heterostructures has been described first in 2011 by Chen et al. [23, 24]. As represented in Figure 1.3, there are two possibilities of introducing oxygen vacancies into a STO substrate. Either via chemical redox-reactions or by heating the STO substrate in an oxygen deficient atmosphere, for example during LAO film deposition. For both ways a well defined conducting interface can be obtained [26, 44]. The conducting interface has a thickness of about 1–2 nm and becomes superconducting at temperatures of $T \leq 300$ mK [8, 25]. The doping via redox-reactions or oxygen vacancies gives the possibility to use also amorphous materials as topping layers, such as amorphous Al_2O_3. In contrast to 2DES caused by polar mismatch, these systems are expected to display significantly smaller electric fields at the interface which may strongly influence electronic transport.

Usually both doping mechanisms, i.e., reduction of Ti^{4+} via redox reaction or oxygen deficiencies, are present in a system, for example when Al_2O_3 is deposited on STO in oxygen deficient atmosphere. At elevated temperatures Al_2O_3 grows with an oxygen deficient

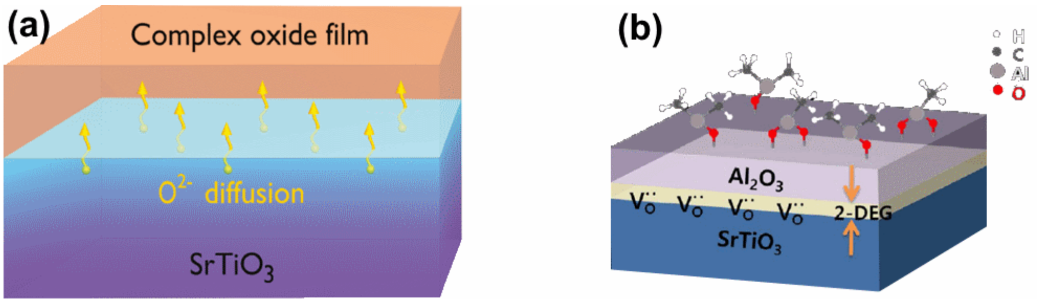

Figure 1.3.: Doping mechanisms for the STO surface by the introduction of oxygen vacancies. (a) Scheme for O^{2-} diffusion from the interface into the oxygen depraved top layers. (b) The reduction of the interface via chemicals. Here, the top layers can act as catalyst and after the reduction process as chemical barrier [23, 24].

cubic Spinel structure (γ-Al_2O_3) on (001) STO. γ-Al_2O_3 has a weakly polar layered structure [45], which may lead also to electronic reconstruction. Usually, intermixing effects due to ion bombardement during film deposition [46] can be be ruled out mostly by transmission electron microscopy (TEM) analysis of the interfaces (see Figure 2.5).

1.2. Electronic Transport in LAO/STO

The conduction electrons of the Ti 3d orbitals display rather strong Coulomb interaction and thus behave more like a two-dimensional electron liquid than a gas [47]. At the interface of the canonical LAO/STO system, the band structure differs from bulk doped STO. Due to the broken structural symmetry at the interface, the d_{xy} subband is shifted down by around 250 meV compared to the bulk. This results in electronic transport dominated by light d_{xy} and heavier d_{xz} and d_{yz} bands [40, 48]. Figure 1.4 (b) displays the band line-up at the interface and shows the electronic band structure in the vicinity of the Γ-point, calculated with *ab-initio* methods [49].

Spin-orbit interaction (SOI) lifts the degeneracy of the *d* orbitals and leads to a mixing of the orbital character. The band filling strongly depends on the charge carrier density. A Lifshitz transition is observed for critical charge carrier densities of $n_c \approx 1.7 \times 10^{13}\,\mathrm{cm}^{-2}$ [41]. For lower doping, the d_{xy} orbitals and are preferentially filled [50]. For higher charge carrier densities ($n > n_c$), the heavier $d_{xz/yz}$ orbitals are populated while the d_{xy} display rather strong Coulomb interaction [40], resulting in an effective one-type charge carrier transport.

The magnetoresistance (MR) is defined as $MR = [R_s(0) - R_s(B)]/R_s(0)$, the relative change of the sheet resistance in a magnetic field. For magnetic fields applied perpendicular to the conduction plane of a 2DES, there are three relevant magnetoresistive effects: ,

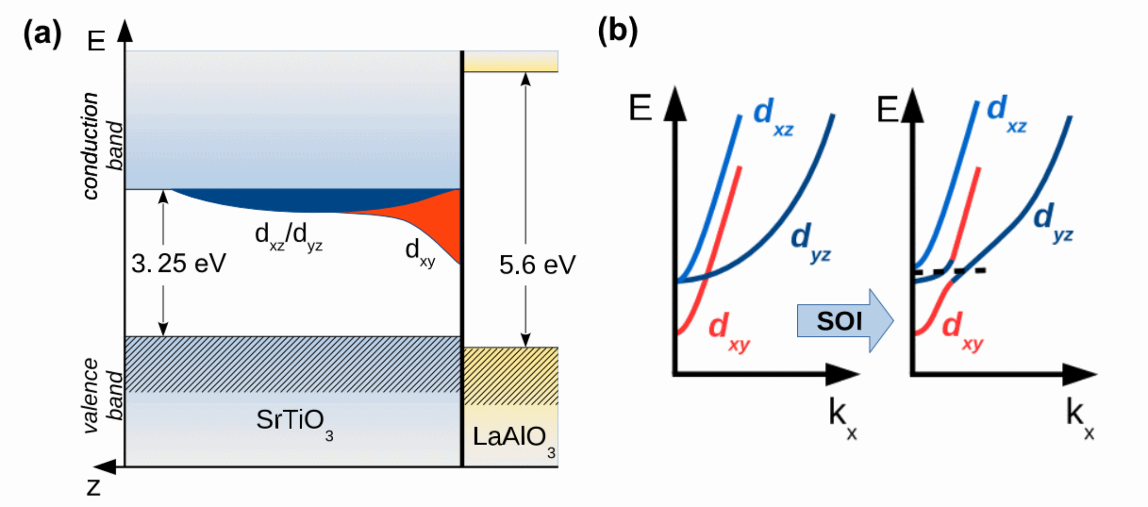

Figure 1.4.: Band structure of the 2DES formed at the LAO/STO interface. (a) The interface after charge transfer from the LAO layers to the d_{xy} and $\mathrm{d}_{xz/yz}$ orbitals. (b) The band splitting due to broken mirror symmetry at the interface and a further lifting of the degeneracy through SOC leading to band mixing. Reproduced from [51].

quadratic *MR*, weak localization (WL) or weak antilocalization (WAL) effects [52] and a linear *MR*.

The positive quadratic magnetoresistance due to Lorentz scattering follows the well known empirical Kohler rule which describes the as a material-dependent function of the magnetic field and the zero-field resistance ρ_0 [53, 54].

$$\frac{\Delta\rho}{\rho_0} = F\left(\frac{B}{\rho_0}\right), \tag{1.1}$$

This normal magnetoresistance has its origins in a lowered effective mean free path for the transport electrons. Their probability for scattering events rises with increasing transversal magnetic fields because this induces a cyclotron motion, thus the total carrier path gets longer [55]. In a single-band model with cubic symmetry (the conduction tensor $\hat{\sigma}$ is treated as scalar), no magnetoresistance is to be found, since the Lorentz force is compensated by the build-up of a Hall field.

A simple model with at least two bands taking part in the conduction process, is needed to describe quadratic *MR*. The current J can be treated as sum of two partial currents, one for each band:

$$J = J_1 + J_2 \tag{1.2}$$

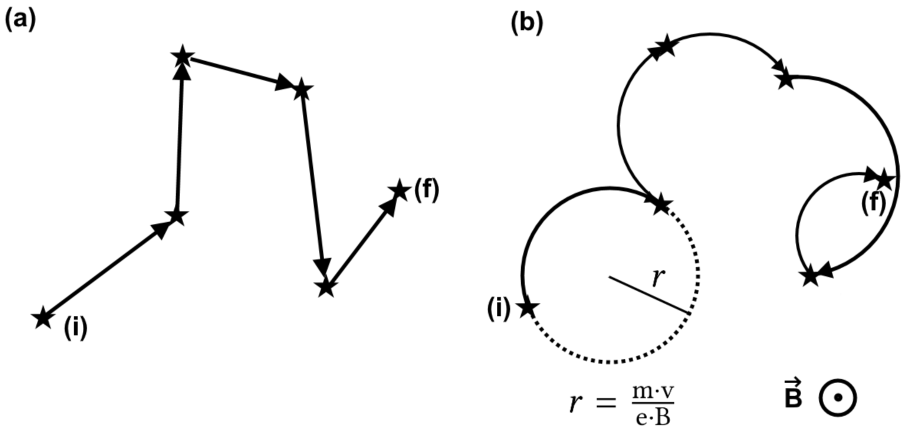

Figure 1.5.: Exemplary trajectory of a single electron along a conductor without (a) and with a magnetic field perpendicular to the net path (b), causing longer ways and thus a higher probability for scattering events.

For each current ($i = 1, 2$) the electric field E is given by (following the Boltzmann equation):

$$\boldsymbol{E} = \rho_0 J_i + \frac{e\tau_i}{m_i} \left(\boldsymbol{B} \times \rho_0 \boldsymbol{J_i} \right), \tag{1.3}$$

where e is the elementary charge, τ the scattering time and m the effective mass. Putting Equation 1.2 and Equation 1.3 together into the relation of the longitudinal electric field and the current, $\rho = (J \cdot E)/J^2$, results in:

$$\frac{\Delta\rho}{\rho_0} = \frac{\sigma_1 \sigma_2 \left(\frac{e\tau_1}{m_1} - \frac{e\tau_2}{m_2} \right)^2 B^2}{(\sigma_1 + \sigma_2)^2 + \left(\frac{e\tau_1}{m_1}\sigma_1 + \frac{e\tau_2}{m_2}\sigma_2 \right)^2 B^2} \tag{1.4}$$

which resembles the Kohler form. Hereby $\Delta\rho = \rho(B) - \rho_0$ and $\rho_0 = \rho(B = 0)$. According to this equation, $\Delta\rho$ is always positive and quadratic for small fields and shows the tendency to saturate at large magnetic fields. The saturation is reached when the electron mean free path takes on closed cycles on the Fermi surface. For some materials, crystallographic directions with open paths across the Fermi surface are possible. These directions show no saturation. In compensated metals with two charge carriers only differing by sign and similar in mobility and concentration no saturation is expected likewise. For these two special cases, Equation 1.4 simplifies to a simple quadratic dependence of $\Delta\rho$.

The Zeeman corrections to the *MR* are described by the Hamiltonian

$$H_Z = \frac{e\hbar}{2m_0}\boldsymbol{\sigma} \cdot \boldsymbol{B}, \tag{1.5}$$

where $\boldsymbol{\sigma}$ are the Pauli spin-matrices and $\boldsymbol{B}$ is the magnetic field, which in the presence of an electric field includes contributions of $B_{el} = \vec{p}(\boldsymbol{k}) \times \vec{E}/2mc^2$ [56]. This leads to a field-dependent spin-splitting of the conduction bands and can lead to a negative MR for sufficiently large magnetic fields caused by a drastic reduction of interband scattering.

The linear magnetoresistance (LMR) recently gained a lot of interest again, since measurements in immense magnetic fields above 50 T still show linear behavior and no signs of saturation at all [57]. The effect can be measured at rather high temperatures ($T \geq 100\,\mathrm{K}$) and seems to be independent of the carrier mobility [58]. An explanation of LMR by quantum effects as provided by Abrikosov [59] is only valid for $\hbar\omega_c \gg \mathrm{k_B}T$, where ω_c is the cyclotron frequency and T the temperature [60]. This leads to fluctuations in the conductance and can be treated as an inhomogeneous resistor network, which for an increasing number of resistors ($\mathrm{n} \longrightarrow \infty$) leads to a linear magnetoresistance for sufficiently large B [61, 62].

The critical field for the transition of the quadratic behavior of the MR at low fields to the linear behavior at high fields scales with $1/\mu_h$, the inverse of the hall mobility [58]. In transport regimes where electron-phonon interactions dominate, it was found that the distribution of disorder in the heterostructure of the 2DES is not important as long as the mean free path of the electrons is smaller than the size of the inhomogeneities. In two-dimensional systems, LMR has been found to be symmetric with respect to the sign of the applied transversal magnetic field which also excludes Hall contributions [63].

1.3. Rashba Spin-Orbit Coupling

In this chapter, a brief summary of the Bychkov-Rashba SOC [64–66] (mostly referred to as Rashba-SOC) is given. The Pauli spin-orbit Hamiltonian describes the influence of atomic SOC on atomic spectra from the point of a relativistic approximation of the Dirac equation [67]. In crystalline solids, this usually leads to the splitting of degenerate valence bands according to the orbital momentum of the corresponding electrons, even at an external magnetic field of $B = 0$ (see Figure 1.4).

$$H_{SO} = -\frac{\hbar}{4m_0^2c^2}\boldsymbol{\sigma} \cdot \boldsymbol{p} \times (\nabla V_0) \tag{1.6}$$

Here, $\boldsymbol{\sigma} = (\sigma_x, \sigma_y, \sigma_z)$ is the vector of the Pauli spin matrices, $\boldsymbol{p}$ the momentum operator and V_0 the Coulomb potential of the atom. This kind of SOI is independent of the crystal symmetry and present in all types of crystals. Fourth-order perturbation theory including the Zeeman effect and the so called *Darwin* term for non-zero probability of s electrons at the core gives the full Pauli Hamiltonian [68]:

$$H = \frac{p^2}{2m_0} + V + \frac{e\hbar}{2m_0}\boldsymbol{\sigma} \cdot \boldsymbol{B} - \frac{e\hbar}{4m_0^2c^2}\boldsymbol{\sigma} \cdot \boldsymbol{p} \times \boldsymbol{\mathcal{E}} - \frac{e\hbar^2}{8m_0^2c^2}\nabla \cdot \boldsymbol{\mathcal{E}}, \tag{1.7}$$

where $\boldsymbol{\mathcal{E}} = \nabla V/e$ is the electric field. The third term gives the Zeeman corrections, the fourth term the Pauli SOC and the fifth term the so called Zitterbewegung described by the Darwin term.

Systems with broken symmetry are classified according to the cause of the asymmetry: bulk inversion asymmetry (BIA), occurring for crystals which do not have an inversion symmetric crystal structure like the zinc-blende structure [69] and structure inversion asymmetry (SIA) of the confining potential which in the lowest order can be characterized by an electric field, for example found at the two-dimensional electron-liquid (2DEL) interface of heterostructures. Both effects cause a spin splitting even for $B = 0$.

While BIA is expected to be reduced at the interface in comparison to the bulk [70], the potential build-up at the interface of LAO/STO or similar heterostructures results in SIA. Microscopic asymmetries of atoms at the interface are expected to contribute to the $B = 0$ spin splitting, yet to a rather small extent [71]. On the other hand, SIA leading to Rashba-type SOC is experimentally accessible and may influence or even dominate electronic transport at the interface of oxide heterostructures [72].

The Rashba-type spin splitting for SIA in a 2DES is given by

$$H_R = \alpha \cdot \boldsymbol{\sigma} \left(\boldsymbol{p} \times \hat{e_z}\right), \tag{1.8}$$

where α is a constant which depends on the properties of the interface and determines the strength of the Rashba SOC [73]. $\hat{e_z}$ is a unit vector perpendicular to the interface [65, 66]. In STO-based heterostructures, there is no BIA, the perovskite structure is inversion symmetric [74, 75] and thus the focus will be on Rashba type SOC caused by SIA.

The polar-catastrophe and polar-discontinuity model explained in section 1.1 gives rise to an electric field oriented perpendicular to the interface. The strength of this electric field depends not only on the polar layered structure, but also on the growth conditions and the thickness of the thin film and its defect structure [76, 77]. Thus, the achieved charge carrier densities are usually well below the ideal case of 0.5 electrons per unit cell.

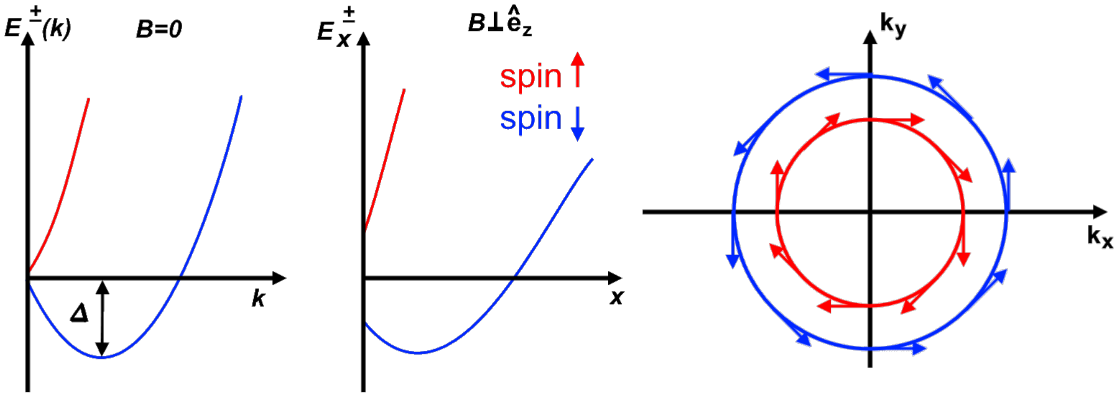

Figure 1.6.: Spin split dispersion according to Bychkov and Rashba [65] for $B = 0$ and for a magnetic field parallel to the interface.

The Rashba-type SOI strongly influences electronic transport for magnetic fields parallel to the plane of the conducting interface of a heterostructure. The spin-splitting of the conduction bands [78] (see Figure 1.6) leads to a lower electron-electron scattering rate of the conduction electrons for the magnetic field oriented perpendicular to the current directions, $\boldsymbol{B} \perp \boldsymbol{I}$, thus increasing the conduction [79]. This behavior is also reported in the LAO/STO system with strong Rashba coupling [80, 81].

1.4. Weak (Anti-) Localization

Rashba-type SOC has a strong effect on the diffusive transport of two-dimensional conducting systems, which at low temperatures are dominated by WL [82]. The Rashba SOC plays an important role for spin relaxation processes influencing the WL. The WL arises from a quantum statistical instead of a classical description for self-crossing paths possible of the moving charge carriers [83, 84]. Thus, at this crossing points, the probability that after a certain time the charge carrier returns to its previous position is finite. Assuming time-reversal symmetry, the charge carrier can also return in the reverse sequence of scattering events.(see Figure 1.7).

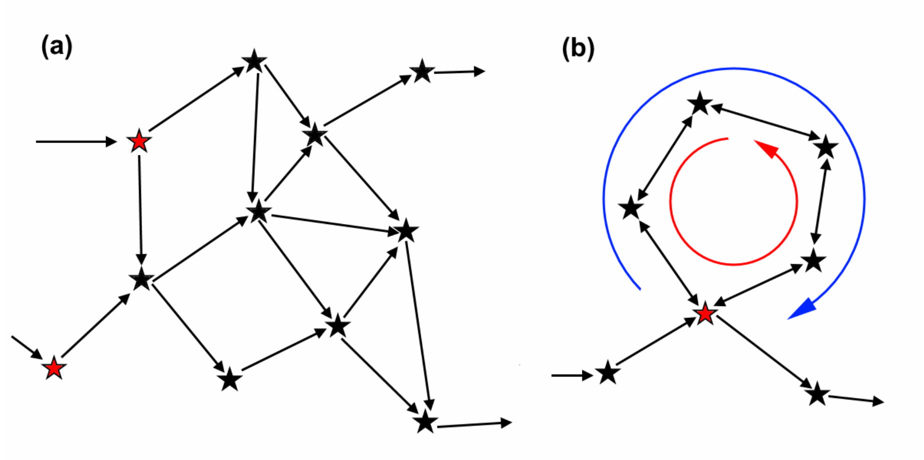

Figure 1.7.: (a) Electrons have an infinite amount of possible trajectories to get from one point to another, including self crossing-paths. Thus there is a probability for an electron to return to the crossing point via a closed loop (b).

In the classical diffusive picture, the intensities of an electron going the closed path in both directions would add up and simply contribute to the total probability to return to the origin. If the electrons quantum nature is considered, interference of the amplitudes for all closed paths have to be taken into account. The amplitudes of the electrons wave-function of each direction interfere positively at the origin and thus the return-probability is doubled in comparison to the classical picture, leading to a decrease of the conductance [85]. If the two partial waves of the electron, one for each path direction, pick up different phases, destructive interference appears and leads to only half the probability for returning to the origin as shown in Figure 1.8. This gives a rise in conductivity and is referred to as weak antilocalization (WAL)[72, 86].

The WL gives a logarithmic rise in resistance with decreasing temperature as a precursor to the fully localized state at $T = 0$. WL is sensitive to inelastic, spin-orbit, paramagnetic impurity or electron-electron scattering [87, 88]. The quantum mechanical description of the diffusive transport is only valid within the limit of phase coherence for the electrons, which requires the phase coherence time τ_ϕ to be larger than, e.g., the time scale for spin-orbit scattering, $\tau_\phi \gg \tau_{so}$ [85, 89, 90]. τ_{so} is the time it takes for an electron to acquire a phase shift of 360° from spin-orbit interaction. Depending on the phase difference between the forward and backward returning path of the electron, the probability to find it at its origin is raised or lowered which directly leads to higher or lower resistance.

An applied magnetic field can suppress the WL by the Aharonov-Bohm-effect [91]. Depending on the direction of the path, the electrons may gather opposing phases from

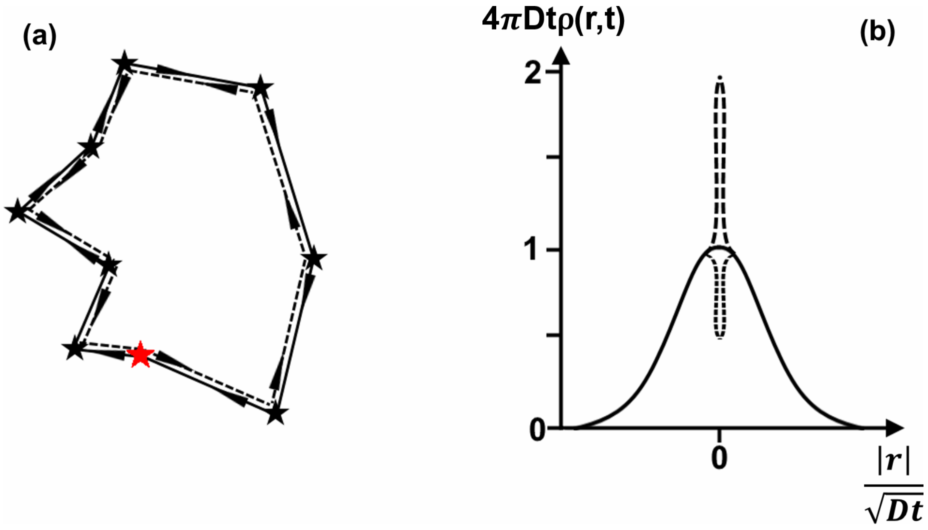

Figure 1.8.: (a) Diffusion path of a conduction electron propagating in both directions (time reversal symmetry), resulting in a doubled probability to return to its origin of quantum diffusion. (b) The probability distribution for an electron starting at $r = 0$ and $t = 0$. The classical case is given by solid line. as solid line. Quantum diffusion gives the upper peak (deviations from classical behavior are shown by dashed line) with twice the return probability, while strong spin orbit scattering leads to WAL with only half the return probability (deviations from classical behavior are shown by dotted line) [84].

the vector potential of the magnetic field [92]. To suppress WL by destructive interference a field of at least h/e has to be inclosed by the path, under consideration of the possible closed paths getting smaller with increasing B.

Maekawa and Fukuyama developed in 1981 a model to describe WL phenomena in 2DES including SOC, Zeeman effect and impurity scattering [87]. According to this model in first-order perturbation theory, the Hamiltonian given in Equation 1.7 reduces to (with $k_f = \hbar = 1$):

$$\begin{aligned} H = {} & \frac{1}{2m}\left(\boldsymbol{p} + \frac{e}{c}\boldsymbol{A}\right)^2 + \boldsymbol{V} \\ & + \sum_l \left[1 + \frac{1}{4m^2c^2}\left(\boldsymbol{p} + \frac{e}{c}\boldsymbol{A}\right)\boldsymbol{\sigma} \times \boldsymbol{\nabla}\right] \times u\left(\boldsymbol{r} - \boldsymbol{R}_l\right) + \frac{g}{2}\boldsymbol{B} \cdot \boldsymbol{\sigma}, \end{aligned} \tag{1.9}$$

where g is the g-factor of the electrons and $u\left(\boldsymbol{r} - \boldsymbol{R}_l\right)$ the potential of an impurity located at $\boldsymbol{R}_l$. The relevant relaxation times are given by

$$\tau^{-1} = \tau_\phi^{-1} + \tau_{so}^{-1} + \tau_s^{-1}, \tag{1.10}$$

with the spin-orbit relaxation time τ_{so} and the magnetic scattering time τ_s. The diffusion constant in d dimensions is given by $D = v_F^2\tau/d$, where v_F is the Fermi velocity. The corresponding length scales are given by $L_x = \sqrt{D \cdot \tau_x}$ and the corresponding magnetic field strengths are

$$B_x = \frac{\hbar}{4e \cdot D\tau_x}. \tag{1.11}$$

For the two-dimensional case of AO/STO heterostructures, the magnetic scattering can be neglected and the remaining parameters can be treated as inelastic (impurity) scattering and spin-orbit scattering.

Caviglia et al. simplified the model given by Maekawa and Fukuyama. In the limit of $B < B_{so} = \frac{\hbar}{4e \cdot D\tau_{so}}$, they give the following form for the first-order corrections $\Delta\sigma$ to the conductance in a magnetic field perpendicular to the conducting plane:

$$\begin{aligned}\frac{\Delta\sigma(B)}{\sigma_0} &= \Psi\left(\frac{B}{B_i + 2B_{so}}\right) \\ &+ \frac{1}{2\sqrt{1-\gamma^2}}\Psi\left(\frac{B}{B_i + B_{so}\left(1+\sqrt{1+\gamma^2}\right)}\right) \\ &- \frac{1}{2\sqrt{1-\gamma^2}}\Psi\left(\frac{B}{B_i + B_{so}\left(1+\sqrt{1-\gamma^2}\right)}\right).\end{aligned} \tag{1.12}$$

Ψ stands for the function $\Psi(x) = \ln(x) + \psi(1/2 + 1/x)$ where ψ represents the digamma function and $\sigma_0 = e^2/\pi h \approx 1.2 \times 10^{-5}$ S is the universal value of conductance. The Zeeman correction is given by $\gamma = g\frac{\mu_B}{4eD}\frac{B}{B_{so}}$. The g-factor itself depends on the electric field at the interface [93, 94]. The strength of the Rashba SOC can be estimated by $\alpha = \frac{\hbar^2}{2L_{so}m^*}$, where for LAO/STO m^* has been estimated to around $3m_0$ [35, 95–97].

For a magnetic field direction parallel to the conducting interface and diffusive electron scattering only at the walls of the confining potential ($d \ll \lambda_{mfp}$), closed paths for which the electron returns to its origin do not inclose magnetic flux (see Figure 1.9). Thus, the electrons do not acquire different phases along their path under time reversal symmetry. For this so called in-plane field configuration, the resistance is still sensitive to Zeeman contributions.

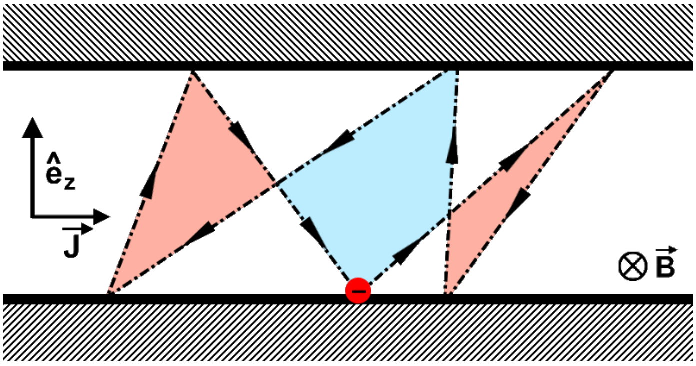

Figure 1.9.: An electron that only scatters diffusive at the walls of its confining potential does not inclose any magnetic flux on its returning path to the origin [89]. The areas inclosing positive and negative flux (red and blue) are of the same size. The striped areas represent the confining potential.

1.5. Spin-Relaxation Processes

Aside from the Aharonov-Bohm effect responsible for the rise of WAL, spin-relaxation mechanisms contribute to WAL by lthe enhancement of destructive interference of the electron wave due to spin disorder. The three most important mechanisms for spin relaxation are the Bir-Aronov-Pikus (BAP) mechanism [98], the D'yakonov-Perel (DP) mechanism [99] and the Elliott-Yafet (EY) mechanism [100, 101]. Besides those, minor contributions to spin relaxation may exist due to interaction of the electron spins with the nuclear spins. Magnetic scattering due to magnetic impurities will be neglected here. A detailed review of the spin-relaxation processes is given by Žutić, Fabian, and Das Sarma in 2004 [102], Figure 1.10 compares the DP and EY mechanisms.

The BAP spin relaxation occurs mostly in heavily p-doped semiconductors where electrons scatter on occupied hole states. It describes spin-flip scattering due to an exchange interaction between electrons and holes which can be seen as strong local fluctuations of the effective magnetic field. This strongly depends on the state of the holes. The relevant Hamiltonian is given by

$$H = A\mathbf{S} \cdot \mathbf{J}\delta(\boldsymbol{r}) \tag{1.13}$$

where A depends on the exchange between valance states, $\mathbf{S}$ and $\mathbf{J}$ are the spin operator for electrons and holes, respectively, and $\boldsymbol{r}$ is the difference of the coordinates of the electron and the hole. Since this effect requires high p-doping and very low temperatures, it is not relevant for 2DES of metal-oxide heterostructures and is only mentioned to complete the overview of spin relaxation mechanisms.

The DP mechanism [99] describes the spin-relaxation in systems spin-splitting due to spin-orbit interactions dominated by inversion asymmetry. In heterostructures like LAO/STO or AO/STO this is the case due to the structural inversion asymmetry at the interface, with the electric field perpendicular to the interface causing Rashba SOC. The spins precess around the axis of their local magnetic field direction given by $B_{loc} = \vec(B) + (\vec{p}(\boldsymbol{k}) \times \vec{E}/2mc^2)$. The precession frequency Ω is directly related to the strength of the (Rashba-) SOC:

$$\begin{aligned} H &= \alpha\hbar\,\boldsymbol{\sigma} \cdot (\boldsymbol{k} \times \boldsymbol{n}) \qquad (1.14) \\ &= \frac{1}{2}\hbar\boldsymbol{\sigma} \cdot \boldsymbol{\Omega(k)}, \end{aligned}$$

where $\boldsymbol{k}$ is the wavevector of states in the conducting channel. The orientation of the precession axis is momentum dependent and thus momentum-changing scattering events also change the spin orientation. This gives rise to a momentum-dependent dephasing of the spins, causing a randomization of the spin orientation. Within the momentum relaxation time τ_p the electrons spin precesses around the intrinsic field by an angle $\delta\phi = \Omega_{av}\tau_p$ before being scattered into another momentum state. The change of the spin phase can then be treated as a random walk, which after a time t has reached t/τ_p steps. The total phase acquired during this walk is given by $\phi(t) \approx \delta\phi\sqrt{t/\tau_p}$. If τ_{so} is defined as for which $\phi(t) = 1$, the inverse spin-relaxation time $1/\tau_{so}$ is proportional to the momentum-relaxation time τ_p:

$$1/\tau_{so} = \Omega_{av}^2 \cdot \tau_p. \qquad (1.15)$$

According to the Drude model the electron mobility is proportional to the momentum relaxation time , $\mu \propto \tau_p$. Taking into account the connection between B_{so} and τ_{so} given by Equation 1.11, in a system with dominating DP spin-relaxation B_{so} is expected to be proportional to the Hall mobility, thus $B_{so} \propto \mu$. The DP mechanism is most relevant for high electron mobility systems.

The EY mechanism describes spin-relaxation due to spin-flipping momentum-scattering events. Elliot [100] stated in 1954 that under SOC induced by lattice ions, conduction-electron spins can relax by momentum scattering on non-magnetic impurities or phonons. In 1963, Yafet [101] expanded the ion-lattice SOI for band structure systems. Combining this with the mechanism described by Elliot gives rise to a consistent picture of phonon- or impurity-induced spin relaxation [102].

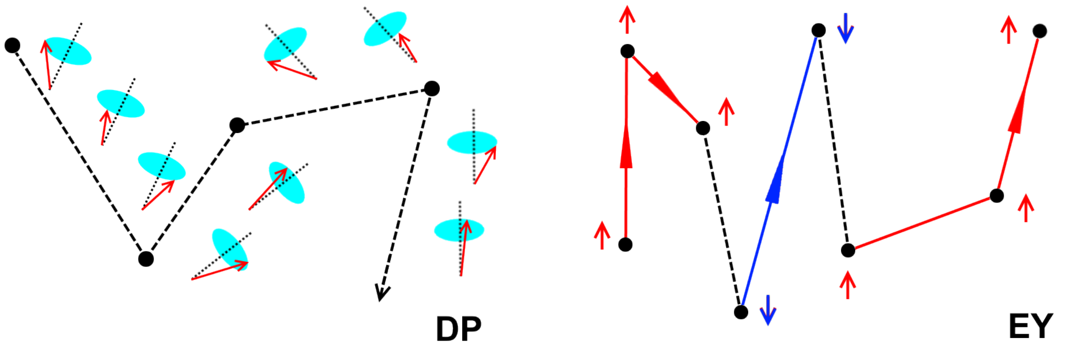

Figure 1.10.: Spin-relaxation mechanisms relevant for conduction electrons in 2DES. The DP describes spin-relaxation in non-degenerate, asymmetric systems with spin-splitting. Spin-up and spin-down states with the same momentum differ in energy. The spins precess around their momentum dependent local magnetic field. Momentum scattering (impurities, phonons, boundary) changes this axis of precession, thus disturbing spin-relaxation. The EY spin-relaxation desribes spin flip processes for Bloch states, where spin-up states also contain small spin-down amplitude and vice versa. Scattering on impurities, phonons or boundaries can flip the spins and lead to an overall spin-relaxation.

In the presence of SOC (Equation 1.6), electron wave functions are not eigenstates of the spin operator σ_z anymore, but can be treated as mixture of spin-up $|\uparrow\rangle$ and spin-down $|\downarrow\rangle$. According to Elliot the spin wave functions have the same symmetry as the lattice. The states of spin-up and spin-down can be written as

$$\begin{gathered} \left[a_{-k}\left|\uparrow\right\rangle + b_{-k}\left|\downarrow\right\rangle\right] e^{-i\boldsymbol{kr}} \\ \left[a^{*}_{-k}\left|\downarrow\right\rangle + b^{*}_{-k}\left|\uparrow\right\rangle\right] e^{i\boldsymbol{kr}} \end{gathered} \tag{1.16}$$

where a and b are coefficients related to the lattice periodicity an $\boldsymbol{k}$ and $\boldsymbol{r}$ the momentum and radius of the Bloch states. Under spatial and time reversal symmetry these states can be considered degenerate when the symmetry group contains inversion.

Due to SOC, the spin-up states have a small contribution of spin-down and vice versa, with $|b|$ in Equation 1.16 being much smaller than $|a|$ which usually is on the order of unity. Since the SOC splitting is much smaller than the energy gap between the bands, perturbation theory gives the estimate

$$|b| \approx \lambda_{so}/\Delta E \ll 1 \tag{1.17}$$

where λ_{so} is the amplitude of the matrix element between the two states and ΔE is the separation of the bands. Elliot related the shift of the electrons g-factor to the spin-relaxation time τ_s

$$1/\tau_s \approx (\Delta g)^2/\tau_p \tag{1.18}$$

where τ_p is the momentum relaxation time. While on the other hand the spin flip probability (with Equation 1.16) leads to

$$1/\tau_s \approx \langle b\rangle^2/\tau_p \tag{1.19}$$

allowing to write $\Delta g \approx |b|$. The qualitative Yafet relation links this result with the thermal equilibration time for the spin population, T_1, and temperature dependency of the resistance

$$1/T_1(T) \propto \left\langle b^2\right\rangle \rho(T). \tag{1.20}$$

Later calculations and experiments [103–106] refined this result for the case of III-V semiconductors, giving

$$\frac{1}{\tau_s(E_{\boldsymbol{k}})} = A\left(\frac{\Delta_{so}}{E_g+\Delta_{so}}^2\right)^2\left(\frac{E_{\boldsymbol{k}}}{E_g}\right)^2\frac{1}{\tau_p(E_{\boldsymbol{k}})}, \tag{1.21}$$

where Δ_{so} is the spin-orbit splitting of the valence band, E_g is the energy gap and $\tau_s(E_{\boldsymbol{k}})$ is the spin-relaxation time at an energy $E_{\boldsymbol{k}}$. A is a numerical factor determined by the exact scattering mechanism (for example electron-electron, electron-phonon or impurity scattering). By linking τ_s and B_{so} via Equation 1.11 and using $\mu \propto \tau_p$, for the EY spin relaxation the connection $B_{so} \propto 1/\mu$ is valid. The EY mechanism is usually most relevant for systems with low electron mobility.

2. Experimental methods

2.1. Sample Preparation

STO single-crystal substrates grown by a Verneuil (flame growth) process are purchased from CrysTec GmbH Kristalltechnologie (Berlin/Germany). The size of the substrates is $5 \times 5\,\mathrm{mm}^2$, with a typical thickness of 1 mm. The crystals are polished on one side by the manufacturer. The plane obtained after polishing is not exactly parallel to the atomic planes, displaying a so called substrate miscut of typically 0.1° or less.

2.1.1. Surface termination

In order to obtain an atomically well defined surface for film deposition, the substrates are subjected to a surface termination process. Generally, the (001)-oriented STO-substrates show a mixed surface termination with TiO_2 and SrO as top layer [107, 108], resulting in a step height of half a unit cell (uc). However, a clean, TiO_2-terminated surface is necessary for interfacial conductance in AO/STO heterostructures.

The recipe described in [107] allows to reproducibly obtain TiO_2-terminated (001)-oriented STO substrate surfaces [109]. At first, the substrates are bathed in bi-distilled water for 10 min to get strontium hydroxide which then can be removed by selective etching in a buffered ammonium flourid (BHF) bath for 30 s. Then, a stopping bath of 10 s in bi-distilled water is carried out to stop the etching. The substrates are blow dried with nitrogen. To recrystallize the surface a heat treatment (5 h at 950 °C) in flowing oxygen is performed in a tube furnace.

After annealing the resulting surface is checked by atomic force microscopy (AFM). A single-type terminated STO substrate surface shows step edges with step height of 3.9 Å (1 uc) and a terrace width related to the miscut angle α of approximately 220 nm (for $\alpha < 0.1^\circ$). No residual particles and no step bunching could be observed on the substrate surface. A constant friction signal on the surface measured by atomic-force microscopy

(AFM) confirms chemical homogeneity and hence the single-type termination. The same procedure has been carried out for (111)-oriented substrates, resulting in a step height of 2.3 Å ($\propto\ a/\sqrt{3}$, where a is the lattice parameter of STO). For (110)-oriented substrates no etching process is performed, since the crystallographic structure does not allow to obtain a single-type terminated surface via etching.

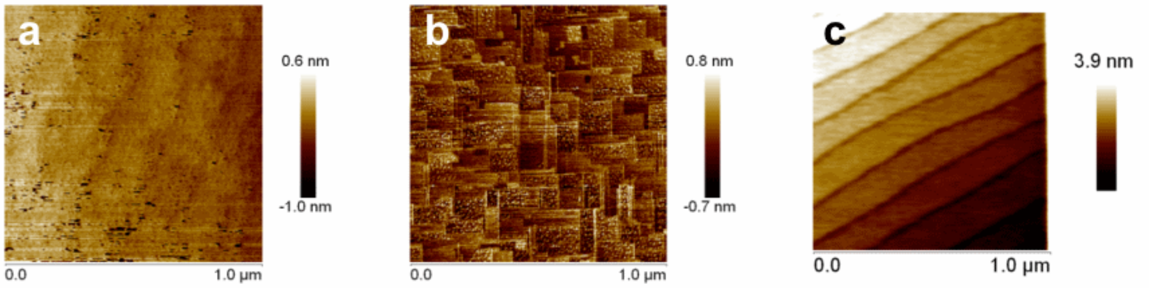

Figure 2.1.: Surface topography of a (001)-substrate as delivered (a), after only annealing (b) and after etching and annealing (c). The micrographs were obtained by AFM in contact mode.

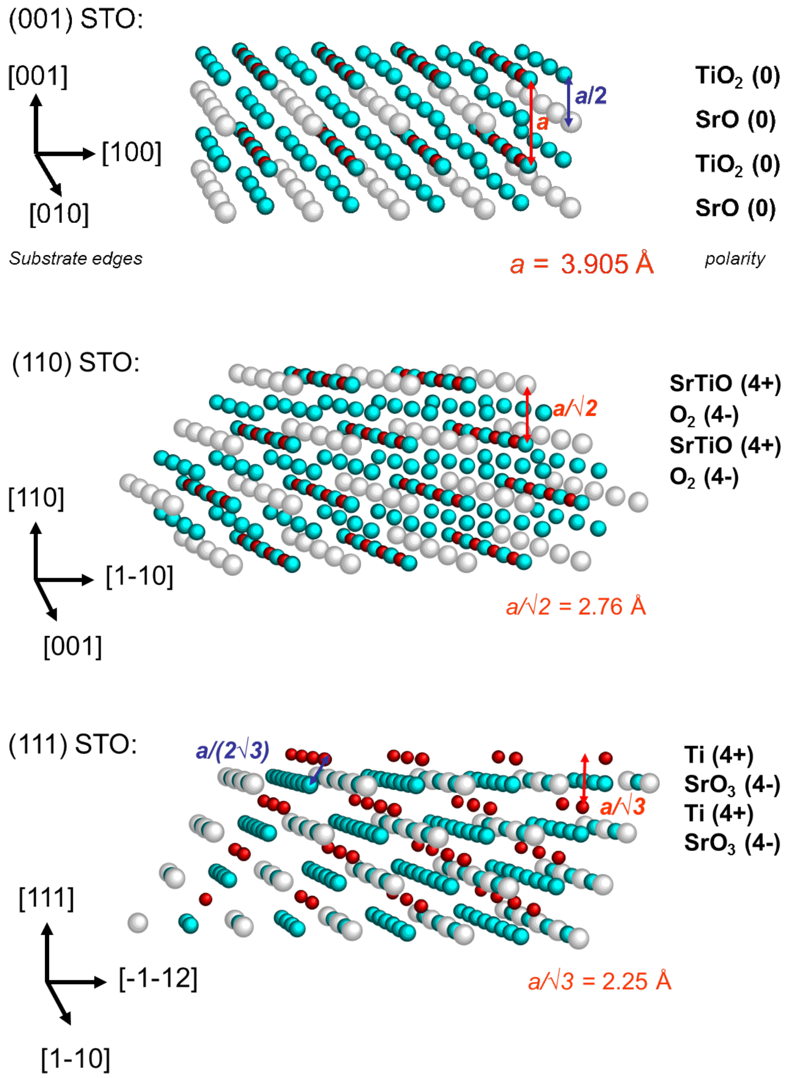

Figure 2.2.: Layered structure of STO single-crystal substrates for (001) (top), (110) (middle) and (111) (bottom) substrate orientation. Chemical elements and charging of the layers are indicated on the right. Crystallographic axes are shown on the left. The lattice parameter of STO is $a = 3.9$ Å.

2.1.2. Photolithography and pulsed laser deposition

In order to characterize electronic transport properties along specified crystallographic directions, resistance microbridges and Hall bars have to be patterned with specific alignment. Thus, two microbridge patterns as shown in Figure 2.3 were designed with bridges aligned by 0° to 135° with respect to the substrate edges. Common patterning techniques, such as wet-chemical or ion-etching or the use of an amorphous LAO hard mask which tend to produce parasitic conductance are not applicable. Furthermore, suitable etching agents are not available [110, 111]. Therefore, a different scheme has been developed. An amorphous CeO_2 hard mask was applied as an inhibit layer instead of amorphous LAO. The CeO_2 layer itself is insulating and does not cause any unwanted conductance, neither in combination with Al_2O_3 nor with the STO substrate [109].

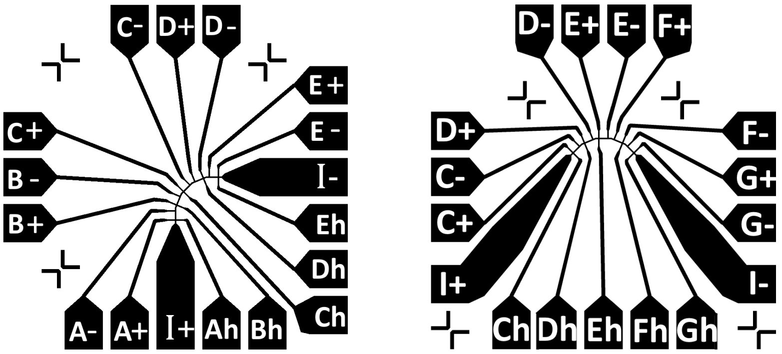

Figure 2.3.: Microbridges along different crystallographic directions ($20 \times 100\,\mu m^2$, $\varphi(A-G) = 0°, 22.5°, 45°, 67.5°, 90°, 112.5°, 135°$), with contacts for four-point resistance and Hall measurements. Designed by R. Schäfer.

The layouts shown in Figure 2.3 were reproduced on the surface of the substrates in a lithographic process using a positive photoresist (AZ MIR 701, Micro Chemicals). Spincoating at 4000 rounds per minute for 60 s gives a film thickness of the photoresist of 900 nm, which then is soft baked on a hot plate for 60 s at 90 °C. Exposure to ultraviolet light by a mask aligner (MA56 / 7.5 s × 18.4 mW/cm^2) was done in hard contact with the substrate. Developing was done for 45 s in AZ 726 MiF (Micro Chemicals). A schematic representation of the photolithography process is shown in Figure 2.4.

The deposition of the CeO_2 inhibit layer after the development was done by a firsr pulsed laser deposition (PLD) step from a polycrystalline target at room temperature and at an oxygen partial pressure of $p(O_2) = 0.1$ mbar. A thickness of 75 nm was achived with 1500 shots at a rate of 5 Hz and a laser fluence of about 1.5 J/cm^2 giving a deposition rate of 0.5 Å per laser pulse. The photoresist was then removed in a lift of process with

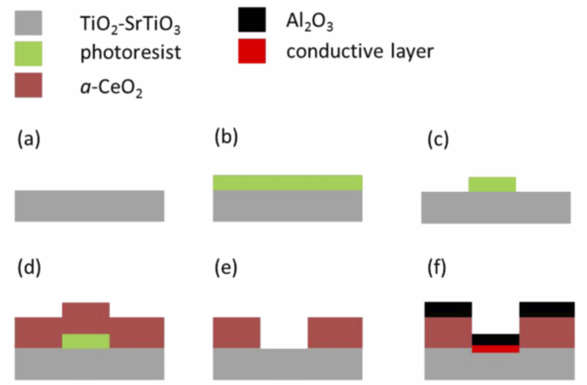

Figure 2.4.: Schematic illustration of the patterning process (cross section) [109]. (a) Bare TiO_2-terminated (001)-oriented STO substrate. (b) Substrate coated with positive photoresist. (c) Structure after UV-light exposure and development. (d) Deposition of a-CeO_2 by PLD. (e) Removing photoresist by lift-off process. (f) Deposition of Al_2O_3 by PLD. A conductive layer (2DEL) is formed at the interface.

TechniStrip P1316 (Micro Chemicals) in an ultrasonic bath of 20 s duration (×3 puddles) followed by washing in bi-distilled water for 10 s (×2 puddles).

Drying in nitrogen and 60 s on a hot plate at 130 °C results in a clean, TiO_2 terminated surface on the microbridges, while the rest of the sample is covered with CeO. In a second PLD step, a 15 nm thick layer of Al_2O_3 was deposited with $1.5\,\mathrm{J/cm^2}$ at 0.1 Å per laser pulse and a rate of 2 Hz, at a substrate temperature of 250 °C and an oxygen partial pressure of $p(O_2) = 10^{-6}$ mbar. The samples were cooled down to room temperature in the same oxygen atmosphere. Transmission electron microscopy (TEM) and electron energy loss spectroscopy (EELS) analysis has been done by Matthias Meffert at the Laboratory for Electron Microscopy (LEM) at KIT and shows a crystalline structure for the deposited Al_2O_3. EELS shows spectra corresponding to γ-Al_2O_3 [112] and oxygen deficient STO [37]. Figure 2.5 shows a TEM micrograph of the AO/STO interface and the obtained EELS spectra.

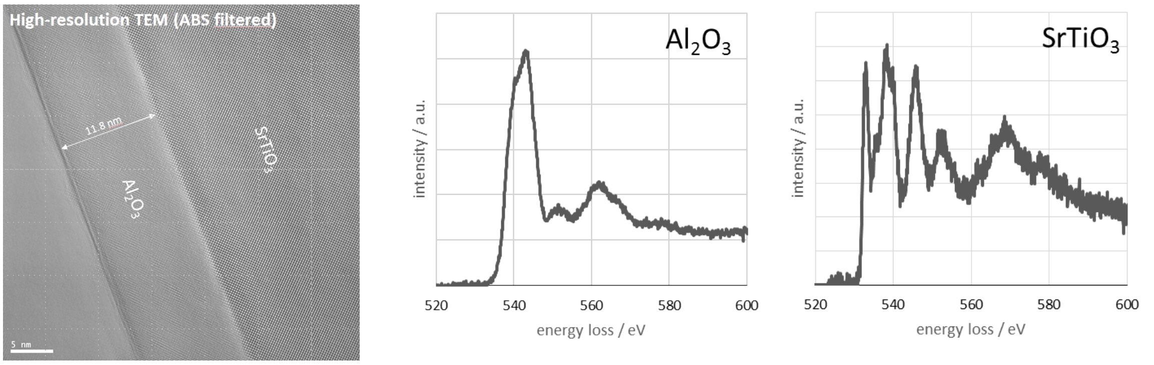

(a) (b) (c)

Figure 2.5.: TEM cross-section of an AO/STO heterostructure displaying the crystalline structure of the PLD-deposited Al_2O_3 (a), as well as EELS measurements on the oxygen absorption edge of the Al_2O_3 thin film (b) and the STO bulk (c). Measurements were done by M. Meffert at LEM.

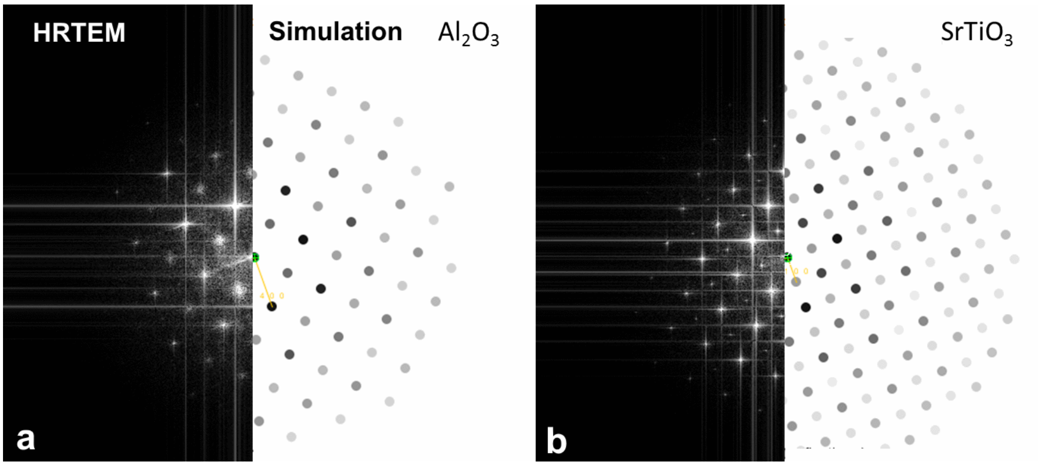

Figure 2.6.: High resolution TEM diffraction of an AO/STO heterostructure with the corresponding simulations displaying a well defined crystalline structure for (a) Al_2O_3 and (b) STO. Measurements were done by M. Meffert at LEM.

2.1.3. Ultrasonic wirebonding

Electrical contacts to the conducting interface were realized by ultrasonic wedge-wedge wirebonding. With this method, it is possible to contact the buried interface through the insulating top layer of Al_2O_3 by merging the 25 μm thick Al-wire (1 % Si, Heraeus, Hanau/Germany) into the surface with a short ultrasonic pulse. During the course of this thesis, the wire bonding machine was exchanged from an old MEI 1204W to a HB05 manual wire bonder by TPT (Munich/Germany) using 33 μm thick Al or Au wire. Both machines use bonding tools from CoorsTek Gaiser (Denver, USA).

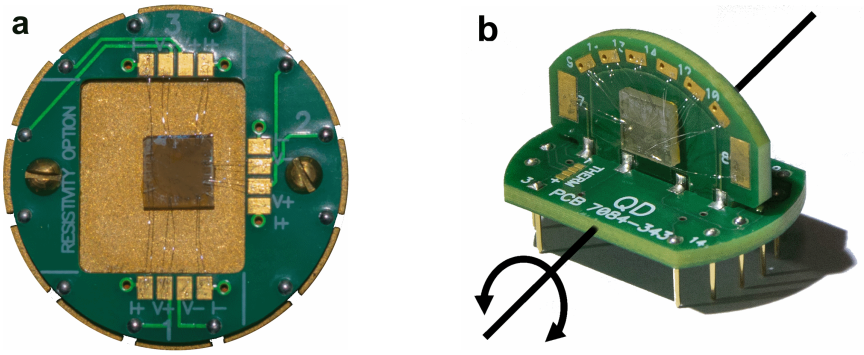

Figure 2.7.: (a) Standard sample holder for out-of-plane measurements with sample ready to load into the PPMS chamber. All bonding wire connections are doubled as backup and to reduce contact resistance. (b) Circuit board for transport measurements with in-plane magnetic field orientation. The axis of rotation is indicated and allows to turn the sample by up to 370°.

The aluminum wires were put in a flat loop from the gold contacts of the Physical Property Measurement System (PPMS) sample holder to the sample (see Figure 2.7), were the second contact is formed with a more powerful ultrasonic pulse than the first one, to ensure a defined, reliable tear of the wire when retreating the wedge. All connections made by wire bonding were doubled to half the contact resistance and to provide a backup in case of contact failure at low temperatures. Figure 2.8 shows bond contacts formed at different ultrasonic power settings and a focused ion beam (FIB) cross section which demonstrates that the sample has not been damaged during the bonding procedure. If the power of the bonds on the samples is set too low, the bond does not stick to the surface, if the power is set too high contact failures as demonstrated in Figure 2.8 occur. This includes direct tearing and small, barely visible cracks in the bond foot which can cause contact failures during thermal cycling of the sample.

An attempt to improve the electronic contacts by using gold-filled trenches as contact pads between the 2DES and the Al-wire was tested alike. However, no improvement of

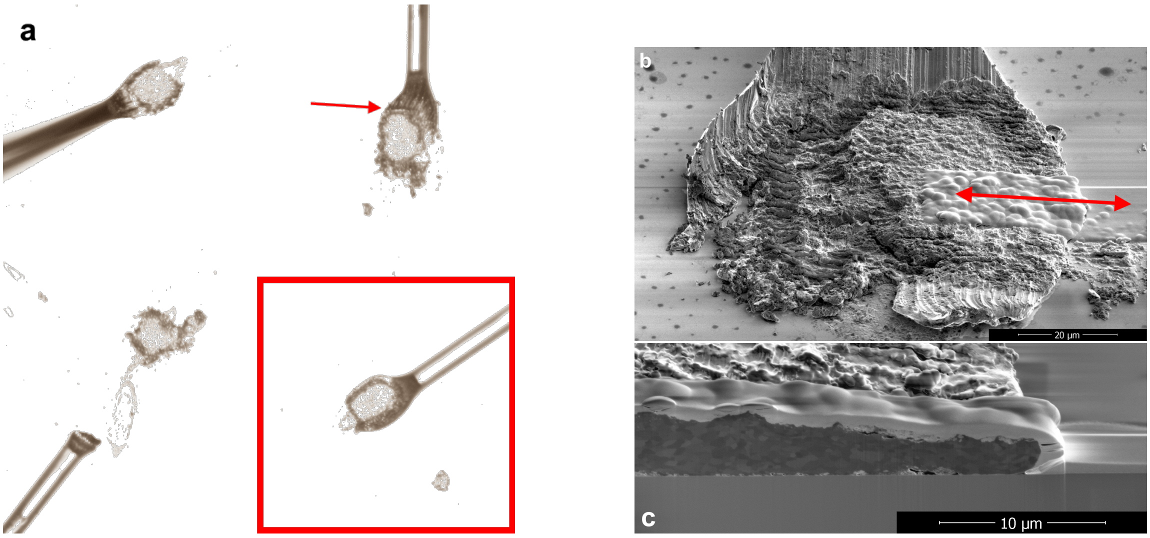

Figure 2.8.: (a) Top view of several bond contacts with failures caused by too much ultrasonic power. This leads to teared bond contacts but also barely visible cracks (indicated by the arrow) causing contact failure during thermal cycling of the sample. The highlighting shows an ideal contact with correct parameters and no signs of tearing. Wire diameter is 25 μm. (b) FIB/SEM micrograph of a wedge bond contact. The deformed Al-wire of the bond contact is shown on a LAO/STO heterostructure. The red arrow indicates the position of the FIB-cross-section (c), surrounded by a platinum layer to protect the material underneath from damage of stray Ga-ions. (c) shows the cross-section of the bond foot, with the protective platinum layer on top of the grained Al-structure (darker area) on top of the heterostructure. No obvious material intermixing is found at the interface, indicating that no damage is done on the heterostructure during the bonding process.

the electrical contact could be obtained in comparison to Al-wedge bonding carried out directly onto the bare sample surface.

2.2. Resistance Measurements

All resistance measurements were done in a PPMS by Quantum Design equipped with a 14 T superconducting magnet in a possible temperature range of 1.8 K - 400 K. Once loaded into the chamber, the sample was kept in a low-pressure helium atmosphere ($p < 10$ mbar). Resistance measurements were not started before 12 h after loading the sample to reduce the influence of charge carrier activation by light [113–115].

An AC current limited to 3 μA was used to avoid charging and heating effects at the contacts. The measurements were carried out in 4-point geometry to ensure negligible influence of the feed lines. The sheet resistance R_s was calculated by multiplying the measured longitudinal resistance R_{xx} with the ratio of the width to the length of the microbridges. *MR* measurements were done with the magnetic field perpendicular and parallel to the interface. For the in-plane measurements a sample rotator (Quantum Design) was used, allowing to turn the sample by up to 370°.

A wobbling motion occurred (precession of the sample surface normal to the ideal rotational axis), but was only noticeable in the very sensitive in-plane Hall effect measurements. The misalignment of the sample surface to the ideal rotational axis is typically smaller than 2°. The wobbling provokes a sinusoidal altering of the magnetoresistance which therefore is easily verified allowing an accurate correction of the measurement. (Figure 2.9).

Drifting of the measured sheet or Hall resistance over time due to residual photo-activated charge carriers or the thermal coupling of the sample to the temperature bath could easily be corrected by assuming an exponential or logarithmic drift over time. In addition, magnetoresistance and Hall resistance were made symmetric and antisymmetric, respectively, with respect to the applied magnetic field by calculating $R'(B) = (R(B) \pm R(-B))/2$.

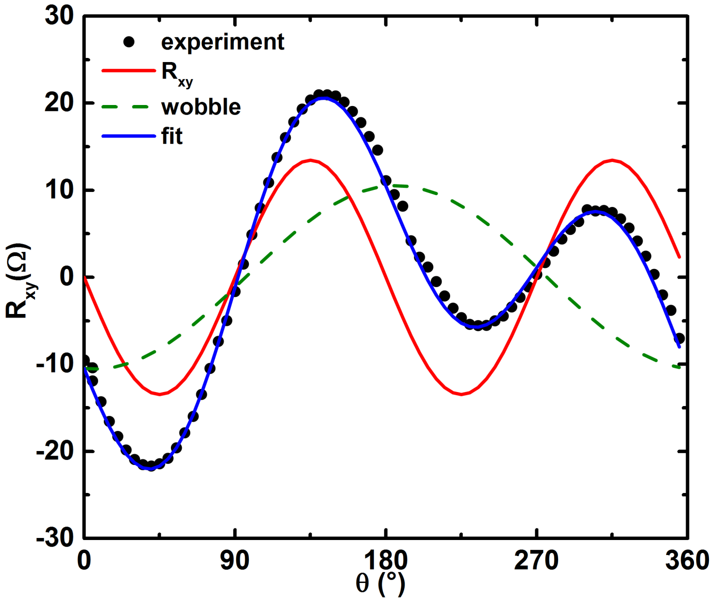

Figure 2.9.: Example of the correction of wobbling for an in-plane Hall resistivity measurement. The green, dashed line displays the sinus-function for a wobble $< 2°$, the red line corresponds to the corrected Hall resistance.

Table 2.1.: List of AO/STO samples produced in the course of this work, labeled according to the consecutive number for all samples handled in the same PLD chamber or their specific crystal-growth batch number. w_t is the average terrace width and ω_c the angle of the step edges with respect to the [100]-direction ($[\bar{1}\bar{1}2]$ for B296) and h_t the step height.

sample	STO surface	w_t (nm)	ω_c (°)	h_t (Å)
B290	(001)	120	85	3.905
B291	(001)	190	35	3.905
B296	(111)	200	20	2.3
B297	(110)	80	70	2.706
B338a	(001)	200	0	3.905
B338b	(001)	200	90	3.905
MJ2465a/b	(001)	45	135	3.905
MJ2466a/b	(001)	45	45	3.905

3. Results and Discussion

Indications of anisotropic electronic transport were first observed in LAO/STO heterostructures [1–4] and later also found for AO/STO systems in van der Pauw resistance measurements at low temperatures close to the superconducting transition [25, 116]. Possible reasons could be extrinsic defects, impurities or intrinsic anisotropy of the interface itself, like net surface charges at the step edges [6] or electronic phase separation [3]. Strong Rashba-type SOC due to the electric field caused by the polar mismatch at the interface can lead to electronic band modifications (band line-up) or electronic phase separation even in structurally perfect LAO/STO [7]. Thus, some of these effects may contribute to or even dominate the anisotropy of the AO/STO interface [26]. In this thesis more detailed resistance measurements on differently oriented interfaces are presented, to get a better understanding of the electronic properties with respect to the anisotropic electronic transport in the AO/STO system.

3.1. Anisotropic electronic transport of (001)-oriented AO/STO heterostructures

At first, two different samples of (001)-oriented AO/STO heterostructures have been produced, labeled B290 and B291, with step edges aligned by $\omega \approx 85^\circ$ and $\omega \approx 35^\circ$ with respect to the [100] direction. The substrates were taken from the same batch to ensure comparable sample quality. The miscut of the substrates typically is below 0.2°, resulting in a terrace width of about 120 nm and 190 nm for samples B290 and B291, respectively. Both samples have been patterned to obtain microbridges arranged by 0° to 90° with respect to the substrate edges, as shown on the left side in Figure 2.3. The width of the resulting microbridges is 18 μm.

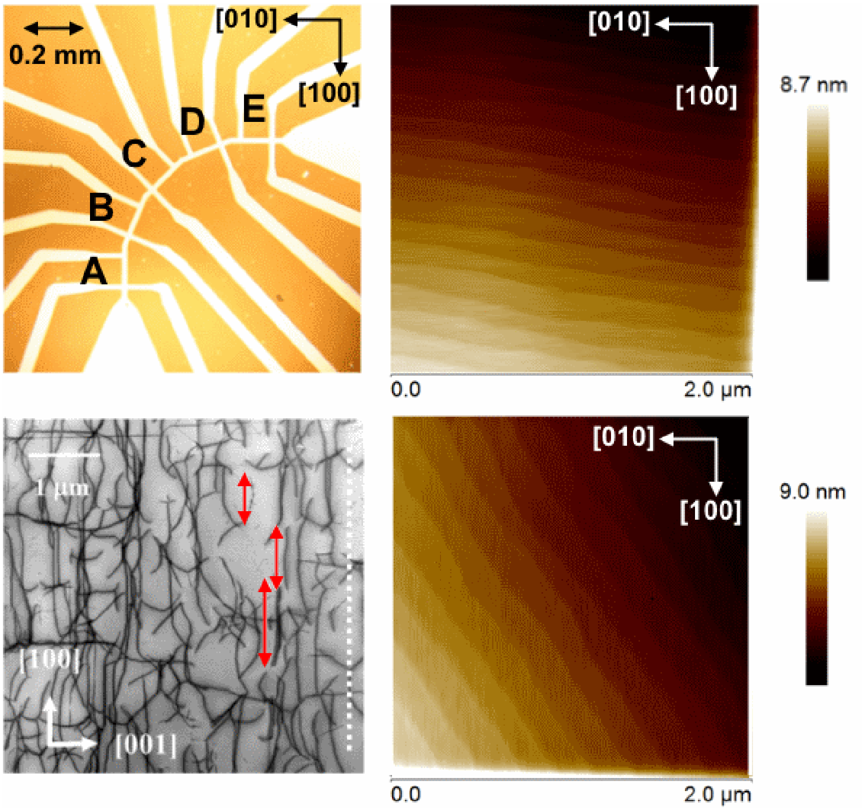

Figure 3.1.: (a) Micrograph of the different four-point microbridges A-E on a patterned sample. Dark areas show the CeO inhibit layer, delivering sharp contrast to the AO/STO conducting paths. (b) and (d) show AFM micrographs of the surface of bridge A for sample B290 and B291, respectively. The angle of the step edges (terraces) to the [100]-direction is $\omega_t \approx 85^\circ$ and $\omega_t \approx 35^\circ$. The step-edge orientation is the same over the whole sample surface. (c) Scanning transmission electron microscopy image (bright field) showing dislocations as dark lines with a high density in the (001) lattice planes. Red arrows indicate different lengths.

3.1.1. Temperature dependence

At first, temperature-dependent resistance measurements in the range of $2\,\mathrm{K} \leq T \leq 300\,\mathrm{K}$ were done for all microbridges A-E without applying magnetic field. Measurements were performed from 300 K to 100 K with temperature intervals of $\Delta T = 4\,\mathrm{K}$, for $100\,\mathrm{K} \geq T \geq 20\,\mathrm{K}$ with $\Delta T = 2\,\mathrm{K}$ and for $20\,\mathrm{K} \geq T \geq 2\,\mathrm{K}$ with $\Delta T = 1\,\mathrm{K}$. The resistance versus temperature plots for B290 and B291 are shown in Figure 3.2 (a) and (b), respectively. Heating and cooling rates were chosen to one minute per interval. Measurements with decreasing and increasing temperatures showed good agreement, indicating good thermalization of the sample. Generally, above $T = 100\,\mathrm{K}$, both samples show isotropic sheet resistance R_s with an almost T^2 dependence, which is attributed to strongly renormalized electron-phonon interactions [117]. Similar behavior is reported in STO heterostructures and n-type doped bulk STO [118, 119].

Below a shallow minimum around 30 K, R_s increases again while becoming clearly anisotropic. For $T < 10\,\mathrm{K}$, the resistance stays almost constant for each individual bridge, giving a residual resistance ratio of around 20 compared to R_s at 300 K. Below $T < 5\,\mathrm{K}$, R_s slightly decreases again for some microbridges, which can be explained by WAL [84, 120]. This behavior is fairly common in 2DEL with SOC [72, 121]. The overall $R_s(T)$ behavior can be well explained by combining electron-phonon interactions for higher temperatures and a dominating impurity-scattering at lower temperatures, given by $R_s = R_{imp} + R_{el-ph}$.

The temperature dependence of R_{imp} can be modeled by assuming localized charged impurities, like trapped charge carriers around oxygen vacancies in STO. Charge trapping in oxides and STO heterostructures is well known and can be described by a thermally activated process [122–124]. The exponential decrease of the number of trapped charged impurities with increasing temperature can be written as $N_i(T) = N_0 \times [1 - \exp(-T_A/T)]$ with the activation temperature T_A [125, 126] and $N_0 = N_i(T = 0)$. The impurity potential is electrostatically screened by the large dielectric permittivity of STO at low T. However, the dielectric permittivity $\epsilon(T)$ of STO decreases with increasing T, which results in a decrease of the screening of the impurity potential and therefore in an enhancement of R_{imp}. The quantum paraelectric behavior of STO is well described by the Barrett formula [127] where the temperature dependence of $\epsilon(T)$ is given by:

$$\epsilon(T) = C \times (T_1/2 \times \coth(T_1/2T) - T_0)^{-1}. \tag{3.1}$$

Here C is the Curie constant, T_1 the temperature below which quantum effects become relevant and T_0 is a pressure dependent specific temperature that can also reach negative values [128]. According to Fermi's golden rule, R_{imp} is proportional to $N_i \times V^2$ where the

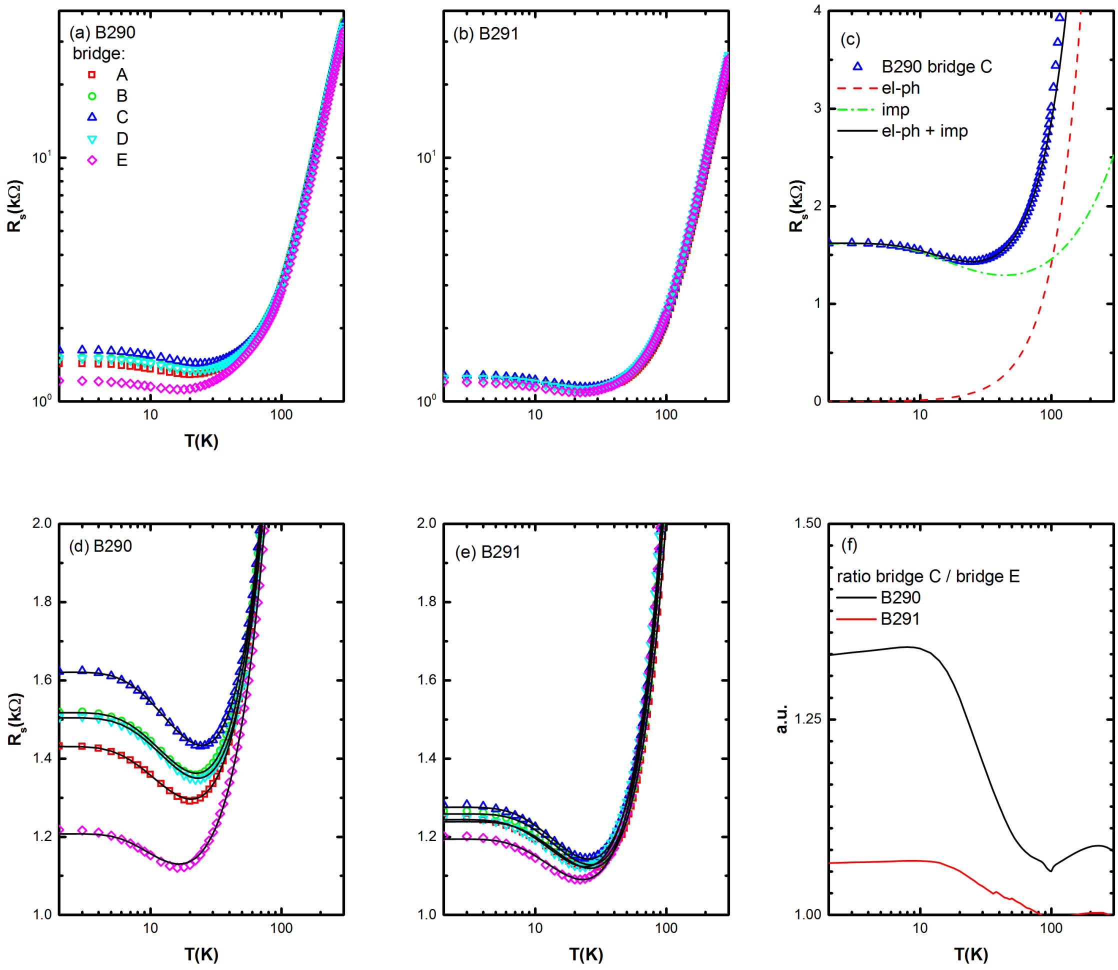

Figure 3.2.: Sheet resistance R_s versus temperature for sample B290 (a) and B291 (b) obtained from four-point measurements on the microbridges A-E. The fitting of the data to Equation 3.2 is demonstrated for bridge C of B290 in (c), with distinct contributions of electron-phonon and impurity scattering. (d) and (e) show the full fits (solid lines) for $T \leq 100\,\mathrm{K}$ for all microbridges. The full sets of fitting parameters are tabulated in Table 3.1. The anisotropy is displayed in (f), showing the ratio of the bridge with largest resistance (bridge C) to the lowest resistance (bridge E) for both samples.

impurity potential $V \propto \epsilon^{-1}$. Therefore the temperature dependence of sheet resistance can be expressed, according to Matthiessen's rule, by:

$$R_s(T) = A\left[1 - \exp\left(-\frac{T_A}{T}\right)\right]\left[\frac{T_1}{2}\coth\left(\frac{T_1}{2T}\right) - T_0\right]^2 + B \times T^2. \tag{3.2}$$

The constant A includes the Curie constant C and N_0. The constant B is a measure for the electron-phonon interactions. Fits to the temperature dependence of the sheet resistance data of samples B290 and B291 according to Equation 3.2 for $5\,\mathrm{K} \leq T \leq 100\,\mathrm{K}$ are shown in Figure 3.2. The full sets of fitting parameters are shown in Table 3.1.

Table 3.1.: Fitting parameters resulting from fits of R_s to Equation 3.2 for all five microbridges on samples B290 and B291. The fitting range was $5\,\mathrm{K} \leq T \leq 100\,\mathrm{K}$.

sample	bridge	A (Ω/K^2)	T_A (K)	T_0 (K)	T_1 (K)	B (Ω/K^2)
B290	A	0.35	20.69	-51.45	24.22	0.13
	B	0.29	21.67	-59.55	24.51	0.14
	C	0.26	22.44	-66.27	25.13	0.14
	D	0.28	22.11	-61.11	24.92	0.13
	E	0.4	24.26	-37.75	34.36	0.1
B291	A	0.21	23.65	-62.07	26.23	0.1
	B	0.21	23.54	-64.74	26.15	0.1
	C	0.18	24.45	-70.5	27.01	0.1
	D	0.15	25.61	-76.87	28.11	0.1
	E	0.17	25.8	-72.32	28.33	0.09

Obviously, anisotropic behavior of R_s is especially pronounced below 30 K, where R_s is dominated by R_{imp}. Hence, a more detailed analysis of R_s at 5 K was done. For sample B290, $R_s(T = 5\,\mathrm{K})$ is lowest for bridge E, where the interfacial steps are almost parallel to the microbridge and the current direction. For bridge A, where the interfacial steps are nearly perpendicular to the current direction R_s is about 17 % higher, while for bridge C with the current direction along [110] direction R_s shows an increase of about 30 % compared to E. Sample B291 shows less anisotropy, where bridge C shows the largest R_s and A and E differ only by 4 %.

The resistance ratio of the bridges C and E changes very little in the temperature range below 10 K (see Figure 3.2 (f)), supporting the assumption that the anisotropy in that region is dominated by R_{imp}, according to the first part in Equation 3.2. Other contributions such as electron-electron interaction (EEI) or WAL might still contribute to the anisotropy, but if so only to minor extent.

One reason for the anisotropic scattering is most likely the presence of dislocation lines in the STO substrate, which are known to influence transport properties in STO-bulk. Figure 3.1 (c) shows a TEM bright-field cross-section image of a STO substrate, indicating a high density of dislocations parallel to the interface. The different length of the dislocation lines in the projected image possibly indicates that they are aligned along different directions in the (001) lattice planes.

The flame fusion growth of the STO single crystals is known to result in a high dislocation density ($> 10^6\,\mathrm{cm}^2$) [129], where especially $\langle 110\rangle$ lattice dislocations with preferential $\{1\bar{1}0\}$ slip planes dominate. This leads not only to peculiar plastic mechanical properties [130], but can also increase charge carrier scattering for current direction perpendicular to the dislocation lines.

Of course, defect scattering at step edges has to be taken into account, too. For both samples, B290 and B291, the resistance for the current direction perpendicular to the interfacial steps is higher than for the current parallel to the steps. In LAO/STO heterostructures it has been shown that these steps reduce the charge carrier mobility and enhance the low-temperature resistance [131]. In addition, the SOC is likely altered by the interfacial steps, because of the additionally broken inversion symmetry at the step edges [18].

To get further insight on the nature of the anisotropic transport at low temperatures, the sheet resistance R_s at $T = 5\,\mathrm{K}$ has been modeled by assuming, beside isotropic defect scattering, anisotropic defect scattering by dislocation lines along [110] and $[1\bar{1}0]$ directions and interfacial steps. The sheet resistance is then given by

$$\begin{aligned} R_s &= r_0 + r_d(\varphi) + r_t(\varphi) \\ &= r_0 + \hat{r}_d \times \sin^2(\varphi - \omega_d) + \hat{r}_t \times \sin^2(\varphi - \omega_t), \end{aligned} \tag{3.3}$$

where r_0 stands for isotropic contributions by, i.e., point defects, r_d for the anisotropic contributions from dislocation lines and r_t for anisotropic contributions from defect scattering by terraces and interfacial steps. ω_d is the angle between the preferential orientation of dislocation lines and the [100] direction and ω_t the angle of the step edges, i.e., $\omega_t = 85°$ for sample B290 and 35° for sample B291.

Figure 3.3 visualizes the various contributions to $R_s(\varphi)$ according to Equation 3.3 for samples B290 and B291. The maximum anisotropy $(R_s^{max} - R_s^{min})/R_s^{min}$ which is deduced from the maximum and minimum values of R_s is about 55 % for sample B290 and 18.5 % for sample B291. The isotropic part r_0 of B291 is only slightly larger compared to B290,

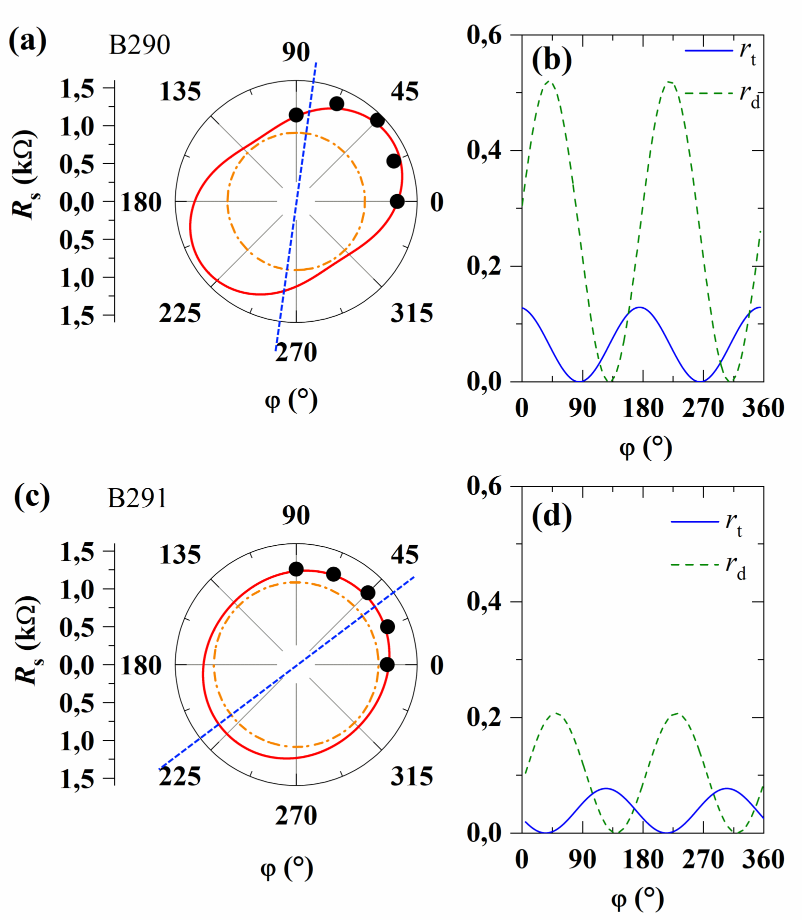

Figure 3.3.: Polar plots of the angular dependence of $R_s(\varphi)$ at $T = 5\,\mathrm{K}$ for sample B290 (a) with step edges almost parallel to the [010] direction (bridge E) and for B291 (bridge C) with step edges aligned by $\omega_t \approx 35°$. φ is the planar angle between the current and the [100] direction. The dashed blue line indicates the orientation of the step edges. The total sheet resistance R_s is modeled according to Equation 3.3. The dashed orange circle shows the isotropic contributions to R_s, while (b) and (d) show the contributions of the inhomogeneous distribution of $\langle 110 \rangle$ dislocation lines ($\omega_d = 135°$) and the contribution of interfacial scattering at the terraces.

which may indicate a more homogeneous distribution of dislocations in sample B291. This is possibly supported by the smaller amplitude of r_d.

The different alignment of the step edges leads to different positions of the minima of r_t. $\hat{r}_t$ is obviously larger for B290 compared to B291. The smaller terrace width of B290 results in a higher step density and thus in an increased $\hat{r}_t$. The ratio of $\hat{r}_t$ between the samples B290 and B291 ($129\,\Omega/77\,\Omega \approx 1.6$) corresponds to the inverse ratio of the terrace width of the samples ($190\,\mathrm{nm}/120\,\mathrm{nm} \approx 1.6$).

Obviously, the anisotropic electronic transport is dominated by r_d, i.e., defect scattering by anisotropically distributed dislocation lines. The preferential orientation of dislocation lines along the <110> direction results in a maximum and a minimum of r_d at $\phi = 45°$ and 135°, respectively. In order to prove that behavior experimentally, we have patterned two samples (B338a and B338b) with microbridges aligned from 45° to 135° (labeled C to G) with respect to the substrate edges. The step edges are normal to bridge C for B338a and parallel for B338b, with a terrace width of about 200 nm. The T dependence of $R_s(T)$ of the corresponding microbridges were comparable to those of sample B290 and B291. The polar plots of R_s at $T = 5\,\mathrm{K}$ are shown in Figure 3.4. The measurements confirm our assumptions on the anisotropic electronic transport being dominated by step edges and dislocations.

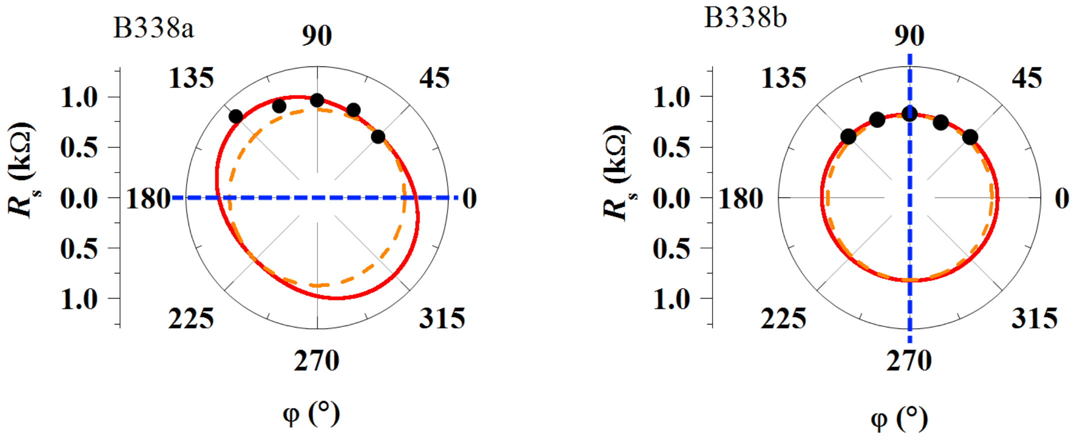

Figure 3.4.: Polar plots of the angular dependence of $R_s(\varphi)$ at $T = 5\,\mathrm{K}$ for sample B338a and B338b, both with microbridges aligned from 45° to 135°. The dashed orange circle represents the isotropic part of R_s. The solid line displays the anisotropic contribution to R_s which is dominated by r_d. The dashed blue line indicates the orientation of the step edges. Maxima of r_d are pronounced at 135°, i.e., current direction perpendicular to the (110) direction.

In contrast to the contributions of r_d to R_s which dominate the anisotropic transport, defect scattering by step edges, i.e., r_t only amounts to about 6 % of R_s and seems to contribute only to minor extend to anisotropic transport. First of all, this might be related to the smaller probability of defect scattering by step edges, which is limited to the immediate interface only, in contrast to defect scattering by dislocation lines which possibly reaches deeper into the bulk STO. Comparing the electron mean free path λ_{mfp} which can be estimated by

$$\lambda_{mfp} = v_f \times \tau \qquad v_f = \frac{\hbar\sqrt{2\pi n_s}}{m^*} \qquad \tau = \mu \times m^*/e. \tag{3.4}$$

to the width of the terraces ($w_t \approx 120{-}190\,\mathrm{nm}$), reveals that it is rather small which may further reduce the sensitivity of R_s to r_t. With $n_s \approx 2 \times 10^{13}\,\mathrm{cm}^{-2}$ and $\mu \approx 200\,\mathrm{cm}^{-2}/\mathrm{Vs}$ for $T = 5\,\mathrm{K}$, λ_{mfp} is around 15 nm and thus about one order of magnitude smaller than the terrace width.

In order to further investigate the role of step edges and surface scattering on the anisotropic electrical transport properties of (001) AO/STO, four different samples with a high surface miscut angle of 0.5° have been prepared. The higher miscut angle results in a higher step density and should enhance defect scattering by step edges which might allow to increase or adjust anisotropic electronic transport. The four substrates were taken out from same batch, but polished in two different directions resulting in step edges perpendicular to the [$\bar{1}$10] and [110] direction, respectively. For each step-edge orientation, one sample was patterned with microbridges from 0° to 90° and one with microbridges from 45° to 135°. The microbridges are labeled according to the patterns in Figure 2.3. The orientation of the microbridges with respect to the step edges is shown in Figure 3.5.

Figure 3.6 displays the corresponding micrographs. Short-circuited bonding pads visible in the first row, especially for MJ2465b, were separated before the transport measurements by scratching the surface with a bonding wedge made from tungsten carbide. The second row shows the AFM-tip position (bridge A) from where the micrographs shown in row three were taken. The step-edge orientation is perpendicular to the miscut direction and corresponds to the expected one, shown in Figure 3.5. The miscut angle of 0.5° results in a calculated terrace width of around 45 nm, which is confirmed by the AFM measurements (see Figure 3.6). Therefore, the step density is increased by a factor of about 4 with respect to sample B290 and B291.

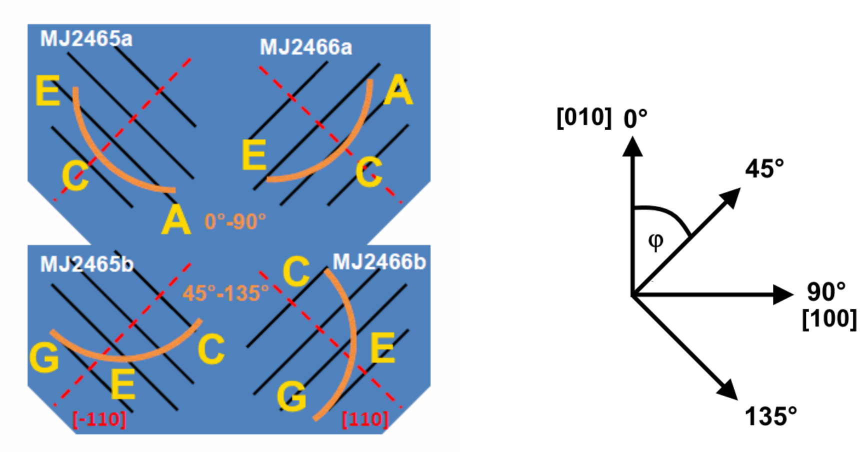

Figure 3.5.: Overview of the microbridge arc (orange line) orientation with respect to the step edges (black lines) for the different high miscut samples. The miscut direction is indicated by the dashed red lines.

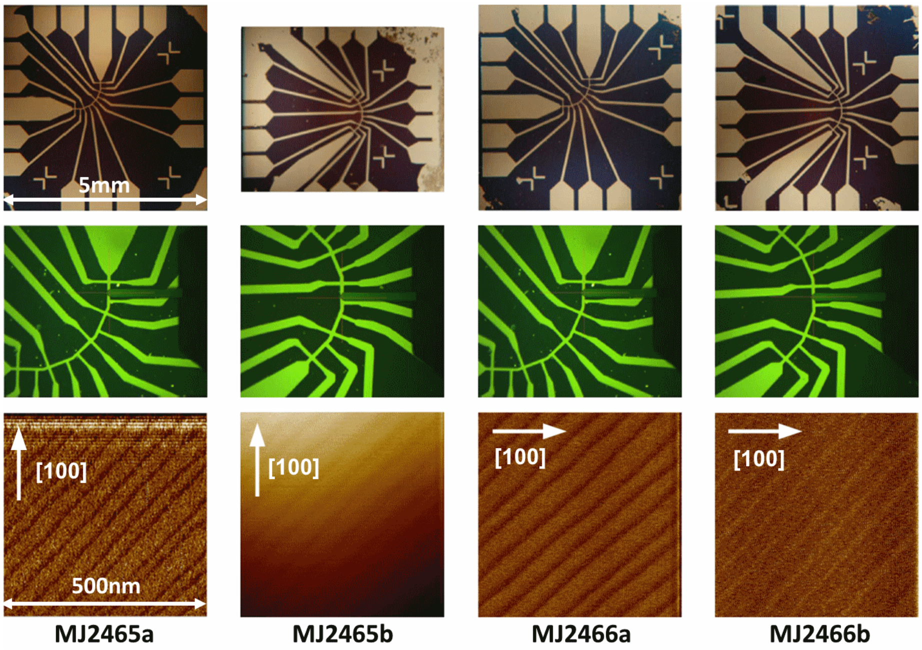

Figure 3.6.: The top row shows micrographs of the microbridge patterns of the high miscut samples before wire bonding. Connected pads at the ends of feeding lines were separated before bonding by scratching the surface with a discarded bonding wedge made out of tungsten carbide. The second row shows the microbridges where the AFM images in the last row where taken. There are no residual particles or imperfections in the conducting areas (bright green). The last row shows the terrace structure inside the microbridges after AO deposition. The images were taken by AFM in friction mode.

Fits to the resistance versus temperature data were performed according to Equation 3.2 in the temperature range of $5\,\mathrm{K} \leq T \leq 100\,\mathrm{K}$ and are shown in Figure 3.7. The full set of fitting parameters can be found in the appendix in Table A.2. The resistance versus temperature data for the high-miscut samples displays the same overall behavior as that of the low-miscut samples (Figure 3.2), i.e., anisotropic transport is only significant for $T < 30\,\mathrm{K}$ and maximum anisotropy for the microbridges at $T = 5\mathrm{K}$ is about 50 %. Thus, the increase of the step-edge density does not drastically change the electronic transport.

As for the samples B290 and B291, R_s is dominated by electron-phonon interactions for $T \geq 100\,\mathrm{K}$ and below the shallow minimum at around 30 K by impurity scattering. Clear anisotropy develops only in the low-temperature regime below 50 K. The resistance of the bridge at 90° of MJ2466a is shifted down over the whole temperature range, but otherwise displays the same characteristics as the other microbridges. Thus, the shift to a lower overall resistance is attributed to other causes than defects or step edges, like resides on the surface or short-circuited contact pads.

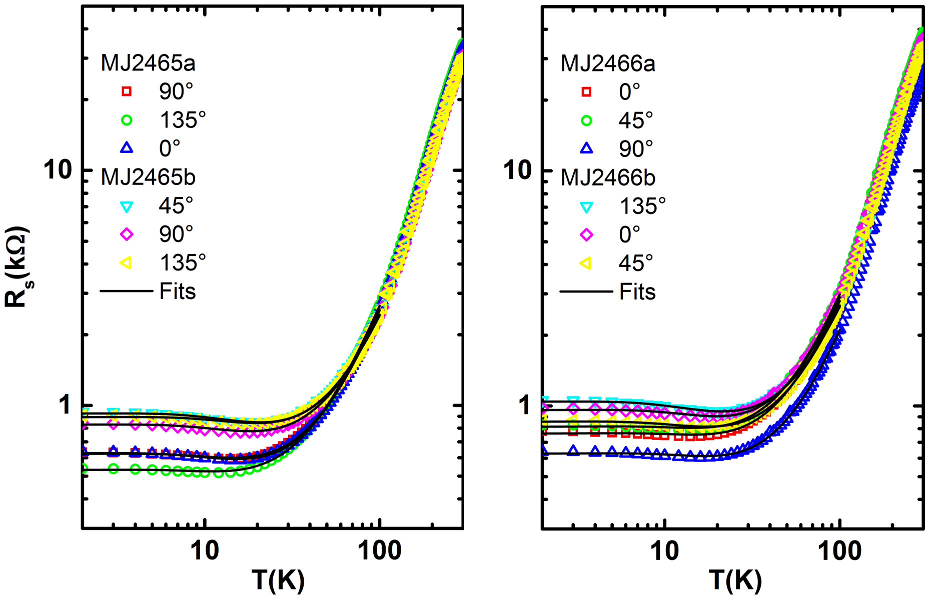

Figure 3.7.: Sheet resistance R_s versus temperature for high miscut samples obtained by four-point measurements on selected microbridges. Fitting was performed in a temperature range of $5\,\mathrm{K} \leq T \leq 100\,\mathrm{K}$.

The anisotropy of the sheet resistance for $T = 5\,\mathrm{K}$ is shown in Figure 3.8. Despite some scattering of data points, the largest resistance is found at 45° for MJ2465 and 135° for MJ2466. Therefore, the angular position of the maximum of the anisotropy obviously changes by 90°. Since the only difference between both sets of samples is the orientation of the step edges, the change in the anisotropy is likely related to the step-edge orientation. The maximum resistance indeed occurs for current direction perpendicular to the step edges. The anisotropic contribution to R_s amounts up to 22 % as obtained by fits according to Equation 3.3. Here, only one sinus function is needed to characterize the anisotropy, due to the alignment of the step edges at 45° or 135° for MJ2466a/b and MJ2465a/b, respectively: $R_s = r_0 + (\hat{r}_d + \hat{r}_t) \times \sin(\varphi - \omega_t)^2$.

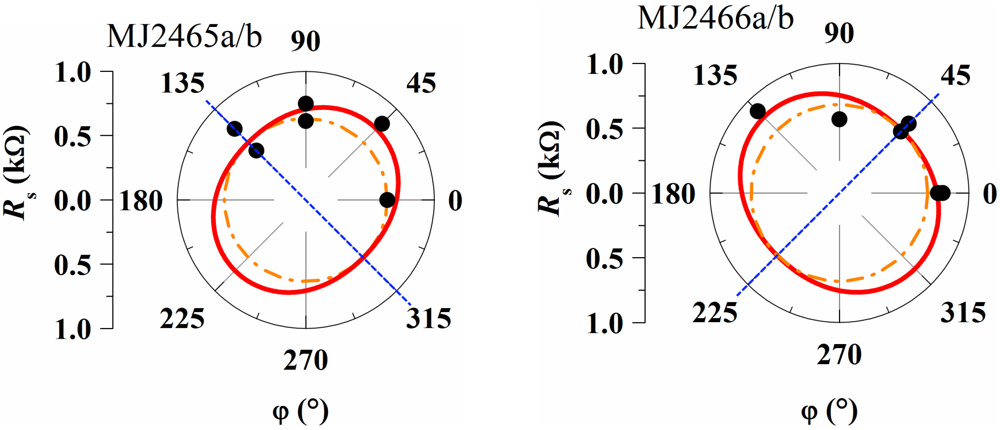

Figure 3.8.: Anisotropic sheet resistance of the high miscut samples. The left side includes the samples MJ2465a and MJ2465b with step edges along 135°, the right side side shows MJ2466a/b with step edges aligned by 45°. The dashed blue line indicates the orientation of the step edges. The anisotropic contributions obtained from fits for both samples are around 22 %, with the highest resistance for the current perpendicular to the step edges.

Since all four high-miscut samples are from the same batch, a similar distribution of dislocations is assumed. The resistance of all four samples is found to be about 22 % larger for the current direction perpendicular to the step edges. Thus, the anisotropy is dominated by the step edges, since no relevant contribution to the anisotropy from dislocation lines is found. The dislocation lines are most likely distributed evenly along the $[1\bar{1}0]$ and [110] direction, resulting in their contribution to the anisotropy being $\hat{r}_d = 0$ while increasing r_0.

For an inhomogeneous distribution of dislocations in AO/STO, the anisotropy is most likely dominated by the dislocations. Step edges due to the miscut angle increase the resistance for the current direction perpendicular to the step edges and thus contribute to the anisotropic transport. The full set of fitting parameters for all (001) AO/STO samples can be found in Table A.1.

With a higher density of step edges, their contribution to the anisotropic transport rises. This makes it possible to manipulate the anisotropy of the electric transport via the density of the step edges, which can be controlled by the substrate miscut angle.

3.1.2. Magnetic field dependence

The out-of-plane magnetic field dependence of R_s was measured in fields up to $B = 14\,\mathrm{T}$, with the field direction perpendicular to the samples surface. For Hall and magnetoresistance measurements, a routine with step sizes of $\Delta B = 10\,\mathrm{mT}$ for fields smaller than $B = 0.1\,\mathrm{T}$, $\Delta B = 100\,\mathrm{mT}$ for $100\,\mathrm{mT} \leq B \leq 1000\,\mathrm{mT}$ and $\Delta B = 1\,\mathrm{T}$ for fields larger than $B = 1\,\mathrm{T}$ was used.

Figure 3.9 (a) shows Hall measurements on sample B290 for selected temperatures for all microbridges. Both field orientations with respect to the z axis (positive or negative fields) were investigated, but no hysteretic behavior was found for R_{xx} or R_{xy} ($-R_{xy}$ shown in plots). The Hall measurements show isotropic behavior and a linear field dependence with a negative slope for $T \geq 100\,\mathrm{K}$, indicating single-type carrier transport by electrons.

Below 30 K a nonlinear magnetic field dependence evolves, denoting multi-type carrier transport. In addition, the Hall resistance becomes different for the various microbridges and shows clear anisotropic behavior.

With respect to the nonlinear, s-shape behavior of the Hall resistance, a two-band model is often applied to model the Hall resistance of LAO/STO [41]. However, to deduce sheet carrier concentration and carrier mobility, one has to assume that both are independent of B. This may not be justified and can lead to large errors in evaluation of the parameters. Therefore only the values of R_{xy} at high fields around 14 T and in the limit of zero field are used to obtain robust experimental values of the total sheet carrier density n_{tot} and of the carriers with the highest mobility n_{hi}.

Figure 3.9 (b) and (c) show the charge carrier density n_{tot} and mobility μ for sample B290. The carrier density has been calculated by $n_s = \frac{B}{e \cdot R_{xy}}$ in the limits of $B \leq 1\,\mathrm{T}$ and $B \geq 10\,\mathrm{T}$ to extract n_{hi} and n_{tot}, respectively. n_{hi} only differs by about 10 % from n_{tot}, which indicates that the low mobility charge carriers contribute to the transport only to a minor extent.

At $T = 300\,\mathrm{K}$, n_{tot} for B290 is about $4 \times 10^{13}\,\mathrm{cm}^{-2}$ and decreases to around $2.5 \times 10^{13}\,\mathrm{cm}^{-2}$ for temperatures below 10 K. B291 shows slightly higher carrier densities, but the same overall behavior. The drop in n_{tot} with decreasing temperatures is interpreted as charge carrier freeze-out or trapping [126, 132] which is often observed in oxides and STO-based heterostructures [117].

With decreasing temperature, μ increases from around $5\,\mathrm{cm}^2/\mathrm{Vs}$ at room temperature to about $300\,\mathrm{cm}^2/\mathrm{Vs}$ at $T \approx 20\,\mathrm{K}$ where a shallow maximum is observed. The mobility was calculated by $\mu = [R_s(B = 0) \times n_{hi} \times e]^{-1}$. Below 10 K, the mobility is limited by defect

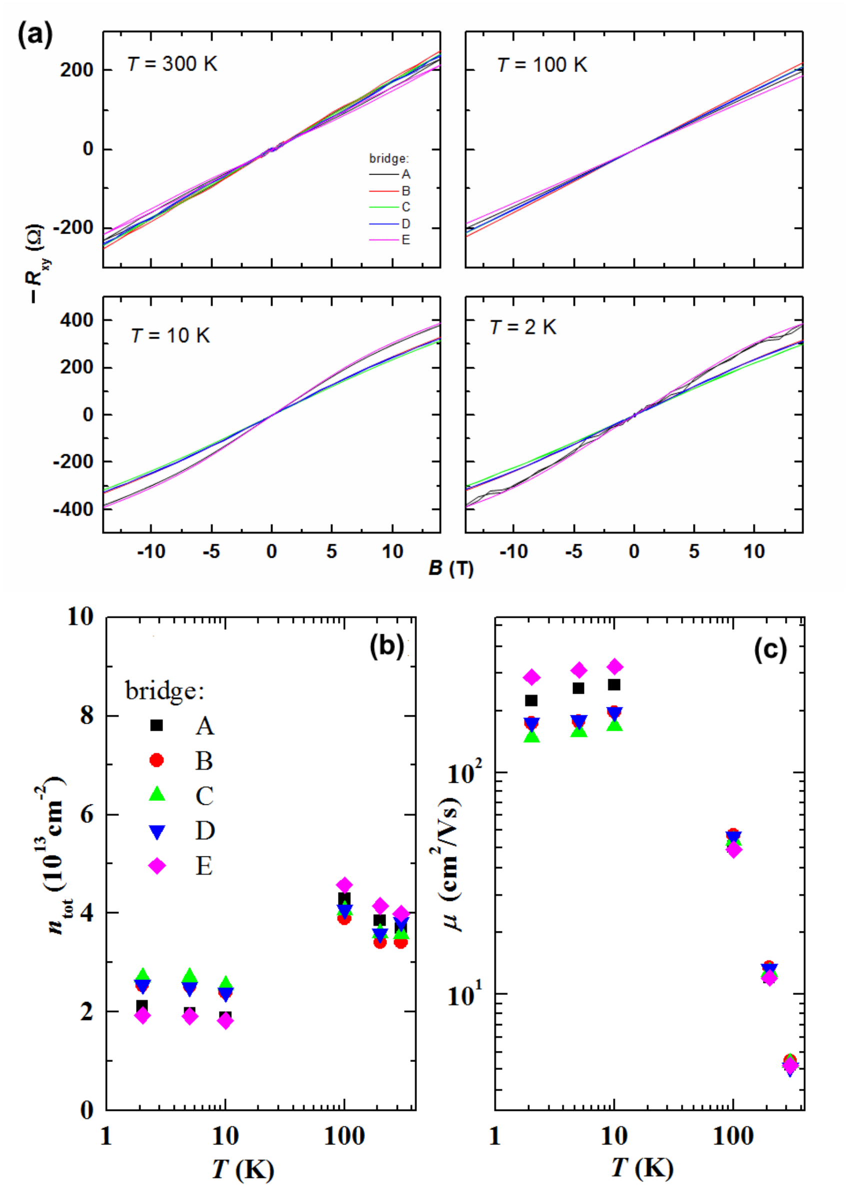

Figure 3.9.: (a) Hall resistance measurements for bridges A-E for selected temperatures. Total sheet carrier density n_{tot} (b) and Hall mobility μ (c) versus T for sample B290.

or impurity scattering and shows significant anisotropic behavior with respect to the different microbridges, i.e., crystallographic directions.

For sample B290 bridge E the mobility is almost twice as large as for bridge C, which shows the lowest mobility. For sample B291 lowest μ is also found for bridge C. The results are in good agreement with the interpretation of the in-plane angle dependence of the residual resistance $R_s(\phi)$ at 5 K (see Figure 3.3). The variation of R_s is obviously caused by changes of the carrier mobility. Enhanced defect scattering results in a decrease of carrier mobility and hence an increase of R_s. Therefore, the carrier mobility is smallest and R_s is largest for current directions perpendicular to the dislocation lines or step edges. Highest mobility is consequently observed for current directions parallel to the step edges and dislocation lines.

The magnetoresistance, $MR = [R_s(B) - R_s(0)]/R_s(0)$, was measured from 300 K down to 2 K. MR versus B is shown in Figure 3.10 for selected temperatures for both samples B290 and B291. For $T \geq 100$ K, both samples show positive, mostly isotropic MR being smaller than 1 %. At low temperatures ($T \leq 20$ K), MR increases up to about 17 % and becomes anisotropic with respect to the microbridges A-E.

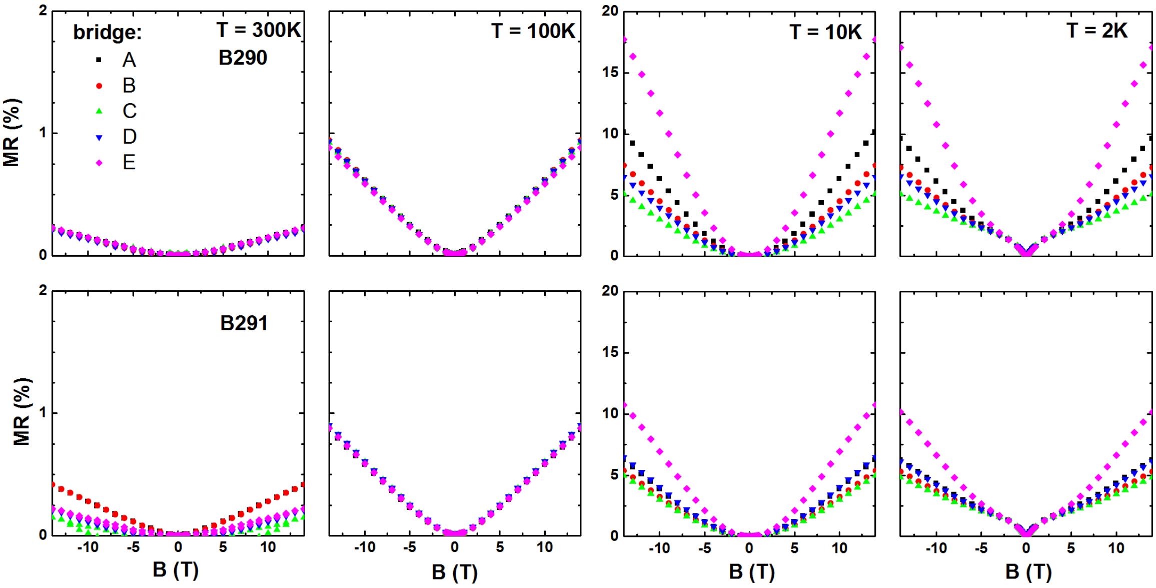

Figure 3.10.: Relative MR at selected temperatures for bridges A-E of the samples B290 and B291. Anisotropy emerges at low temperatures with MR rising up to 20 %. WAL emerges below 10 K.

The significant positive MR at low temperatures most likely originates from elongated electron paths due the orbital motion caused by the Lorentz force. The longer paths increase the scattering rate, which is known as Lorentz scattering. With the assumption of two bands with different charge carrier densities for each band and cyclotron motion on open orbits, the magnetic field dependence of the sheet resistance can be expressed by a Lorentz function according to Kohler [53, 54]: $MR \propto B^2/[1 + (B/w)^2]$.

The broadening w is strongly related to the Hall mobility μ and can be regarded as a robust parameter, since the low-temperature *MR* curves ($T \leq 10\,\mathrm{K}$) of Figure 3.10 display a point of inflection at round 10 T, indicating a saturation of R_s at a finite magnetic field. For temperatures of $T \geq 10\,\mathrm{K}$, *MR* can be almost perfectly described by Lorentz scattering:

$$R_L = \frac{R_0 + R_\infty(\frac{B}{w})^2}{1 + (\frac{B}{w})^2}, \tag{3.5}$$

where R_L is the magnetoresistance caused by Lorentz scattering, R_0 the zero-field resistance and R_∞ the saturated magnetoresistance at high fields The smallest broadening w is found for bridge E (Figure 3.11) which also shows the highest mobility (Figure 3.9), while bridge C displays the strongest broadening along with the lowest mobility. Since the broadening w usually scales nearly linearly with the inverse of the mobility, the anisotropic behavior of *MR* is most likely caused by the different charge carrier mobilities.

For temperatures below $T = 10\,\mathrm{K}$, weak antilocalization (WAL) emerges from SOC and influences the transport properties at small magnetic fields [72]. At $T = 2\,\mathrm{K}$ contributions from WAL dominate magnetotransport for $B < 5\,\mathrm{T}$, while at larger magnetic fields ($B > 8\,\mathrm{T}$) *MR* is comparable to that at 10 K. It is well known that the Rashba-type SOC in LAO/STO heterostructures produces WAL behavior at low temperatures and magnetic fields [72]. Obviously, the magnetotransport in AO/STO is affected by EEI and WAL alike [120] and dominates *MR* at low T and B as well. Therefore, within the diffusive transport regime *MR* should be described by the two dimensional WL theory [84, 86, 87, 120].

The model developed by Maekawa and Fukuyama in 1981 for the diffusive regime [87] includes Zeeman corrections, which in the LAO/STO systems should be much smaller compared to the contributions from SOC.

The spin-splitting energy due to the Rashba effect depends on the wave vector k and results in a k^3 spin splitting (cubic Rashba effect) with a similar field dependence as derived by the Maekawa-Fukuyama (MF) theory [133, 134]. The parameters in the MF expression (Equation 3.6) are the inelastic field B_i, the spin-orbit field B_{so} and the field-dependent Zeeman correction γ which contains the electron g factor. ψ stands for the digamma function. The MF formula for the conductivity is given by

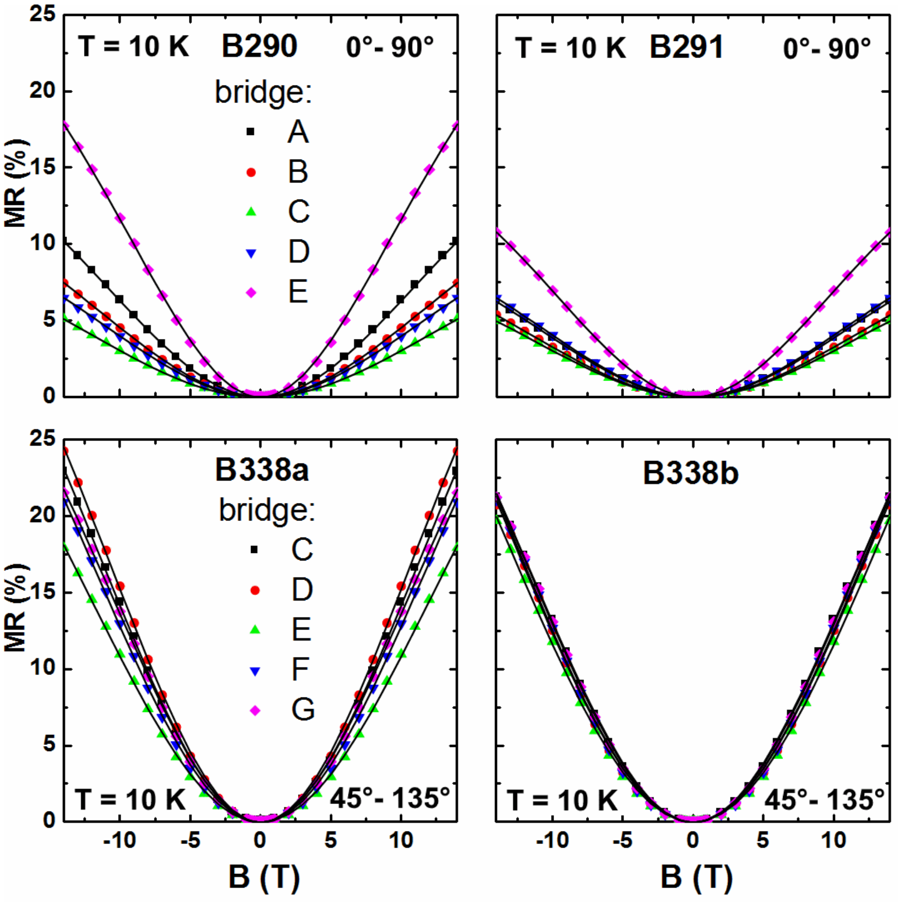

Figure 3.11.: *MR* at 10 K of the different microbridges (A-E) of the samples B290 and B291 (0°-90°), and of B338a and B338b (microbridges C-G, 45°-135°). Samples B338a and B338b display a somewhat larger *MR* and smaller anisotropic behavior while showing an increased mobility. The solid black lines represent fits according to Equation 3.5.

$$\begin{aligned}\frac{\Delta\sigma(B)}{\sigma_0} = \Psi\left(\frac{B}{B_i + 2B_{so}}\right) \\ + \frac{1}{2\sqrt{1-\gamma^2}}\Psi\left(\frac{B}{B_i + B_{so}\left(1+\sqrt{1+\gamma^2}\right)}\right) \\ - \frac{1}{2\sqrt{1-\gamma^2}}\Psi\left(\frac{B}{B_i + B_{so}\left(1+\sqrt{1-\gamma^2}\right)}\right),\end{aligned} \tag{3.6}$$

where $f(x) = \psi\left(\frac{1}{2} + \frac{1}{x}\right) + \ln(x)$ and $\sigma_0 = e^2/\pi h$ is the quantum of conductance. In order to obtain only the contributions from WAL, $R_s(B, 10\,\mathrm{K})$ has been subtracted from $R_s(B, 2\,\mathrm{K})$. Then, a least square fit according to Equation 3.6 was performed in the range of $B < 3\,\mathrm{T}$, with the parameters B_i, B_{so} and γ, where $\gamma = g\mu_B B/4eDB_{so}$. μ_B is the Bohr magneton and D the diffusion coefficient. Figure 3.12(a) shows exemplary the *MR* of bridge E for sample B290 at 10 K and 2 K. In Figure 3.12(b), contributions to the conductance only by WAL are plotted. Finally. Figure 3.12(c) shows the fitting parameters B_i and B_{so} versus the in-plane direction of the current for samples B290 and B291.

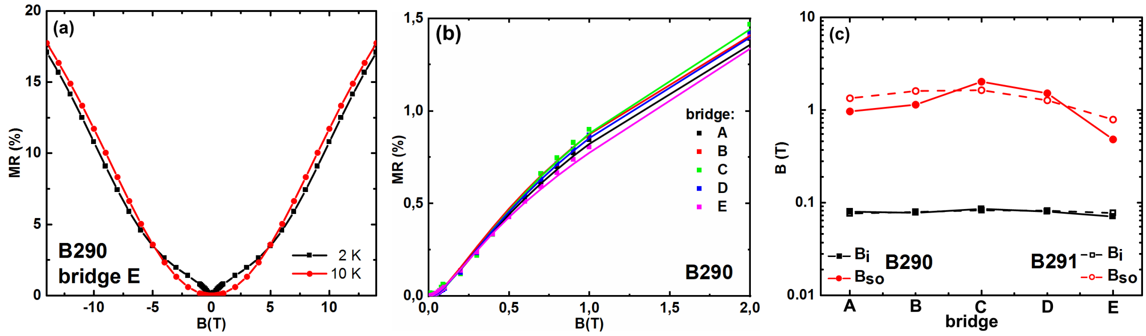

Figure 3.12.: (a) *MR* for microbridge E of sample B290 at 10 K and 2 K. The difference gives the contribution from WAL. (b) Fits to the WAL contributions at 2 K of microbridges of B290, according to Equation 3.6. (c) B_i and B_{so} of the samples B290 and B291 as a function of the the in-plane direction of the current. $\phi = 0°$ corresponds to bridge A and $\phi = 90°$ to bridge E.

Generally, contributions from WAL are much smaller compared to those from Lorentz scattering (LS). However, for $B < 2\,\mathrm{T}$, WAL dominates magnetotransport, see Figure 3.12 (a). The magnetoconductance, $\Delta\sigma = \sigma(B) - \sigma(0)$, is around $0.3\,\mathrm{e}^2/\hbar$ for B290 and $0.2\,\mathrm{e}^2/\hbar$ for B291, respectively, which is in line with the quantum nature of the underlying effect of WL. The parameters B_i and B_{so} are in the range of 0.1 T and 1–2 T respectively, which corresponds well to those reported in the literature for LAO/STO [80]. Thus, the SOC in AO/STO systems discussed in this work is most likely controlled by the Rashba effect as well.

The anisotropic behavior of B_{so} hints at additional contributions to the spin-orbit relaxation time, defining B_{so}. For Rashba-type SOC, the responsible spin-relaxation mechanism is described by the D'yakonov-Perel (DP) spin-relaxation mechanism (see section 1.5). However, other spin-relaxation mechanisms such as the Elliott-Yafet (EY) might be present alike [99–101].

The DP mechanism describes spin relaxation by a precession of the spin around the local magnetic field direction. Scattering events can change the axis of precession. Between two momentum scattering events, different spins accumulate different phases due to their precession movement. Thus the averaged spin relaxes over time, with the characteristic spin relaxation time τ_{so} proportional to $1/\tau$, where τ is the elastic scattering time.

The EY mechanism describes spin flipping during momentum scattering events. Scattering by impurities, phonons or boundaries can flip the spins and lead to an overall spin relaxation. This gives $\tau_{so} \propto \tau$. Both mechanisms usually take part in the spin relaxation. With the Drude model giving $\tau \propto \mu$ and Equation 1.11 giving $B \propto \tau^{-1}$, both spin-relaxation mechanisms are related to B_{so} by their mobility:

$$\begin{aligned} \mathrm{Elliott-Yafet:} \quad & B_{so} \propto 1/\mu \\ \mathrm{D'yakonov-Perel:} \quad & B_{so} \propto \mu \end{aligned} \tag{3.7}$$

Figure 3.13 displays a clear linear relation of the anisotropic part of the spin-orbit field $\Delta B_{so} = B_{so} - B_{so}(\mathrm{E})$ (see Figure 3.12(c)) to the inverse of the Hall mobility μ for the samples. This leads to the conclusion that defects and dislocations are a main source for anisotropic electrical transport in (001)-AO/STO, where predominantly the EY spin-relaxation mechanism contributes to the anisotropic magnetotransport. Magnetoresistance and Hall-resistance measurements of the high-miscut samples show the same general behavior as for the low-miscut samples just discussed. Fits to the magnetoconductance at $T = 2\,\mathrm{K}$ according to Equation 3.6 (as described in subsection 3.1.2) give values for the anisotropic spin-orbit field ΔB_{so}, which again show a linear behavior over the inverse of the Hall mobility. These values are included in Figure 3.13 and follow the same linearity as the low-miscut samples. Thus, in all (001)-oriented AO/STO samples the Elliot-Yafet spin-relaxation mechanism dominates the anisotropy in the transport, while the DP mechanism most likely dominates the isotropic spin relaxation.

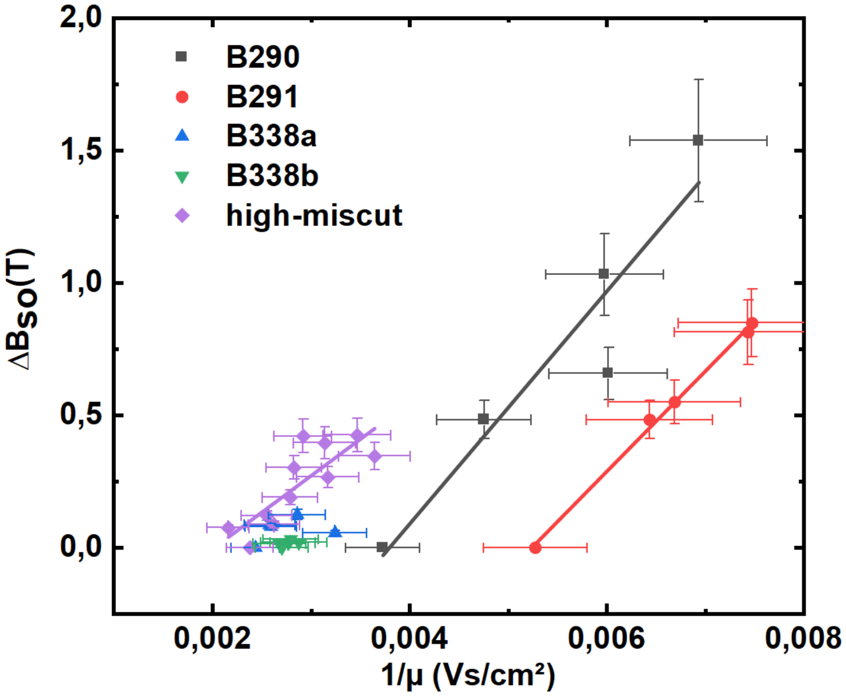

Figure 3.13.: ΔB_{so} as obtained by fitting the *MR* data according to Equation 3.6 plotted against the inverse of the Hall mobility for the microbridges of all (001) oriented samples. The linear behavior (solid lines) indicates the EY spin relaxation mechanism as dominant source for anisotropy. The different colors denote different of samples.

3.1.3. Magnetotransport for in-plane magnetic fields

In LAO/STO heterostructures, SOC-induced anomalous in-plane magnetoresistance (*AMR*) has been reported [18, 19, 80, 96]. The *AMR* is explained by Rashba-type SOC which arises from the polar mismatch at the interface between LAO and STO. Calculations of the band structure of (001) LAO/STO by Fête et al. [80] have shown that the presence of a Rashba term in combination with the 1D-like d_{xz} and d_{yz} subbands - caused by the large difference of the electron mass along the two orthogonal in-plane directions - results in a spin splitting and hence an energy gap at the Γ point for B_{ip} parallel to the current direction ($\phi = 0$), where the current direction is along the [100] or [010] directions.

In contrast, B_{ip} perpendicular to the current ($\phi = 90°$) causes only a Zeeman-like offset of the subbands.

Since AMR behavior in LAO/STO is obviously affected by Rashba-type SOC, measurements of the in-plane magnetotransport are suitable to probe Rashba coupling in AO/STO.

Figure 3.14 shows the amplitude of the magnetoconductance for the microbridges A, C and E of sample B290. Figure 3.14(a) shows a polar plot of $\Delta\sigma$ versus ϕ, the angle between the magnetic field and the (100) direction, while the cartesian coordinate plot in Figure 3.14(b) shows $\Delta\sigma$ versus the angle between the field and the current direction, $\theta = \phi - \varphi$, where φ is the current direction. All measurements here show a two-fold symmetry.

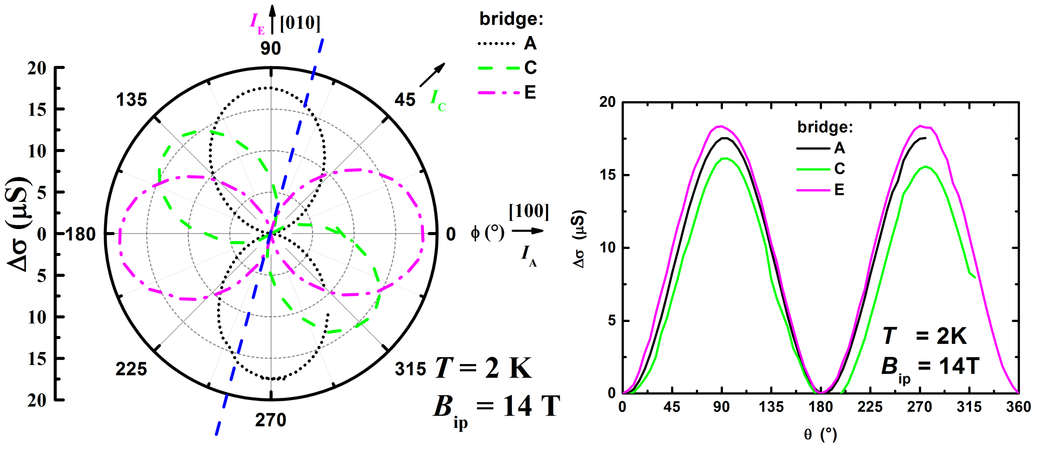

(a) (b)

Figure 3.14.: (a) Polar plot of the magnetoconductance for bridges A, C and E of sample B290 at $T = 2\,\mathrm{K}$ and $B_{ip} = 14\,\mathrm{T}$ as function of the angle between B_{ip} and the [100] direction. The dashed blue line gives the orientation of the step edges. (b) $\Delta\sigma$ plotted versus θ, displaying the non-crystalline character of the magnetoconductance.

The orientation of the step edges, indicated by the dashed blue line in Figure 3.14(a), does not alter the orientation or magnitude of the two-fold symmetry in any significant way. The position of the maxima for the microbridges A, C and E changes in steps of 45°, corresponding to the different orientation of the microbridges on the sample.

The minima of the two-fold oscillation of $\Delta\sigma$ dsiplayed in Figure 3.14b occur at the same angle $\theta = 0^\circ/180^\circ$ without significant phase shift. Thus, the angle between the magnetic field and the current dictates the extrema of the *AMR*. The origin of the *AMR* is therefore not crystalline in nature. The differences in the maximum amplitude $\Delta\sigma_{max}$ for A, C and E show the same trend as the maximum out-of-plane *MR* at $T = 2\,\mathrm{K}$ shown in Figure 3.10. Thus, they are probably related to to differences in μ and R_s of the the microbridges and most likely caused by the anisotropic distribution of dislocations.

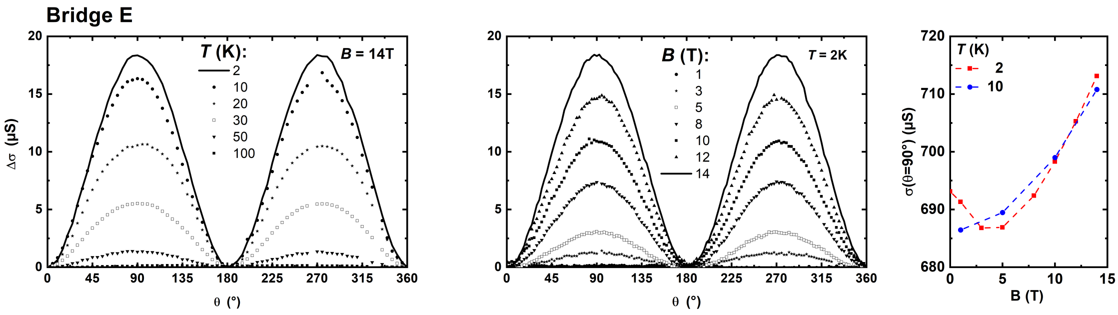

(a) (b) (c)

Figure 3.15.: $\Delta\sigma$ of bridge E at 14 T for different temperatures (a) and at 2 K for different magnetic fields (b) as function of the angle θ between current direction and magnetic field direction. (c) The maximum conductance versus B_{ip} with B_{ip} perpendicular to the current direction ($\theta = 90^\circ$) for bridge E at 2 K and 10 K.

Figure 3.15 gives more detail on the behavior of $\Delta\sigma(\theta)$ for microbridge E. Figure 3.15(a) shows $\Delta\sigma(\theta)$ for a magnetic field of $B = 14\,\mathrm{T}$ at various temperatures. The amplitude of $\Delta\sigma(\theta)$ increases with decreasing temperature, to a maximum of around 17 μS at $T = 2\,\mathrm{K}$. For $T \geq 100\,\mathrm{K}$ no significant angular dependence of $\Delta\sigma(\theta)$ could be measured. Figure 3.15(b) shows $\Delta\sigma(\theta)$ at $T = 2\,\mathrm{K}$ for magnetic fields up to 14 T. A noticeable amplitude is measured for $B \geq 3\,\mathrm{T}$ which increases with increasing field.

The field-dependent behavior of the maximum conductance $\sigma(\theta = 90^\circ)$ for 2 K and 10 K is shown in Figure 3.15(c). For both temperatures, $\sigma(\theta = 90^\circ)$ increases with increasing field $B_{ip} > 3\,\mathrm{T}$. Interestingly, for $T = 2\,\mathrm{K}$, the conductance first decreases with increasing field which may be attributed to WAL. In the low field range ($B_{ip} < 3\,\mathrm{T}$) at 2 K, the magnetotransport is strongly affected by WAL leading to an increase of conductance. Generally, WAL should not be sensitive to a magnetic field parallel to the 2DES. However, a finite thickness of the 2DES or misalignment of the magnetic-field direction resulting in a remaining out-of-plane field component, may result in a decoherence of the electronic phase as well.

Angular oscillations of magnetoconductance induced by Rashba effect in LAO/STO , i.e., $\Delta\sigma(\phi) \propto \sin^2(\phi)$ are only expected if charge transport is controlled by the d_{xz}, d_{yz} subbands. The Fermi level strongly depends on the charge carrier density, resulting to a Lifshitz transition at $n_c \approx 1.7 \times 10^{13}\,\mathrm{cm}^{-2}$. Above, n_c the d_{xz} and d_{yz} subbands are occupied [41]. For the AO/STO samples of this work, $n_s > 2 \times 10^{13}\,\mathrm{cm}^{-2}$ (see Figure 3.9).

The x and y directions are orthogonal to each other and thus the degeneracy of the d_{xz} and d_{yz} subbands leads to the same anisotropy $\Delta\sigma(\theta)$ for any current direction. This is also observed in our experiment. The specific angular dependence of $\Delta\sigma(\theta)$ in AO/STO thus suggests that the anisotropic transport is most likely caused by Rashba-type SOC, alike.

If it is assumed that $\Delta\sigma(\theta)$ is entirely caused by the d_{xz} and d_{yz} subbands closest to the Fermi energy E_F, the relative change $\Delta\sigma(B, \phi = 90°)/\sigma(B, 0) = 1/8(\Delta_{SO}/E_F)^2$, is directly related to the Rashba-induced spin-splitting energy Δ_{SO} [79]. For LAO/STO $\Delta_{SO}(B, \phi = 90°)/\sigma(B, 0) \approx 1.6\,\%$ at $B = 7\,\mathrm{T}$, resulting in $\Delta_{SO} = 7\,\mathrm{meV}$ for a zero-field conductance $\sigma_0 = 2\,\mathrm{mS}$, respectively [72, 80]. For AO/STO (B290), $\Delta\sigma(B, \phi = 90°)/\sigma(B, 0)$ increases from $0.2\,\%$ at $B = 3\,\mathrm{T}$ by $\approx 1\,\%$ at $8\,\mathrm{T}$ to $2.6\,\%$ at $B = 14\,\mathrm{T}$. Thus, for AO/STO Δ_{SO} seems to be smaller compared to LAO/STO.

The Rashba-type SOC depends on n_s [72] and on the electric field perpendicular to the interface [65] and thus the polarity of the heterostructure. For the epitaxially grown spinel-type/perovskite heterostructure γ-Al_2O_3/STO, the polar character and potential build-up is expected to be comparable to that of LAO/STO or even larger [45, 135]. A low deposition temperature T_s can lead to a strongly disordered and quasi-amorphous structure of Al_2O_3. However, TEM cross-sections at the interface still show a crystalline structure for the Al_2O_3 (see Figure 2.5). Because of n_s being close to that of LAO/STO, we assume that AO/STO displays polar character alike, however, probably weaker compared to LAO/STO or γ-Al_2O_3/STO heterostructures.

All data of the in-plane Hall resistance (R_{xy}) measurements have been corrected for wobbling as shown in Figure 2.9. Figure 3.16 shows measurements of R_s and R_{xy} for $T = 2\,\mathrm{K}$ and $B_{ip} = 14\,\mathrm{T}$ of microbridges A, C and E as a function of θ. R_s and R_{xy} both show a perfect two-fold symmetry and can be described by a sine function, with a phase shift of 45° between R_s and R_{xy}. The amplitude of R_s decreases slightly from A to E, while the amplitude of R_{xy} is largest for bridge C ($R^C_{xx} \approx R^C_{xy}$) and smaller for A and E. For a homogeneous 2DES, the difference $\Delta = (R_{max} - R_{min})$ is the same for R_{xx} and R_{xy}. However, $\Delta(\theta)$ for R_{xx} is shifted by 45° with respect to that of R_{xy} [136]. Equation 3.8 gives

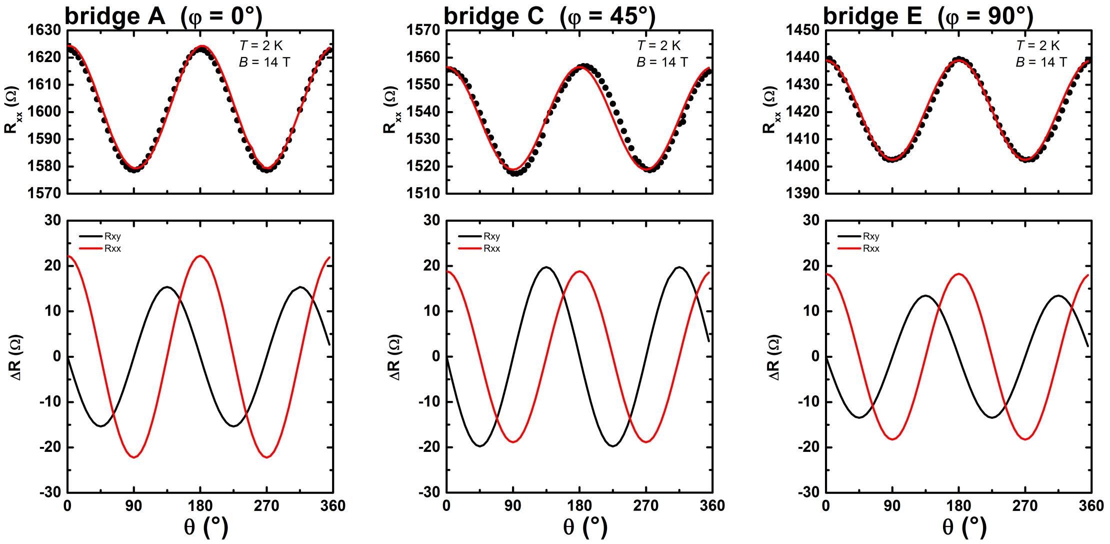

Figure 3.16.: Comparison of the in-plane magnetoresistance at $T = 2\,\mathrm{K}$ and $B_{ip} = 14\,\mathrm{T}$ for bridges A, C and E. (upper row). The solid lines are fits to the data. (lower row) Corresponding amplitudes of R_{xx} and R_{xy} versus θ. ΔR_{xx} is shifted by 45° with respect to ΔR_{xy}. The different amplitudes (by about 20 %) are attributed to inhomogeneities of the 2DES.

the resistance modulations expected for a homogeneous system:

$$\begin{aligned} R_{xx} &= R_{xx}^{av}\left(1 + \frac{\Delta}{2}\cos(2\theta)\right) \\ R_{xy} &= -R_{xx}^{av}\,\frac{\Delta}{2}\sin(2\theta). \end{aligned} \tag{3.8}$$

The results shown in Figure 3.16 follow the amplitude shift given in Equation 3.8, but the amplitudes themselves are not the same. Thus, our system is inhomogeneous, which is most likely due anisotropic defect scattering.

3.2. Anisotropic electronic transport of (110)-oriented AO/STO heterostructures

AO/STO heterostructures on (110)-oriented STO substrates have been manufactured as described in section 2.1. The structured microbridges allow to probe 4-point resistance along different crystallographic orientations, in five steps from [001] to [1$\bar{1}$0]. Figure 3.17 shows a micrograph of the patterned Hall bars along with an AFM micrograph of the STO surface before the patterning process.

The step edges of this sample have a height of around 2.76 Å (= $a/\sqrt{2}$, where $a = 3.905$ Å) and a width of around 80 nm. They are oriented by an angle of $\phi \approx 70^\circ$ with respect to the [001] direction. The impact of the step edges and dislocations on the anisotropy of electronic transport is expected to be insignificant compared to the anisotropy of the electronic band structure of (110) oriented LAO/STO heterostructures [18, 19, 137, 138], since the step edges are less pronounced in comparison to (001) oriented STO. The dislocations line are most likely homogeneously distributed in the conducting plane or perpendicular to it [130], resulting in isotropic contributions to the transport. In LAO/STO, the largest resistance is expected for the current along the [1$\bar{1}$0] direction, due to weaker dispersion and smaller band width for the lowest electronic subbands along the [1$\bar{1}$0] ($\Gamma - M$) direction as compared to the [001] ($\Gamma - Z$) direction.

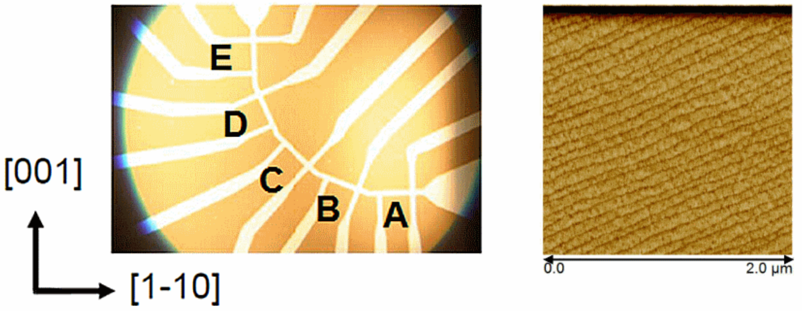

Figure 3.17.: Micrograph of the structured microbridges on sample B297 with (110) surface orientation. The microbridges are $17 \times 100\,\mu m^2$ in size. There are no residual particles in the conducting area. The right hand side shows an AFM micrograph in friction mode of the STO surface before the deposition of AO, demonstrating step edges with a width of about 80 nm.

3.2.1. Temperature dependence

Figure 3.18 shows the sheet resistance R_s for the microbridges A-E of a (110)-oriented AO/STO heterostructure as a function of temperature from 300 K to 2 K. The electronic transport in (110)-oriented AO/STO heterostructures shows anisotropic transport at low T comparable to LAO/STO [17].

Above $T = 100\,\mathrm{K}$, all microbridges show a T^2 behavior. At $T \approx 20\,\mathrm{K}$, R_s shows a shallow minimum, before again rising slightly towards 2 K. The temperature dependence for each bridge is similar to that of (001)-oriented AO/STO heterostructures, resulting in a resistance ratio of about 20 for R_s at 300 K and 10 K. The T dependence is well described by electron-phonon interactions and impurity scattering as described by Equation 3.2. The fits indicated in Figure 3.18 are in almost perfect agreement with the measured data.

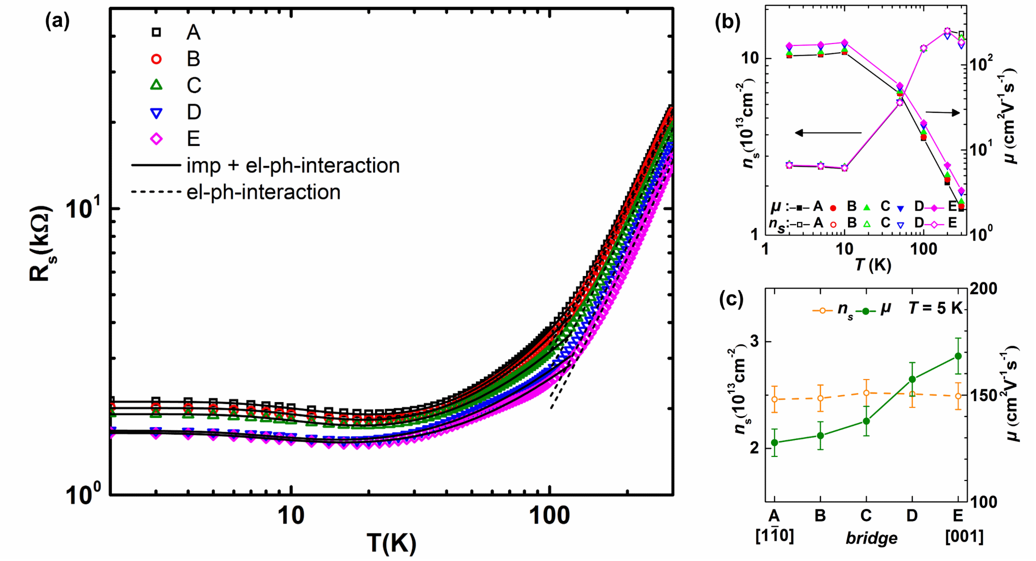

Figure 3.18.: Sheet resistance versus temperature for the microbridges A-E (from A || [1$\bar{1}$0] to E || [001]) (a). Sheet carrier density n_s and Hall mobility μ versus temperature (b) and for the five microbridges A-E at $T = 5\,\mathrm{K}$ (c).

Obviously, R_s decreases continuously from bridge A (I || [1$\bar{1}$0]) to bridge E (I || [001]) for all temperatures from 300 K to 2 K. Thus, anisotropic transport is not only restricted to the low-temperature regime, where usually impurity scattering dominates the anisotropic electronic transport. Between 300–5 K, the anisotropy decreases with decreasing temperature from 47 % to 29 %. This rather weak T dependence suggests that the intrinsic electronic band structure for [1$\bar{1}$0] and [001] is likely the dominant source for the anisotropy in the electronic transport.

Hall resistance measurements in an out-of-plane magnetic field in the range of $-14\,\mathrm{T} \leq B \leq 14\,\mathrm{T}$ and at temperatures $2\,\mathrm{K} \leq T \leq 300\,\mathrm{K}$ allow to extract the T dependence of the sheet carrier density n_s and the Hall mobility μ. Below $T = 30\,\mathrm{K}$, the Hall resistance R_{xy} starts to show small deviations from linear behavior at higher magnetic fields, which indicate multi-type carrier transport.

This behavior is similar to that of (001)-oriented AO/STO heterostructures. The total sheet carrier density was deduced from the asymptotic values of R_{xy} at high magnetic fields. Deviations from the values extracted at small magnetic fields close to $B = 0$ are smaller than 10 %. Figure 3.18 (b) shows the total n_s and μ for all microbridges in the range of 2–300 K. The total n_s decreases with temperature from around $1.3 \times 10^{14}\,\mathrm{cm}^{-2}$ at 300 K to $2.5 \times 10^{13}\,\mathrm{cm}^{-2}$ at 5 K, which matches the reports for (110) LAO/STO heterostructures quite well [23].

The mobility μ increases with decreasing temperature, from roughly $2.5\,\mathrm{cm}^2/\mathrm{Vs}$ at room temperature to around $150\,\mathrm{cm}^2/\mathrm{Vs}$ at 5 K. The temperature dependence of both, n_s and μ, is in good agreement to that of (001) LAO/STO and AO/STO heterostructures (section 3.1, [8, 17, 26]). Analogously to R_s, the anisotropy of n_s and μ is largest at $T = 300\,\mathrm{K}$, amounting up to 16 % and 65 %, respectively. With decreasing T the anisotropy decreases to 2 % for n_s and 34 % for μ at 5 K. At low temperatures, the anisotropy in R_s thus is caused by the anisotropy in μ, while n_s is almost the same for the different microbridges (Figure 3.18 (c)).

The anisotropic transport persistent in the whole range of 2–300 K is in contrast to the anisotropic transport in (001) AO/STO (see section 3.1), where the anisotropy is caused extrinsically by the inhomogeneous distribution of dislocations along the $[1\bar{1}0]$ and [110] directions [26]. Effects caused by lattice distortions may be responsible for the lower anisotropy at low temperatures in (110) AO/STO, slacking and masking the intrinsic anisotropy caused by the band structure. The temperature dependence of n_s is most likely caused by charge carrier trapping, often referred to as carrier freeze-out.

3.2.2. Magnetic field dependence

Measurements of the *MR* with the magnetic field perpendicular to the sample surface have been performed with the same routine as described in subsection 3.1.2. For $T \geq 50\,\mathrm{K}$, only a small, positive *MR* of about 2 % at $B = 14\,\mathrm{T}$ is found. The *MR* displays no distinct anisotropy with respect to the crystallographic directions.

Figure 3.19 shows the *MR* for all the microbridges at $T = 10\,\mathrm{K}$ and 2 K, as well as WAL fits to the *MR* at 2 K. At $T = 10\,\mathrm{K}$, *MR* is dominated by classical Lorentz scattering and hence perfectly described by the Kohler rule (Equation 3.5). Fits are indicated by solid black lines. *MR* is largest for bridge E ($I \parallel [001]$) and smallest for bridge A ($I \parallel [1\bar{1}0]$) very similar to the anisotropic behavior of the mobility (see Figure 3.18).

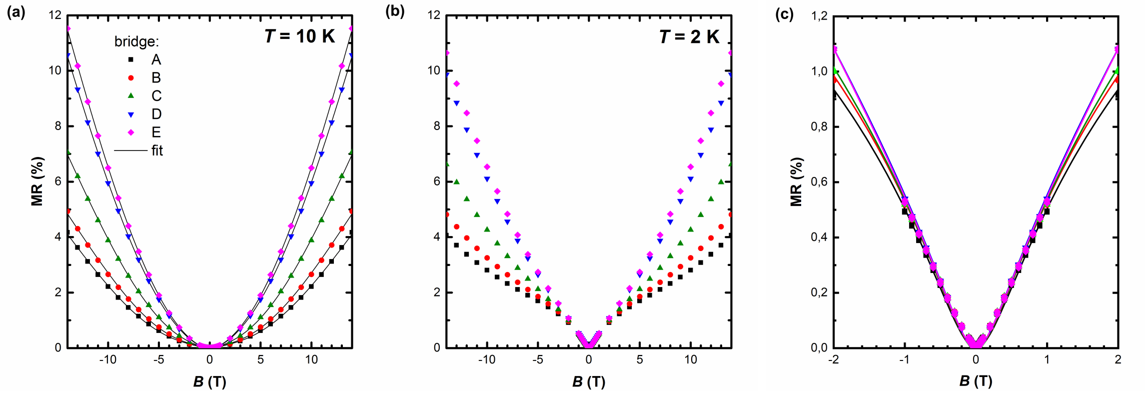

Figure 3.19.: Magnetoresistance measurements for the different microbridges A-E of B297 with out-of-plane magnetic field direction. (a) *MR* at 10 K with fits (solid lines) according to Equation 3.5. (b) *MR* at $T = 2\,\mathrm{K}$. WAL emerges and dominates at small magnetic fields. (c) *MR* in the low field range for $B < B^*$ at 2 K. Fits to the data by Equation 3.6 are shown by solid lines.

At $T = 2\,\mathrm{K}$, the WAL contribution dominates the low field behavior of *MR*, while at higher magnetic fields *MR* is comparable to that at 10 K. Figure 3.19(c) shows WAL at $T = 2\,\mathrm{K}$ in the regime where it is dominated by WAL. Fits to the WAL were performed within the phase-coherence limit $B < B^*$, with $B^* = \hbar c/2e \cdot l_m^2$ and the electronic mean free path $l_m = 12\,\mathrm{nm}$ for this sample, resulting in $B^* \approx 2\,\mathrm{T}$. The fits according to the Maekawa-Fukuyama theory including Zeeman corrections (see Equation 3.6) result in in an almost perfect description of the data, shown in Figure 3.19(c). The fitting parameters B_i and B_{so} for the microbridges A-E are shown in Figure 3.20. For all microbridges $B_i \approx 180\,\mathrm{mT}$ and $B_{so} \approx 0.5$–$0.6\,\mathrm{T}$. B_i and B_{so} show values well comparable to those found for (001) AO/STO or LAO/STO heterostructures where Rashba-type SOC is dominant.

However, in contrast to the (001) AO/STO heterostructures, for the (110) AO/STO the characteristic magnetic fields B_i and B_{so} do not display anisotropic behavior. Therefore, anisotropic SOC via EY spin relaxation due to anisotropic defect scattering seems to play no significant role here, which is in agreement with the assumption of mostly isotropic contributions from dislocation lines along the [110] and $[1\bar{1}0]$ directions to the transport in (110) AO/STO. Compared to the WAL corrections, Zeeman corrections are not relevant.

In comparison to WAL, the LS contributions are minor for $B \leq 2T$ and dominate at large fields $B \geq 8\,\mathrm{T}$ where WAL is usually negligible. However, the anisotropy of the *MR* with respect to the microbridges for $B \geq 8\,\mathrm{T}$ is larger at $T = 10\,\mathrm{K}$ than at 2 K. In contrast, the

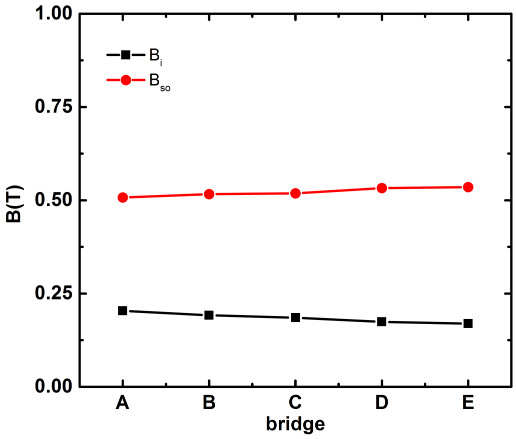

Figure 3.20.: Parameters of the fits to the WAL contribution at 2 K according to Equation 3.6. No significant anisotropy for the microbridges is found for B_i and B_{so}.

anisotropy of R_0, μ and n_s increases with decreasing temperature from 10 K to 2 K and may not explain this behavior. It might be possible that WAL contributions for large magnetic fields, as predicted by theory [139–141], are able to influence the anisotropy.

On the other hand, Rashba-type SOI is expected to be anisotropic and may lead to anisotropic *MR* at high fields. For example, angle-resolved photoemission spectroscopy (ARPES) experiments on (110)-oriented STO surfaces showed anisotropic Rashba spin splitting [18, 137]. Similar effects have been discussed for (110) LAO/STO heterostructures [17, 19]. If WAL contributions to the *MR* can be neglected, which is the case for magnetic fields applied parallel to the interface (see section 1.4), the Rashba effect can be examined in more detail.

3.2.3. Magnetotransport for in-plane magnetic fields

In this section, *AMR* measurements of the microbridges A ($I \parallel [1\bar{1}0]$) and E ($I \parallel [001]$) in magnetic fields B_{ip} of up to 14 T with different orientations with respect to the current are discussed.

Figure 3.21 shows the sheet resistance R_s for bridges A and E measured at $T = 2$ K for various magnetic fields up to 14 T versus the angle ϕ with respect to the [001] direction within the plane of conduction. The two-fold, sinusoidal oscillations show maxima at $\phi = 90°/270°$ and $0°/180°$ for bridges A and E respectively.

This clearly indicates that, as in (001) AO/STO, the anisotropy depends dominantly on the angle between the current direction and the in-plane magnetic field B_{ip} and not on the crystallographic direction [142]. The maxima in R_s occur always for the magnetic field parallel to the current path. The *AMR* increases continuously with increasing B_{ip}, and

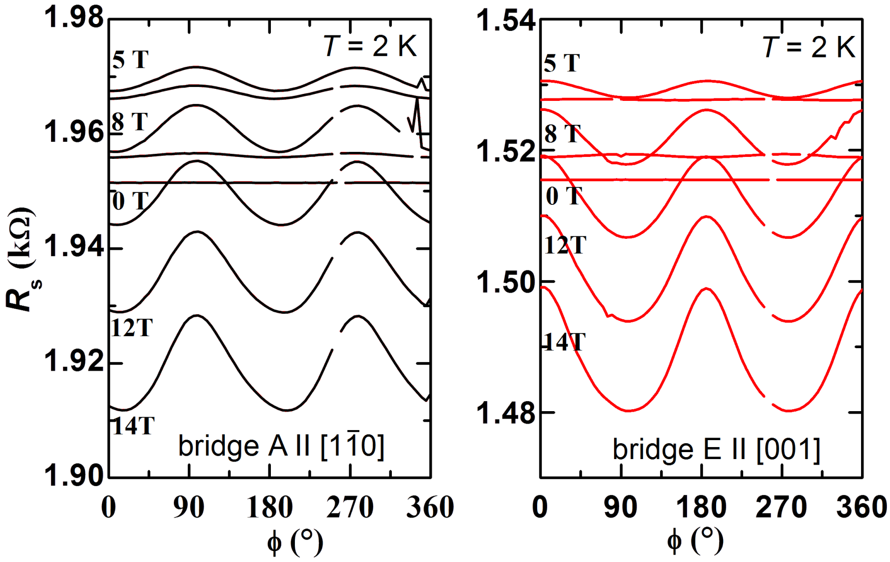

Figure 3.21.: R_s versus the in-plane angle ϕ between the magnetic field and the [001] direction for fields up to 14 T for microbridges A and E aligned parallel to the [1$\bar{1}$0] and [001] direction, respectively . The maxima occur for $B_{ip} \parallel I$ for both microbridges.

reaches about 1 % for microbridge A and 1.4 % for E at 14 T. Compared to the out-of-plane MR in (001) and (110) AO/STO it is thus about one order of magnitude smaller.

R_s increases first with increasing B_{ip} up to 5 T before decreasing with further increasing field to values below $R_s(B = 0)$. This behavior is examined in more detail in Figure 3.22. It shows the in-plane magnetoresistance at $T = 2$ K for microbridges A and E versus B_{ip} for the field direction parallel ($\theta = 0°$) and perpendicular ($\theta = 90°$) to the current direction. For $\theta = 0°$ the in-plane magnetoresistance is faintly larger than for $\theta = 90°$. The MR_{ip} shows a maximum at $B_{ip} \approx 5$ T and takes negative values for magnetic fields ≥ 10 T. The negative MR_{ip} may be attributed to the Zeeman effect, which by spin-polarization leads to a decrease of interband scattering with increasing B_{ip} at higher magnetic fields [81]. Zeeman corrections are expected to be largest for magnetic field perpendicular to current direction, which may explain the larger negative MR for $\theta = 90°$.

The temperature dependent anisotropy $\Delta\sigma$ of B297 at $B_{ip} = 14$ T shown in Figure 3.23 displays a rather surprising behavior. The minima of $\Delta\sigma$ for A and E are shifted by 90° with respect to each other, confirming the noncrystalline angular dependent anisotropy. The amplitudes $\Delta\sigma_{max}$ plotted versus the temperature reveals differences between bridge A and E for 20 K. The amplitude $\Delta\sigma_{max}$ of bridge A decreases much faster with decreasing temperature than that of bridge E. This anisotropic behavior might indicate different tem-

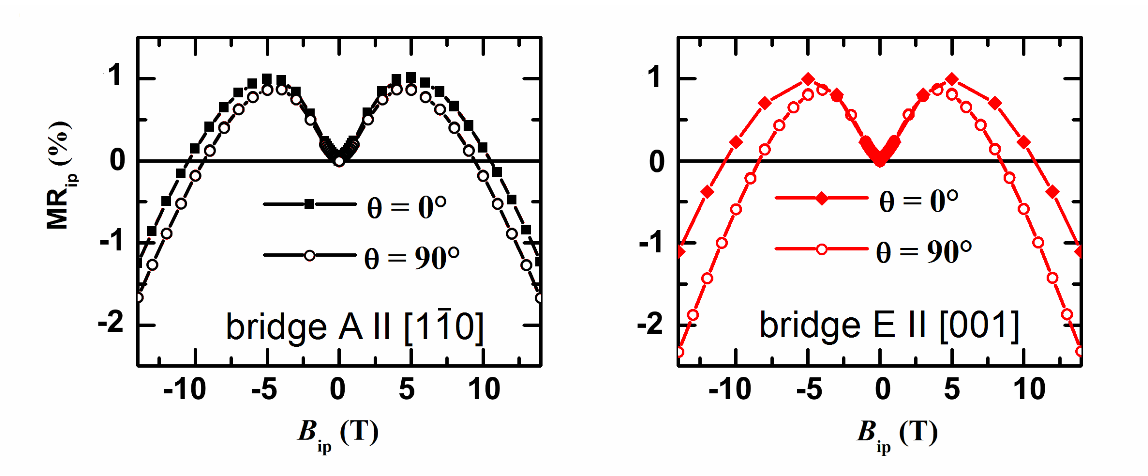

Figure 3.22.: MR_{ip} for bridge A and E versus B_{ip} for the field direction parallel ($\theta = 0^{\circ}$) and perpendicular ($\theta = 90^{\circ}$) to the current direction.

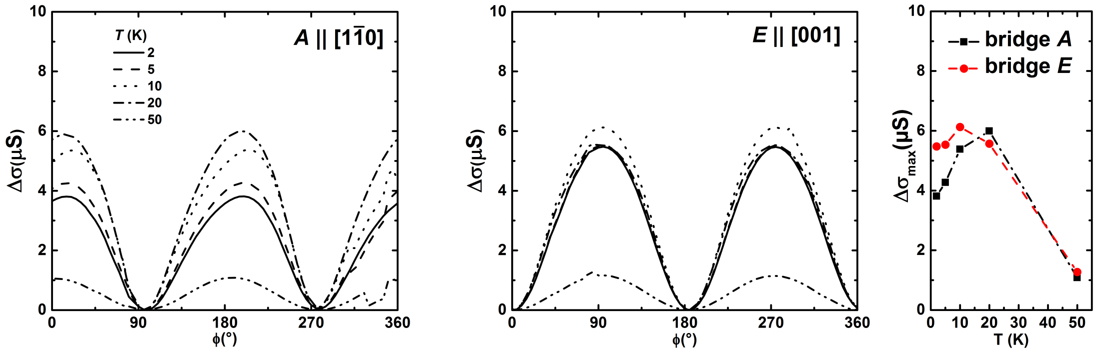

(a) (b) (c)

Figure 3.23.: Amplitude of the angular oscillations in the conductivity for bridges A (a) and E (b) along the [1$\bar{1}$0] and [001] direction respectively. Measurements were performed at $B = 14$ T in the temperature range of 2–50 K and plotted versus ϕ, the angle between the magnetic field and the [001] direction. (c) The maximum amplitude $\Delta\sigma_{max}$ versus the temperature.

perature sensitivity of the electronic band structure along the two different crystallographic directions, resulting in different band fillings and mobilities.

The anomalous magnetoconductance (AMC) $= \left[\sigma(B_{ip},\theta) - \sigma(B_{ip},0)\right]/\sigma(B_{ip},0)$ is displayed for $B_{ip} = 14\,\mathrm{T}$ and $T = 2\,\mathrm{K}$ for both current directions in Figure 3.24. For both directions, [1$\bar{1}$0] and [001], the maxima of the AMC occur at $\theta = 90°$ and 270°. The maxima at the magnetic field perpendicular to the current amount to 1.3 % and 0.8 % for the [001] and [1$\bar{1}$0] direction, respectively. Detectable AMC appears for magnetic fields larger than 3 T and shows a nearly quadratic behavior with increasing B_{ip} up to fields of around 10 T. Obviously, the increase is different for both crystallographic directions, which might indicate anisotropic Rashba coupling.

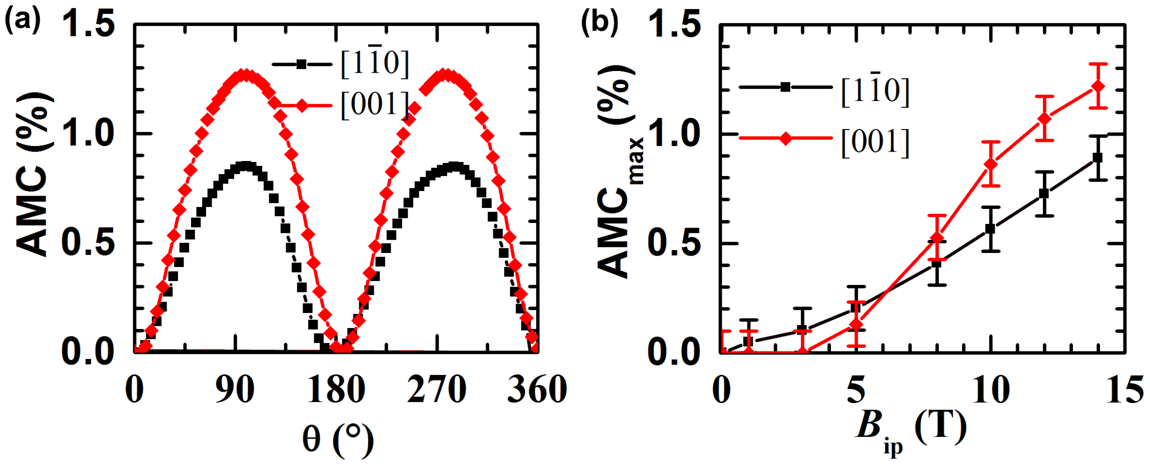

Figure 3.24.: (a) Anomalous magnetoconductance versus θ at $T = 2\,\mathrm{K}$ and $B_{ip} = 14\,\mathrm{T}$. (b) The amplitude of magnetoconductance oscillations, AMC$_{max}$, for the directions [1$\bar{1}$0] and [001] versus the in-plane magnetic field strength.

The two-fold oscillations of the magnetoconductance of (110) AO/STO are similar to those found in (001) LAO/STO and AO/STO. In previous work by Fête et al. it was shown that Rashba-type SOC can in induce the two-fold noncrystalline angular oscillations of the magnetoconductance [80]. For moderate magnetic fields, the amplitude $\Delta\sigma$ of the oscillations scales with the square of the spin-orbit energy, i.e., $\Delta\sigma_{max} = \left[\sigma(B_{ip},90°) - \sigma(B_{ip},0°)\right]/\sigma(B_{ip},0°) \propto \Delta_{so}^2$ for moderate magnetic field strengths. The (110) AO/STO heterostructure presented in this work shows a similar behavior (Figure 3.24). Therefore, it is very likely that the AMR (AMC) in (110) AO/STO is dominated by Rashba type SOC.

3.2.4. Theoretical modeling of the electronic band structure

To obtain a better understanding of the measured anisotropy in the electronic transport, linear combination of atomic orbitals (LCAO) calculations of the electronic band structure for the (110) AO/STO interface were carried out by Robert Eder (IFP). More details on these tight-binding calculations are given in Ref. [142]. The energy bands $E_{\nu,\boldsymbol{k}}$ are labeled by the band index ν. $\boldsymbol{k}$ is the wave vector in the rectangular Brillouin zone. The band structure obtained this way is shown in Figure 3.25.

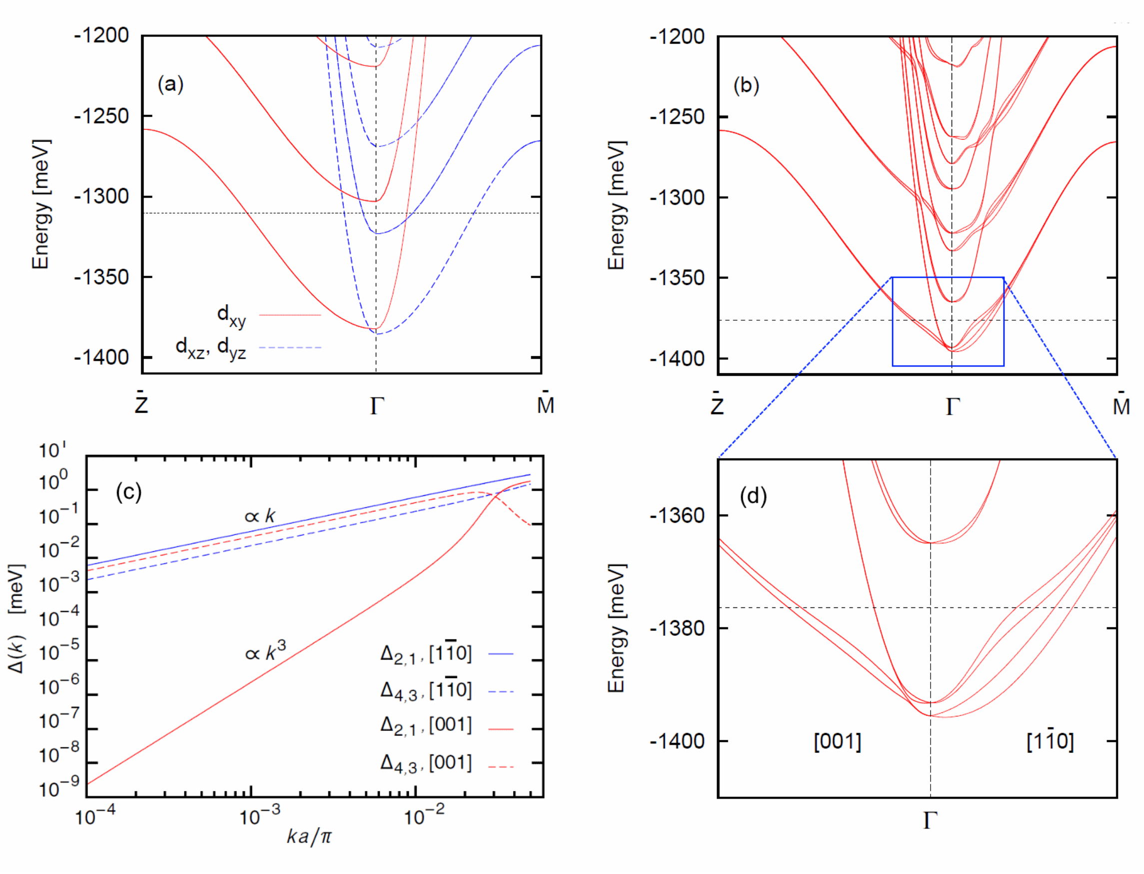

Figure 3.25.: Electronic band structure for (110) AO/STO obtained by LCAO calculations. (a) Band structure without SOC and symmetry breaking electric field. Spins are two-fold degenerate, the horizontal line gives the Fermi energy for 0.4 e/unit-cell. (b) Band structure with SOC and symmetry breaking electric field normal to the interface at $B = 0$. The horizontal line is the Fermi energy for 0.05 e/unit-cell. (c) Rashba-induced band splittings $\Delta_{\nu,\nu'}(\boldsymbol{k})$ near Γ along the two symmetry lines of the Brillouin zone. (d) Close-up view of dashed box in (b).

When SOC and the symmetry breaking electric field usually present in AO/STO are neglected, the calculations give the band structure shown in Figure 3.25a. It roughly agrees with the band structure obtained by Wang et al. [137] using fits to their ARPES data. Deviations are due to modified hopping terms in this calculation compared to Ref. [137]. The three t_{2g} orbitals show no intermixing. Thus the bands can be classified by their corresponding type of d orbitals where bands derived from d_{xz} and d_{yz} orbitals are degenerate. The horizontal line gives the Fermi energy for an electron density of 0.4 e/unit-cell (1.8×10^{14} cm^{-2}), corresponding to the experiments by Wang et al. [137]. The various subbands are generated by the confinement of the electrons in z direction.

Figure 3.25 (b) and (c) show the band structure with an electric field in z-direction and finite SOC, while $B = 0$. The horizontal lines give the Fermi energy for an electron density of 0.05 e/unit-cell or 2.3×10^{13} cm^{-2}, which is close to our experiment. Changing the density in the range of 0.04 e/unit-cell $\leq n_s \leq$ 0.07 e/unit-cell results only in minor changes of the magnetoresistance.

Near the Γ-point, linear ($\propto \boldsymbol{k}$) and cubic ($\propto \boldsymbol{k}^3$) Rashba-induced band splitting is found, as already discussed by Zhong et al. [143]. A new gap forms at Γ, where the lowest d_{xy}-derived band along $\Gamma - \bar{M}$ combines with one d_{xz}/d_{yz}-derived band along $\Gamma - \bar{Z}$. The newly formed mixed band is shifted upwards by about 20 meV. If the bands are labeled in order of ascending energy with 1 being the lowest, the calculations give cubic Rashba spin-splitting between bands 1 and 2 in [001] direction and linear splitting along [1$\bar{1}$0] direction. Splitting between bands 3 and 4 is linear for both directions (see Figure 3.25(c)). This emphasizes the anisotropic character of the Rashba-effect at the (110) AO/STO interface which most likely influences the electronic transport (see subsection 3.2.1).

Introducing a magnetic field in the (x,y) plane leads to shifts and small changes of the Fermi sheets corresponding to the bands 1 to 4. The displacement is perpendicular to the magnetic field direction and larger for $B \parallel [001]$ than for $B \parallel [1\bar{1}0]$. This behavior is qualitatively derived from a simplified single-band model [79] with a Hamiltonian of the form

$$H = \frac{p^2}{2m} + \alpha \boldsymbol{\tau} \cdot (\boldsymbol{p} \times \boldsymbol{e}_z) - \omega_s \boldsymbol{\tau} \cdot \boldsymbol{B}. \tag{3.9}$$

Here α denotes the strength of the Rashba coupling, $\boldsymbol{\tau}$ the vector of the Pauli matrices and $\omega_s = \mu_B B$. The directions of the calculated displacement indicates $\alpha < 0$ for the outer sheets 1 and 2 and $\alpha > 0$ for the inner sheets 3 and 4. The variation of the calculated 'band resolved' conductivities is shown in Figure 3.26. The contributions are summed over pairs of bands, having similar Fermi-surface geometry and shift in opposite direction in a magnetic field. ϕ denotes again the angle between the magnetic field and the [001]-direction.

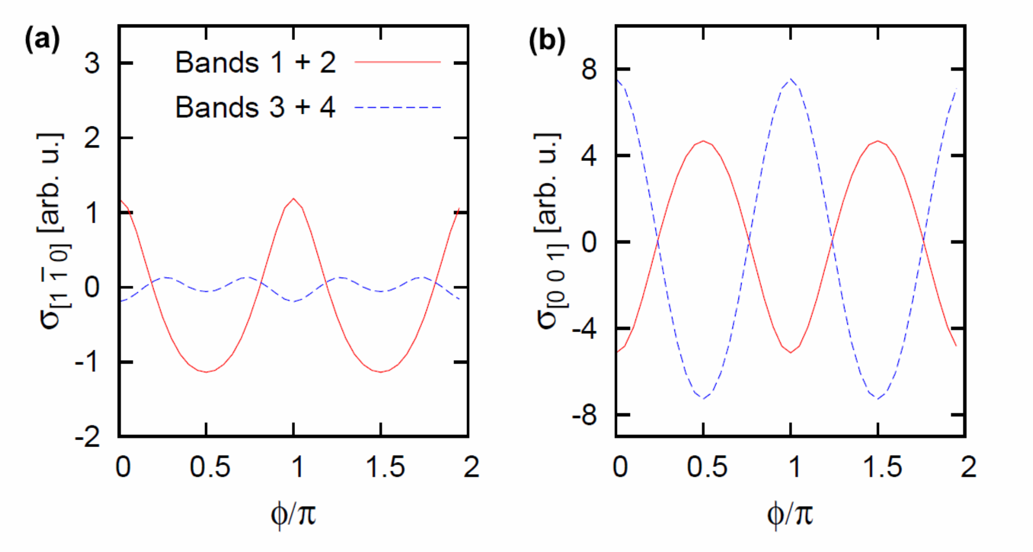

Figure 3.26.: Angular variation of $\sigma_{[1\bar{1}0]}$ (a) and $\sigma_{[001]}$ (b) for $B = 14\,\mathrm{T}$ where ϕ denotes the angle between B and [001]-direction. A contribution to σ independent of ϕ has been subtracted.

The variation of the conductivity for each band with the field direction ϕ follows the form

$$\sigma \approx A_0 + A_2 \sin(2\theta) + A_4 \sin(4\theta) \tag{3.10}$$

where θ is the angle between the magnetic field and the current direction. For bands 1 and 2 the constant A_2 is negative and much larger than A_4. For bands 3 and 4, the $[1\bar{1}0]$ direction shows four maxima, with $A_4 \gg A_2$ and A_2 being positive, while for the [001] direction $A_2 \gg A_4$. In contrast to bands 1 and 2, A_2 is positive here. The significant admixture of A_4 for band 3+4 along the $[1\bar{1}0]$ direction and the sign change in A_2 for band 1+2 and band 3+4 along the [001] direction is different from the behavior described by simpler models which only cover two-fold oscillations [79]. The direction-dependent displacement of the Fermi sheets suggests that the effective Rashba parameter for bands 3 and 4 depends on the direction of the magnetic field.

Agreement with experiment could be obtained only by choosing a band-dependent relaxation time, more precisely the relaxation time $\tau_{1,2}$ for the bands 1 and 2 had to be chosen larger by roughly a factor 4 as compared to $\tau_{3,4}$ for bands 3 and 4. Thereby both $\tau_{1,2}$ and $\tau_{43,4}$ need to vary slightly with magnetic field to obtain a reasonable fit as shown

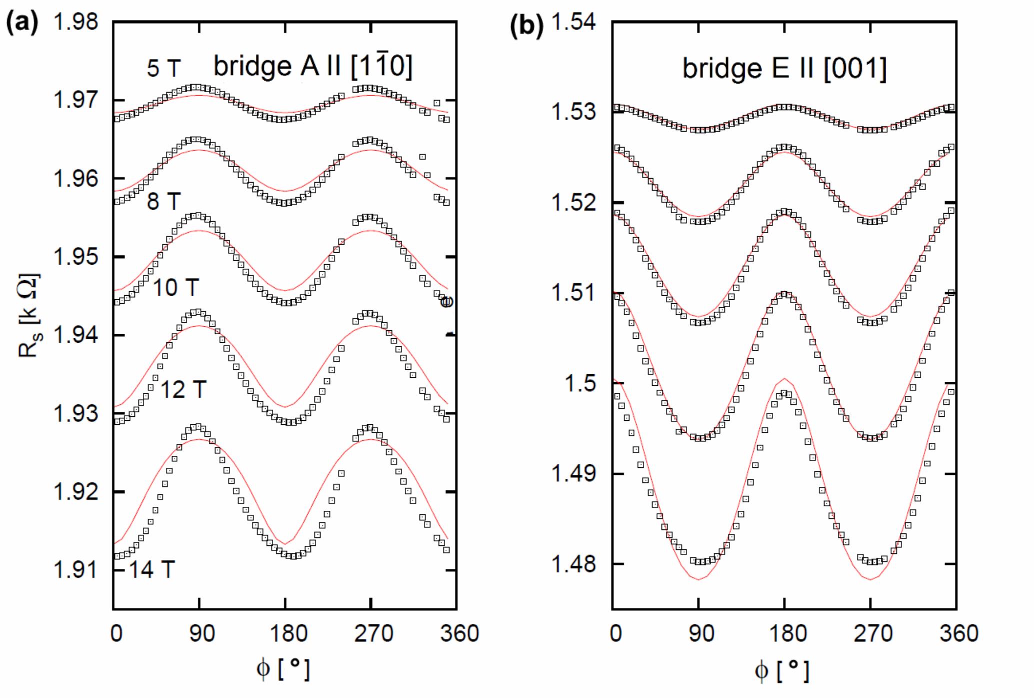

Figure 3.27.: Calculated sheet resistance (lines) versus angle between magnetic field and [001] direction compared to the experimental data (see Figure 3.21) for (a) the current direction along [1$\bar{1}$0] and (b) along the [001] direction.

in Figure 3.27. The figure displays the calculated ϕ dependence of the resulting sheet resistance in comparison with the experimental data already discussed in Figure 3.21. The agreement for microbridge E (current along [001]) is quite good, while for microbridge A (current along [1$\bar{1}$0]) there is a discrepancy in the shape of the oscillation. The simulation shows sharp minima and wide maxima, which is opposite to the experimental data. This is most likely due to limitations of the semi-classical Boltzmann approximation, where only the exact solutions would give an exact reproduction of the experimental data [81].

3.2.5. Backgating experiments

The simulations shown in Figure 3.27 for fixed charge carrier density n_s and Rashba-coupling strength α give rise to the question in which way these properties affect the magnetotransport in AO/STO heterostructures. Gating experiments are suitable to change both quantities simultaneously by applying an electric field perpendicular to the conducting interface [144, 145].

For that reason, gating-experiments were carried out on the same sample used above by providing an additional electrode to the back side of the AO/STO heterostructure. First, the sample was thinned down from the backside at the LEM (Laboratory for Electron

Microscopy, KIT) while precautions were taken to protect the surface. The thickness was reduced from 1 mm to 0.2 mm to gain a factor of five in the resulting electric field perpendicular to the interface for the same gate voltage. The maximum gate voltage V_g was limited to 50 V because of safety protections for the PPMS.

The gate electrode was applied by sputtering platinum on the back side of the substrate. Figure 3.28 shows the minimum sheet resistance R_0, versus gate voltage V_g for $B_{ip} = 1, 5$ and 14 T. For $V_g > 0$, electrons are introduced into the channel. Therefore, R_s decreases with increasing V_g. Both microbridges *A* and *E* show an exponential decrease of R_0 with increasing V_g. The back-gate effect seems to be similar for both bridges and does not depend on the strength of applied magnetic fields. For $V_g = 5$ V and $B_{ip} = 11$ T, R_0 of bridge *A* and *E* is around 28 kΩ and 16 kΩ, decreasing to 2.2 kΩ and 1.6 kΩ for $V_g = 24.91$ V, respectively.

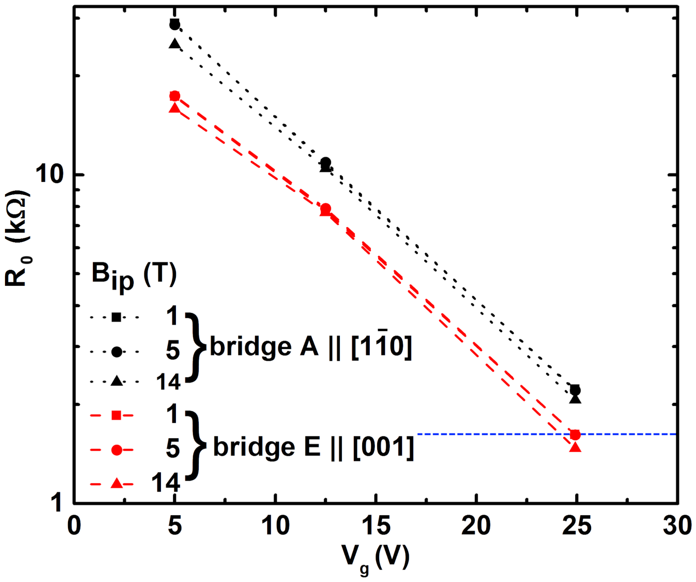

Figure 3.28.: R_0 obtained from AMR measurements at different B_{ip}. R_0 decreases exponentially with increasing V_g. The dashed blue line indicates the resistance level for bridge *E* at $B_{ip} = 1$ T before the sample was thinned.

A gate voltage of $V_g = 24.91$ V was necessary to achieve the same resistance levels as before the thinning process. Increasing V_g beyond 25 V results in strong electronic drifts and unstable conditions. Therefore, V_g was limitted to +25 V. On the other hand, reducing V_g to +5 V results in an increase of R_s close to the threshold for resistance measurements. For $V_g = 0$, the sample was insulating, indicating that despite all precautions the thinning altered the sample's resistance.

Figure 3.29 shows *AMR* measurements for $V_g = 5$, 12.5 and 24.91 V at $B_{ip} = 1, 5$ and 14 T for both microbridges, A (along the $[1\bar{1}0]$) and E (along the [001] direction). The symbols show the experimental data and the solid lines show fits to the data according to:

$$R_s = R_0 + R_2 \cos(\phi)^2 + R_4 \cos(2\phi)^2,$$

where $AMR = (R_s - R_0)/R_0$. The amplitudes of the two-fold oscillation R_2 and of the four-fold oscillation R_4 correspond to the amplitudes A_2 and A_4 given by Equation 3.10.

For $B_{ip} = 1$ T, shown in Figure 3.29 (a) and (b), *AMR* for the microbridges A and E shows two-fold angular oscillations dependent on ϕ with maxima at $\phi = 0°$ and 180°. The amplitude decreases with increasing V_g. At $V_g = 5$ V and 12.5 V, the two-fold *AMR* is similar for both bridges, while at 24.91 V the amplitude for *E* is only about half that of bridge A.

For $B_{ip} = 5$ T, shown in Figure 3.29 (c) and (d), *AMR* for A and E shows similar ϕ-dependence for the two lower gate voltages. The two-fold oscillations show wide minima and narrow maxima, which may be caused by a superposition of a dominating two-fold and a minor four-fold oscillation. For $V_g = 24.91$ V, R_2 shows a sign change for bridge E, with an *AMR* of 0.9 %, compared to 0.6 % for bridge A.

Figure 3.29 (e) and (f) show the *AMR* for $B_{ip} = 14$ T. At $V_g = 5$ V, both microbridges show a dominating contribution of R_2 admixed with a smaller contribution of R_4. The total *AMR* is about 1 % which is well comparable to the earlier results without backgating. For 12.5 V, *AMR* of bridge A shows the same characteristics as before at 5 V, but of reduced magnitude. For bridge E, a nearly perfect four-fold oscillation is measured. At $V_g = 24.91$ V, *AMR* of bridge A is dominated by a positive R_2 with a smaller, negative R_4 giving a total modulation of about 1.5 %. The *AMR* of microbridge E is dominated by a negative R_2 with a minor positive R_4, adding up to a total modulation of R_s by 8 %.

The results in Figure 3.29 show that altering the band filling and the strength of the Rashba-SOC by applying a gate voltage drastically changes the angular dependence of the *AMR*. For the low gate voltages $V_g \leq 12.5$ V and magnetic fields $B_{ip} \leq 5$ T and for $V_g = 5\,\mathrm{V}/B_{ip} = 14$ T, both microbridges show qualitatively the same ϕ dependence with maxima always at the same ϕ-position, indicating a crystalline anisotropy of the *AMR*.

At high gate voltages $V_g = 24.91$ V and for $B_{ip} = 5$ T the sign of the oscillations of both bridges is shifted in comparison to Figure 3.27, while the absolute amplitude is comparable. If the magnetic field is increased to 14 T, for bridge A the shape of oscillations suggests a higher order contribution, while *AMR* for E the two-fold oscillation drastically increases.

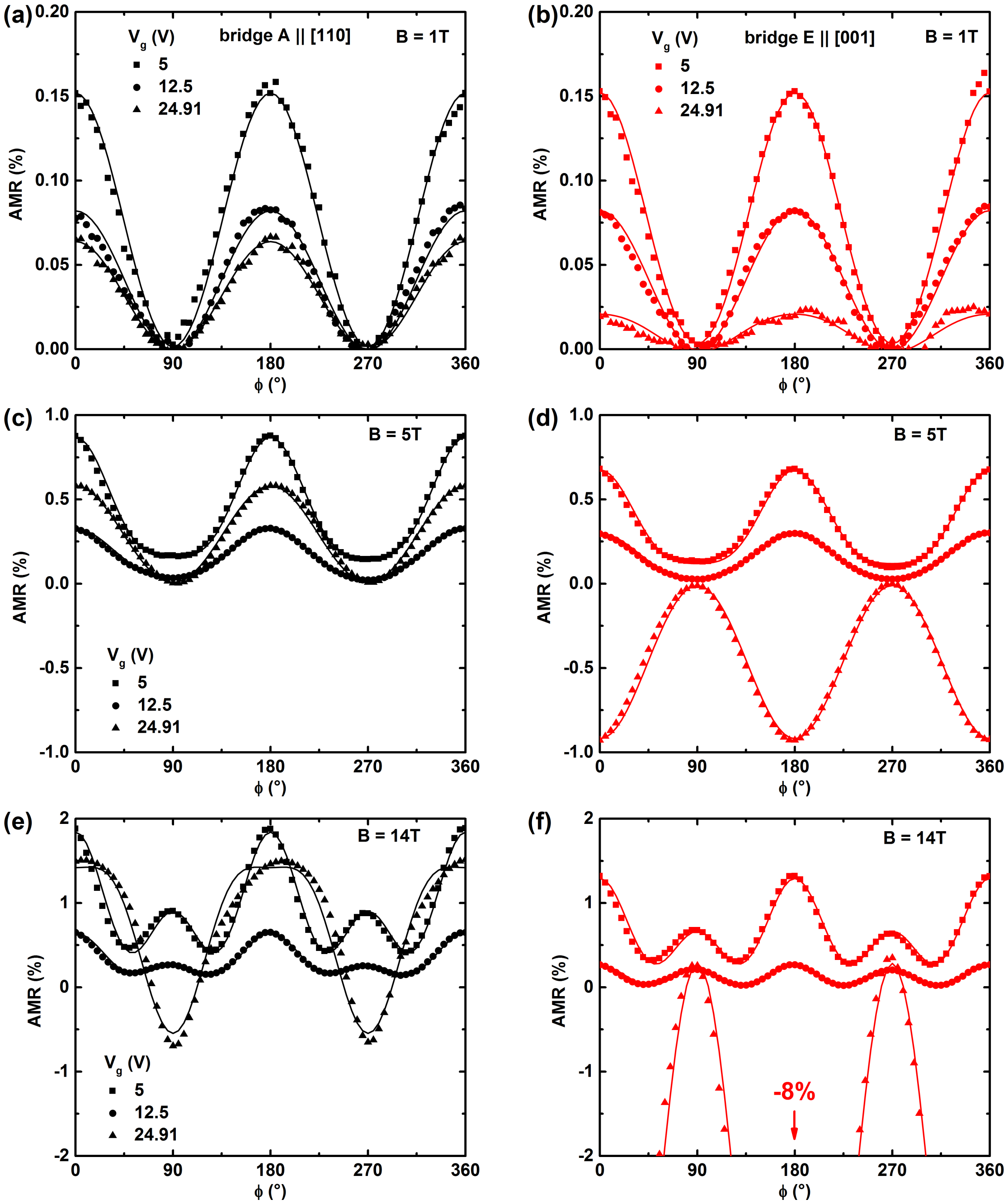

Figure 3.29.: *AMR* versus ϕ, the angle between B_{ip} and the [001]-direction for bridge A and E for various gate-voltages and magnetic fields. Symbols show experimental data for different gate voltages V_g, the solid lines are fits according to ??. All measurements were done at $T = 2\,\mathrm{K}$. (a) and (b) for $B_{ip} = 1\,\mathrm{T}$, (c) and (d) for $B_{ip} = 5\,\mathrm{T}$ and (e) and (f) for $B_{ip} = 14\,\mathrm{T}$.

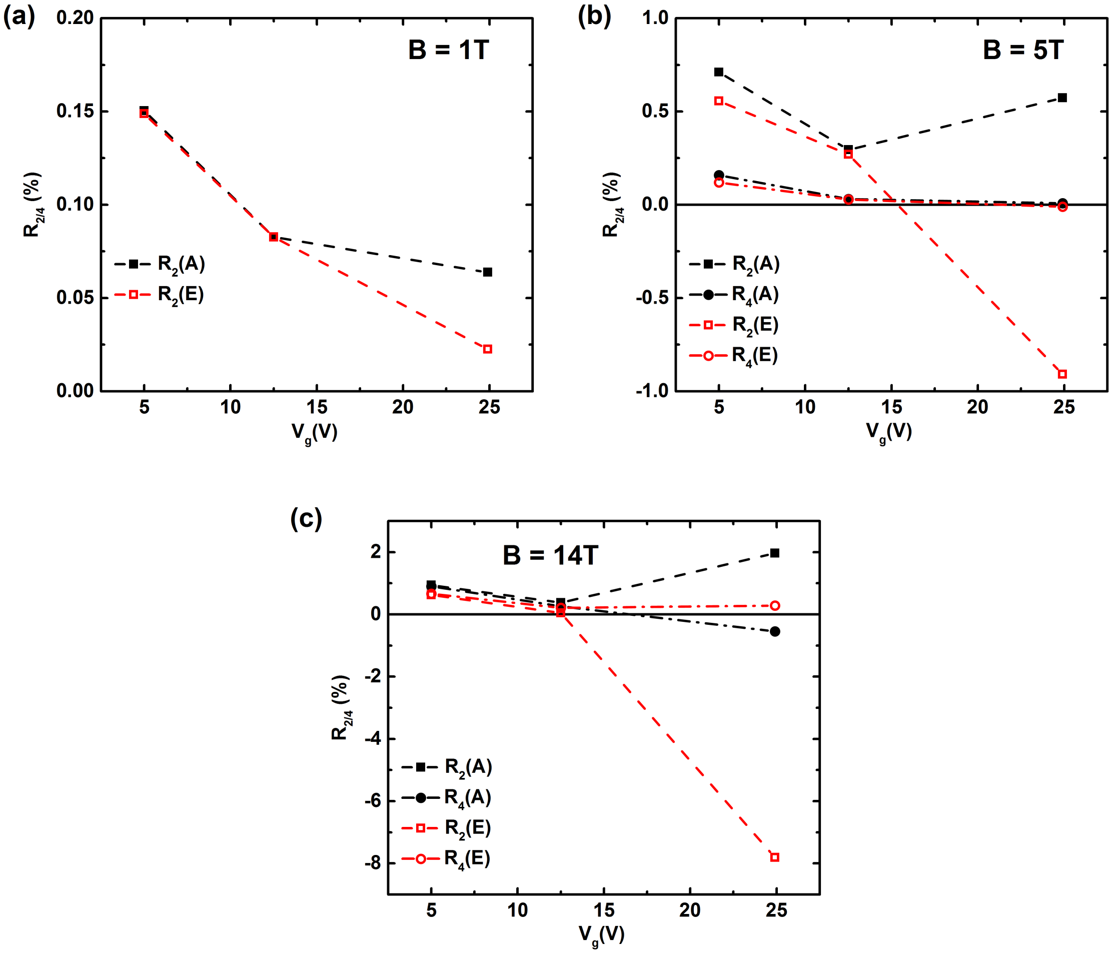

Figure 3.30.: Relative amplitudes R_2 and R_4 of bridge A and E obtained from fits of **??** to the experimental data of the backgating experiments shown in Figure 3.29 for $B = 1\,\mathrm{T}$ (a), $5\,\mathrm{T}$ (b) and $14\,\mathrm{T}$ (c).

Figure 3.30 shows the amplitudes R_2 and R_4 obtained from fits of **??** to the experimental data of the backgating experiments shown in Figure 3.29. For $B = 1\,\mathrm{T}$, there are no four-fold contributions. R_2 and R_4 decrease for all magnetic fields when the gate voltage is increased from 5 V to 12.5 V. For $V_g = 24.91\,\mathrm{V}$ and $B \geq 5\,\mathrm{T}$, the amplitude R_2 of the two-fold oscillations becomes negative for bridge E, but increases for A. For 14 T, the four-fold oscillation become relevant, with a negative amplitude R_4 for A and a small positive R_4 for E.

As expected from the previous simulations, beside a two-fold *AMR* including sign changes also a four-fold contribution to the *AMR* appears when the doping level or the magnetic field are changed, demonstrating that the *AMR* behavior in (110) AO/STO is very sensitive to n_s and B_{ip}. The results explain why (110) LAO/STO or (110) AO/STO sometimes display crystalline or non-crystalline *AMR*. The large sensitivity of the *AMR* to n_s allows to tune magnetotransport by electric field effect, which especially might be important for applications in the field of spintronics.

Experiments which combine a backgate and a sidegate electrode may allow to individually control the Rashba-SOC strength α and the charge carrier concentration. Supported by simulations of the electronic band structure, this might be a suitable tool to obtain a better understanding of the Rashba-coupling and its effect on the electronic transport in anisotropic 2DES.

3.3. Anisotropic electronic transport of (111)-oriented AO/STO heterostructures

(111)-oriented AO/STO samples have been prepared by the deposition of Al_2O_3 via PLD on STO as described in section 2.1. The structured microbridges reach from bridge A along $[1\bar{1}0]$ to bridge E along the $[\bar{1}\bar{1}2]$ direction. The substrate miscut of sample B296 results in a terrace structure with a terrace width of approximately 200 nm and a step height of around 2.3 Å ($a/\sqrt{3}$, where $a = 3.905$ Å, see Figure 2.2), where the step edges are aligned by an angle of $\phi \approx 20^\circ$ with respect to bridge E, which is parallel to $[\bar{1}\bar{1}2]$.

Figure 3.31 shows the microstructure where the conducting areas are the bright regions where no residual particles are found, whereas the darker, insulating parts represent the areas with the inhibit CeO layer. The right hand side displays the orientation of the step edges of the clean, terminated STO substrate before the PLD process. The picture was obtained by an AFM in contact mode.

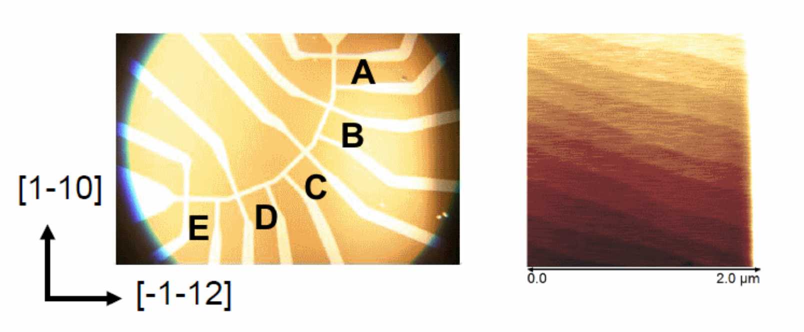

Figure 3.31.: Micrograph of the structured microbridges on sample B296 with (111) surface orientation. The microbridges (bright areas, left) are $16 \times 100\,\mu m^2$ in size. There are no residual particles in the conducting area. The right side shows an AFM micrograph recorded in contact mode. The terraces are oriented by an angle of $\phi \approx 20^\circ$ with respect to the $[\bar{1}\bar{1}2]$ direction.

3.3.1. Temperature dependence

Figure 3.32 shows the temperature dependence for microbridges A-E (corresponding to current direction along the $[1\bar{1}0]$ and $[\bar{1}\bar{1}2]$ direction, respectively) for sample B296. First, R_s decreases with decreasing T, however much slower compared to the decrease of R_s for (001) and (110) AO/STO. At around $T = 90$ K, $R_s(T)$ displays a shallow minimum. Below the minimum, R_s increases continuously with decreasing temperature down to $T = 2$ K. The anisotropy between the microbridges A and E increases with decreasing temperature, from

4 % at 300 K to 12 % at 2 K. Fits according to Equation 3.2 for impurity and electron-phonon interactions in the low and high temperature regime, respectively, are indicated by solid black lines. Impurity scattering becomes dominant for temperatures below the minimum at $T \approx 120\,\mathrm{K}$.

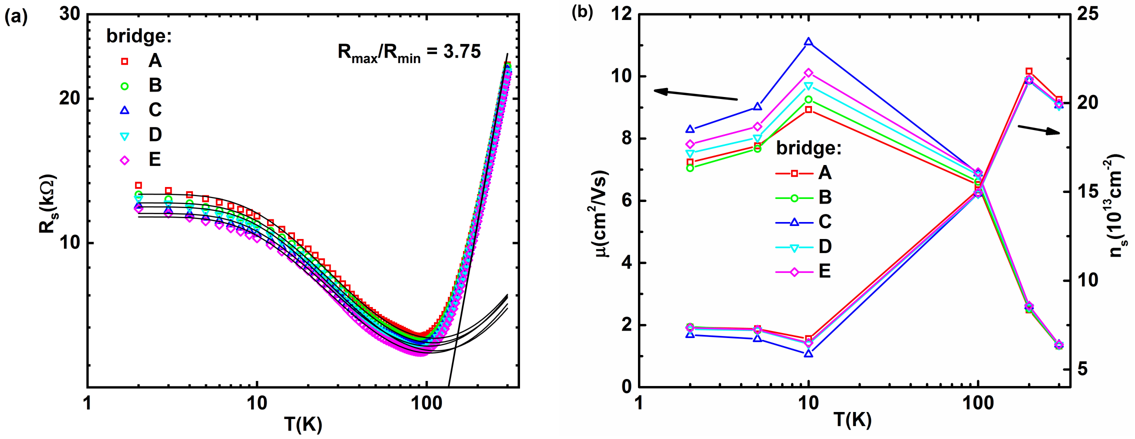

Figure 3.32.: (a) The sheet resistance versus temperature of (111)-oriented AO/STO. The solid black lines show fits for impurity scattering in the low and electron-phonon interactions in the high temperature regime, according to Equation 3.2. (b) The sheet carrier concentration and mobility obtained by measuring the Hall resistance at different temperatures. Significant anisotropy evolves for $T \leq 100\,\mathrm{K}$.

Figure 3.32(b) displays the sheet carrier density and mobility obtained by measuring the Hall resistance at different temperatures. The Hall resistance is linear with respect to the magnetic field, indicating single-ype carrier transport. Bridge C displays the lowest sheet carrier density and highest mobility. The remaining four microbridges show continuous behavior, with increasing mobility from bridge A to bridge E. The sheet carrier density seems to be mostly homogeneous with respect to the various microbridges without indications for a distinct anisotropy.

3.3.2. Magnetic field dependence

The magnetic field dependence of the sheet resistance of (111) AO/STO is quite different-from that of (001) and (110) AO/STO discussed before. Measurements of *MR* are shown in Figure 3.33. Interestingly, in strong contrast to (001) and (110) AO/STO heterostructures the *MR* displays no significant difference for the microbridges A-E. Figure 3.33 (a) shows for example *MR* of bridge A for different temperatures.

The *MR* is linear for $T \geq 100\,\mathrm{K}$ and comparable to that of (001) and (110) AO/STO heterostructures. For lower temperatures and fields above $B = 2\,\mathrm{T}$, *MR* differs strongly from that of (001) and (110) oriented AO/STO. The *MR* increases with decreasing T, from 0.5 % at 10 K to a maximum of 2.3 % at 2 K and $B = 6\,\mathrm{T}$. For magnetic fields larger than 6 T, the *MR* decreases with increasing field strength resulting in a negative *MR* of up to −0.54 % at 14 T.

At small magnetic fields $B \leq 2\,\mathrm{T}$ for $T = 2\,\mathrm{K}$ the data shows the typical B dependence of WAL. Fits to the sheet resistance with respect to the Maekawa-Fukuyama model (Equation 3.6) are shown in Figure 3.33(b) by solid lines. Although the WAL description of MF only holds for small magnetic fields in the diffusive limit of transport, the inclusion of Zeeman corrections still gives good fits to the data in the high-field range ($B > 2\,\mathrm{T}$). The characteristic fields obtained from the fits are well comparable to (001) and (110) AO/STO, i.e., ($B_i \approx 200\,\mathrm{mT}, B_{so} \approx 1.5\,\mathrm{T}$). Therefore, one might expect similar Rashba-type SOC in (111) AO/STO as well. Even at $T = 2\,\mathrm{K}$, anisotropic behavior of *MR* is not significant.

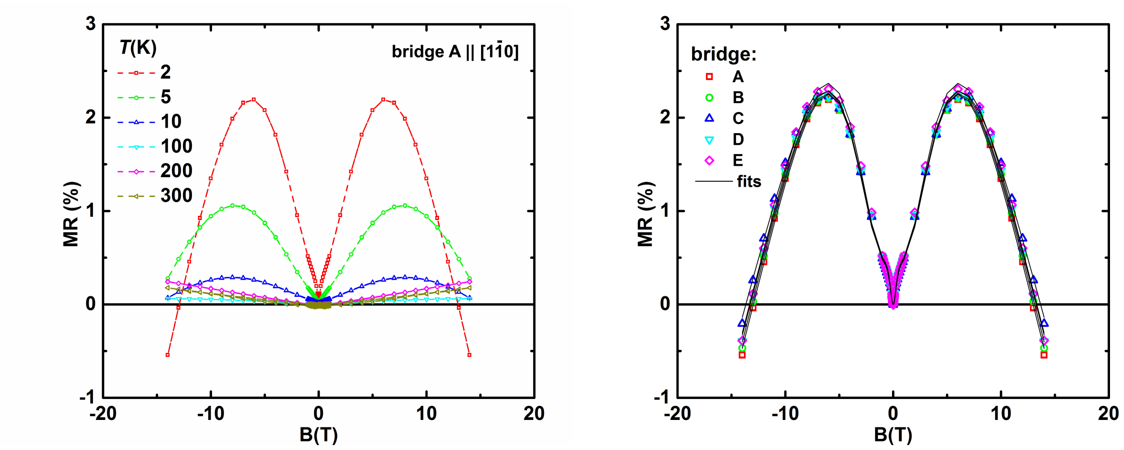

Figure 3.33.: Magnetoresistance of (111) AO/STO. (a) *MR* for microbridge A for different temperatures. (b) *MR* for the microbridges at $T = 2\,\mathrm{K}$. Fits to the MF expression are shown by solid lines. For $B \geq 5\,\mathrm{T}$ Zeeman corrections dominate the magnetotransport and even lead to a negative *MR*.

Figure 3.34 shows the magnetoresistance at $T = 2\,\mathrm{K}$ plotted for the different microbridges for various magnetic fields. For $B = 0.5\,\mathrm{T}$ and 1 T, where WAL dominates magnetotransport, *MR* shows isotropic behavior. For $B \leq 6\,\mathrm{T}$ *MR* steadily increases with increasing field, showing an isotropic positive *MR*. However, at large fields, $B = 14\,\mathrm{T}$, *MR* is negative and smallest for bridge C. Interestingly, the anisotropic behavior at $B = 14\,\mathrm{T}$ seems to be nearly symmetric with respect to C. One may probably note a small increase of *MR* from bridge A to E for $B \geq 6\,\mathrm{T}$ (ignoring bridge C for $B = 14\,\mathrm{T}$), which might be attributed to changes in the Hall mobility.

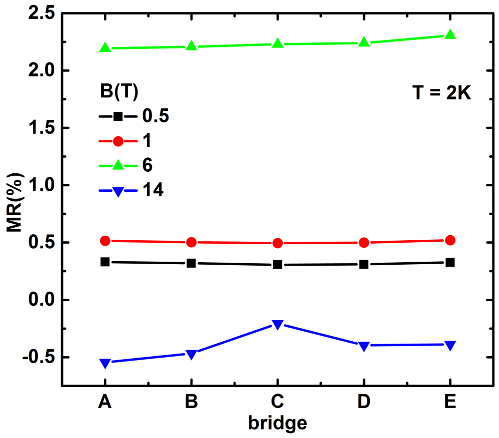

Figure 3.34.: Magnetoresistance of (111) AO/STO for different magnetic fields. Note, for $B = 14\,\mathrm{T}$ *MR* is negative.

3.3.3. Magnetotransport for in-plane magnetic fields

For (111) AO/STO, the *AMR* has been measured for $T = 2\,\mathrm{K}$ and different magnetic field strengths. The same measurement procedure and parameters as described in subsection 3.1.3 were used. Figure 3.35 shows the amplitude of the in-plane magnetoresistance ΔR_{xx} at $T = 2\,\mathrm{K}$ and $B = 14\,\mathrm{T}$ versus θ, the angle between the in-plane magnetic field and current (bridge) direction. ΔR_{xx} can be perfectly described by a two-fold oscillation, with an additional four-fold oscillation of which the amplitude decreases from bridge A to E. ΔR_{xy} follows a simple two-fold pattern.

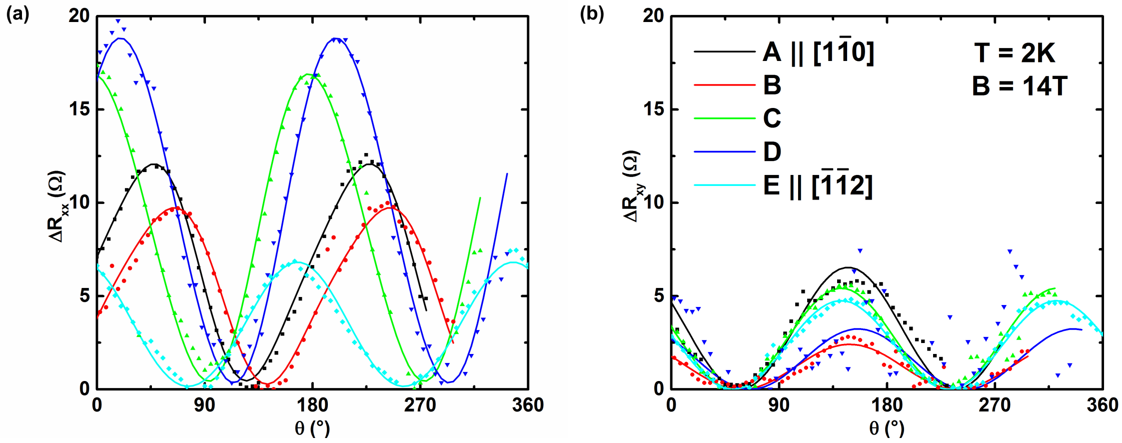

Figure 3.35.: Amplitude of the magnetoresistance for an in-plane magnetic field of 14 T at $T = 2\,\mathrm{K}$. (a) R_{xx} plotted against θ, the angle between the magnetic field and the current direction. (b) R_{xy} versus θ. Solid lines are fits to the experimental data with respect to Equation 3.8.

As expected, ΔR_{xy} shows maxima at θ around 45°. Fits to the measured data were performed as described in Figure 2.9 and are shown in the figure by solid lines.

As mentioned above, the *MR* and *AMR* behavior of (111) AO/STO are quite different to those from (001) and (110) AO/STO. Reasons for that are at the present not clear and have to be figured out in more detail by systematic theoretical support via for example LCAO calculations as already carried out for (110) AO/STO. Beside the crystalline anisotropy of (111) AO/STO, which may result in an intrinsic anisotropic electronic transport as found for (110) AO/STO, extrinsic inhomogeneities, as observed for (001) AO/STO have to be taken into account, which may influence the anisotropic behavior. In combination, that might probably result in a rather complicated electronic transport, with contributions hard to disentangle from intrinsic electronic anisotropy.

4. Conclusion

In this work, AO/STO heterostructures with (001), (110) and (111) STO substrate surface orientation were prepared by pulsed laser deposition and their electronic transport was investigated in detail, especially with respect to anisotropy. Resistance bridges and Hall bars were patterned by photolithography along different crystallographic directions before depositing Al_2O_3 using an in-house developed hard-mask lift-off technique. Electrical contacts to the buried interface were prepared by ultrasonic wire bonding. During the transport measurements and further sample characterization the AO/STO heterostructures showed no degradation with respect to the investigated properties, indicating good chemical stability and passivity to the ambient conditions.

Generally, the AO/STO heterostructures display electron-like metallic transport, i.e., decreasing resistance with decreasing T, down to $T \approx 30\,\mathrm{K}$. Below the minimum, R_s increases slightly again and displays weak antilocalization below about 10 K. The sheet resistance at room temperature usually is of the order of $10^3\ \Omega$, which indicates that these correlated 2DES are close to a metal-insulator transition. Sheet carrier concentration and Hall mobility are decreasing and increasing with decreasing temperature, respectively. At room temperature, n_s amounts to about $4 \times 10^{13}\,\mathrm{cm}^{-2}$ and is rather independent of the substrate orientation and well comparable to that of LAO/STO heterostructures. The mobility reaches up to $400\,\mathrm{cm}^2/\mathrm{Vs}$ at 2 K for (001) and (110) AO/STO and seems to be significantly reduced for (111) AO/STO.

For the (001) AO/STO heterostructures, anisotropic electronic transport develops below the minimum in $R_s(T)$ at $T \approx 30\,\mathrm{K}$, where impurity scattering becomes dominant compared to electron-phonon interactions at higher temperatures.

The anisotropy is most likely caused by an anisotropic distribution of dislocation lines along the [110] and $[1\bar{1}0]$ crystallographic directions and scattering deliberately induced by a substrate miscut angle, i.e., misalignment of the surface normal with respect to the crystallographic (001) direction. Typically, the miscut angle amounts to 0.1–0.2°, resulting in a terrace width of about 100–200 nm. AO/STO heterostructures grown on standard (001) STO substrates display resistance anisotropy of up to about 50 % dominated by anisotropic bulk-like defect scattering due to an inhomogeneous distribution of dislocation lines. Anisotropic transport caused by step edges is limited to about 10 % for a standard miscut of about 0.2°. However, increasing the number of step edges by a factor of 5 by increasing the miscut angle to about 0.5° results in a dominant contribution to the anisotropic transport by step-edge scattering. The contribution of the step edges to the anisotropic transport increases systematically with decreasing terrace width. This gives the possibility to directly manipulate the electronic anisotropy of the 2DES and might even result in a quasi one-dimensional system when the terrace is smaller than the mean free path of the conducting electrons.

Magnetoresistance (MR) is dominated by classical Lorentz scattering for $T \geq 10\,\mathrm{K}$. For $T < 10\,\mathrm{K}$, weak antilocalization (WAL) emerges and dominates the electronic transport for $B \leq 5\,\mathrm{T}$. Fits to the experimental data according to the Maekawa-Fukuyama model [87] give the fitting parameters $B_i \approx 0.1$–$0.3\,\mathrm{T}$ (inelastic field) and $B_{so} \approx 0.3$–$5\,\mathrm{T}$ (spin-orbit field) which are comparable to those of LAO/STO ($B_i \approx 0.1\,\mathrm{T}, B_{so} \approx 1$–$5\,\mathrm{T}$) [80], which strongly suggests that the responsible spin-orbit coupling mechanism is Rashba-type alike in AO/STO. The anisotropic contributions to B_{so} are proportional to the inverse of the Hall mobility of the corresponding microbridge, which suggests that the anisotropy of the WAL is caused by impurity-driven Elliot-Yafet spin relaxation [100, 101].

Measurements of the anomalous magnetoresistance (*AMR*) for the magnetic field direction parallel to the interface show two-fold angular oscillations. The angular position of the extrema depends only on the relative angle between magnetic field and current direction and are independent of the crystallographic orientation of the current. The maxima of the *AMR* occur for the magnetic field applied parallel to the current direction. The amplitude of the *AMR* increases quadratically with increasing magnetic field strength, indicating Rashba-type SOC, which however appears to be somewhat smaller for AO/STO than for LAO/STO.

In contrast to (001) AO/STO, measurements on (110) AO/STO display anisotropic electronic transport over the complete measured temperature range. In addition, anisotropy decreases with decreasing T and becomes less relevant in the temperature regime where usually defect scattering limits electronic transport. That behavior strongly suggests that anisotropic behavior in (110) AO/STO is dominated by intrinsic electronic anisotropy and not by extrinsic effects as it is the case in AO/STO. The Hall mobility is lowest for the current parallel to the $[1\bar{1}0]$ direction and highest for [001], while the charge carrier concentration is isotropic.

Similar to (001) AO/STO, the *MR* for $T \geq 10\,\mathrm{K}$ is dominated by Lorentz scattering, and for $T < 10\,\mathrm{K}$ WAL becomes significant. WAL for $T \leq 10\,\mathrm{K}$ and $B \leq 3\,\mathrm{T}$ shows no significant anisotropy and results in B_i and B_{so} of about 0.2 T and 0.55 T, respectively, comparable to LAO/STO, where Rashba-type SOC is reported. *AMR* measurements at 2 K for the magnetic field direction in the conduction plane show again two-fold angular oscillations. Their amplitude is proportional to the square of the magnetic field strength and thus Rashba-SOC is indicated as well. At high magnetic fields, negative in-plane *MR* due to Zeeman spin-splitting is found.

Band structure calculations by linear combination of atomic orbitals including Rashba-SOC, confirm the influence of the band structure on the anisotropic transport. The experimental results for the AMR can be modeled successfully if different electronic lifetimes for different electronic subbands are assumed.

Backgating experiments show that the *AMR* is strongly influenced by the gate voltage applied normal to the interface. With decreasing gate voltage, i.e., increasing resistance, the *AMR* displays four-fold oscillations instead of the previously observed two-fold oscillations. In addition, with increasing magnetic field, maxima of the AMR can also shift by about 90°. These observations demonstrate the strong effect of sheet carrier concentration and magnetic field on the *AMR* behavior and very likely explain the different *AMR* reported in literature.

The (111) AO/STO heterostructures show a metallic interface as well, but R_s is increased by a factor of 10 compared to (001) and (110) heterostructures. The minimum of $R_s(T)$ is found at 90 K. Anisotropy increases with decreasing temperature, with $R_s(2\,\mathrm{K})$ being lowest along $[1\bar{1}0]$ and largest along the $[\bar{1}\bar{1}2]$ direction.

MR shows no significant anisotropy. For $B \geq 10$ T, *MR* becomes negative, most likely due to the Zeeman effect. In (111) AO/STO, WAL is comparable to WAL in (001) and (110) AO/STO. The Maekawa-Fukuyama model including Zeeman corrections gives a perfect description of the data up to the highest magnetic fields.

AMR experiments on (111) AO/STO show two-fold oscillations, which show no clear angular dependence of their maxima with respect to the angle between the current and the magnetic field or crystallographic directions. This indicates a rather complicated electronic transport and might be of interest for future research. The detailed interpretations of different crystallographic orientations of AO/STO interfaces is expected to clarify the role of bulk STO properties in the two-dimensional interfaces.

Future experiments should expand the gating effects for the different interface orientations and might combine a backgate and sidegate electrode, allowing an individual control of the Rashba-SOC strength and the charge carrier concentration. The results may provide further insight on the electronic transport.

List of Figures

List of Tables

Bibliography

[1]J. A. Bert, K. C. Nowack, B. Kalisky, H. Noad, J. R. Kirtley, C. Bell, H. K. Sato, M. Hosoda, Y. Hikita, H. Y. Hwang, and K. A. Moler, "Gate-tuned superfluid density at the superconducting $LaAlO_3/SrTiO_3$ interface", Physical Review B - Condensed Matter and Materials Physics **86**, 1–5 (2012).

[2]L. Li, C. Richter, J. Mannhart, and R. C. Ashoori, "Coexistence of magnetic order and two-dimensional superconductivity at $LaAlO_3/SrTiO_3$ interfaces", Nature Physics **7**, 762–766 (2011).

[3]Ariando, X. Wang, G. Baskaran, Z. Q. Liu, J. Huijben, J. B. Yi, A. Annadi, A. R. Barman, A. Rusydi, S. Dhar, Y. P. Feng, J. Ding, H. Hilgenkamp, and T. Venkatesan, "Electronic phase separation at the $LaAlO_3/SrTiO_3$ interface.", Nature communications **2**, 188 (2011).

[4]B. Kalisky, E. M. Spanton, H. Noad, J. R. Kirtley, K. C. Nowack, C. Bell, H. K. Sato, M. Hosoda, Y. Xie, Y. Hikita, C. Woltmann, G. Pfanzelt, R. Jany, C. Richter, H. Y. Hwang, J. Mannhart, and K. a. Moler, "Locally enhanced conductivity due to the tetragonal domain structure in $LaAlO_3/SrTiO_3$ heterointerfaces", Nature Materials **12**, 1–5 (2013).

[5]M. Honig, J. A. Sulpizio, J. Drori, A. Joshua, E. Zeldov, and S. Ilani, "Local electrostatic imaging of striped domain order in $LaAlO_3/SrTiO_3$", Nature Materials **12**, 1112–1118 (2013).

[6]N. C. Bristowe, T. Fix, M. G. Blamire, P. B. Littlewood, and E. Artacho, "Proposal of a One-Dimensional Electron Gas in the Steps at the $LaAlO_3/SrTiO_3$ Interface", Physical Review Letters **108**, 166802 (2012).

[7]S. Caprara, F. Peronaci, and M. Grilli, "Intrinsic Instability of Electronic Interfaces with Strong Rashba Coupling", Physical Review Letters **109**, 196401 (2012).

[8]A. Ohtomo and H. Y. Hwang, "A high-mobility electron gas at the $LaAlO_3/SrTiO_3$ heterointerface", Nature **427**, 423–426 (2004).

[9]S. Thiel, G. Hammerl, A. Schmehl, C. W. Schneider, and J. Mannhart, "Tunable quasi-two-dimensional electron gases in oxide heterostructures", Science **313**, 1942–1945 (2006).

[10] A. Brinkman, M. Huijben, M. Van Zalk, J. Huijben, U. Zeitler, J. C. Maan, W. G. Van Der Wiel, G. Rijnders, D. H. Blank, and H. Hilgenkamp, "Magnetic effects at the interface between non-magnetic oxides", Nature Materials **6**, 493–496 (2007).

[11] N. Reyren, S. Thiel, A. D. Caviglia, L. Fitting Kourkoutis, G. Hammerl, C. Richter, C. W. Schneider, T. Kopp, A. S. Rüetschi, D. Jaccard, M. Gabay, D. A. Muller, J. M. Triscone, and J. Mannhart, "Superconducting interfaces between insulating oxides", Science **317**, 1196–1199 (2007).

[12] J. A. Bert, B. Kalisky, C. Bell, M. Kim, Y. Hikita, H. Y. Hwang, and K. A. Moler, "Direct imaging of the coexistence of ferromagnetism and superconductivity at the $LaAlO_3/SrTiO_3$ interface", Nature Physics **7**, 767–771 (2011).

[13] L. Fidkowski, H.-C. Jiang, R. M. Lutchyn, and C. Nayak, "Magnetic and superconducting ordering in one-dimensional nanostructures at the $LaAlO_3/SrTiO_3$ interface", Phys. Rev. B **87**, 014436 (2013).

[14] M. S. Scheurer and J. Schmalian, "Topological superconductivity and unconventional pairing in oxide interfaces", Nature Communications **6** (2015) `10.1038/ncomms7005`.

[15] F. Loder, A. P. Kampf, and T. Kopp, "Route to Topological Superconductivity via Magnetic Field Rotation", Scientific Reports **5**, 1–10 (2015).

[16] M. Ben Shalom, C. W. Tai, Y. Lereah, M. Sachs, E. Levy, D. Rakhmilevitch, A. Palevski, and Y. Dagan, "Anisotropic magnetotransport at the $SrTiO_3/LaAlO_3$ interface", Physical Review B - Condensed Matter and Materials Physics **80**, 3–6 (2009).

[17] G. Herranz, F. Sánchez, N. Dix, M. Scigaj, and J. Fontcuberta, "High mobility conduction at (110) and (111) $LaAlO_3/SrTiO_3$interfaces", Scientific Reports **2**, 3–7 (2012).

[18] K. Gopinadhan, A. Annadi, Y. Kim, A. Srivastava, B. Kumar, J. Chen, J. M. D. Coey, Ariando, and T. Venkatesan, "Gate Tunable In- and Out-of-Plane Spin–Orbit Coupling and Spin-Splitting Anisotropy at $LaAlO_3/SrTiO_3$ (110) Interface", Advanced Electronic Materials **1**, 1500114, 1500114–n/a (2015).

[19] S.-C. Shen, Y.-P. Hong, C.-J. Li, H.-X. Xue, X.-X. Wang, and J.-C. Nie, "In-plane anisotropy in two-dimensional electron gas at $LaAlO_3/SrTiO_3$ (110) interface", Chinese Physics B **25**, 076802 (2016).

[20] J. Mannhart and D. G. Schlom, "Oxide interfaces—an opportunity for electronics", Science **327**, 1607–1611 (2010).

[21] B. Förg, C. Richter, and J. Mannhart, "Field-effect devices utilizing $LaAlO_3/SrTiO_3$ interfaces", Applied Physics Letters **100**, 053506 (2012).

[22] W. Siemons, G. Koster, H. Yamamoto, W. A. Harrison, G. Lucovsky, T. H. Geballe, D. H. A. Blank, and M. R. Beasley, “Origin of Charge Density at $LaAlO_3$ on $SrTiO_3$ Heterointerfaces: Possibility of Intrinsic Doping”, Phys. Rev. Lett. **98**, 196802 (2007).

[23] Y. Chen, N. Pryds, J. E. Kleibeuker, G. Koster, J. Sun, E. Stamate, B. Shen, G. Rijnders, and S. Linderoth, “Metallic and insulating interfaces of amorphous $SrTiO_3$-based oxide heterostructures”, Nano Letters **11**, 3774–3778 (2011).

[24] S. W. Lee, Y. Q. Liu, J. Heo, and R. G. Gordon, “Creation and Control of Two-Dimensional Electron Gas Using Al-Based Amorphous Oxides/$SrTiO_3$ Heterostructures Grown by Atomic Layer Deposition”, Nano Lett. **12**, 4775–4783 (2012).

[25] D. Fuchs, R. Schäfer, A. Sleem, R. Schneider, R. Thelen, and H. von Löhneysen, “Two-dimensional superconductivity between $SrTiO_3$ and amorphous Al_2O_3”, Applied Physics Letters **105**, 092602 (2014).

[26] K. Wolff, R. Schäfer, M. Meffert, D. Gerthsen, R. Schneider, and D. Fuchs, “Anisotropic electronic transport of the two-dimensional electron system in Al_2O_3/$SrTiO_3$ heterostructures”, Physical Review B **95**, 245132 (2017).

[27] *$SrTiO_3$ for Research and Development, Datasheet*, http://www.crystec.de/daten/srtio3.pdf, CrysTec Kristalltechnologie GmbH (May 2018).

[28] W. Zhong and D. Vanderbilt, “Effect of quantum fluctuations on structural phase transitions in $SrTiO_3$ and $BaTiO_3$”, Phys. Rev. B **53**, 5047–5050 (1996).

[29] O. N. Tufte and P. W. Chapman, “Electron Mobility in Semiconducting Strontium Titanate”, Physical Review **155**, 796–802 (1967).

[30] T. Sakudo and H. Unoki, “Dielectric properties of $SrTiO_3$ at low temperatures”, Physical Review Letters **26**, 851–853 (1971).

[31] K. A. Muller and H. Burkard, “$SrTiO_3$: an intrinsic quantum paraelectric below 4K”, Phys. Rev. B **19**, 3593 (1979).

[32] H. Uwe and T. Sakudo, “Stress-induced ferroelectricity and soft phonon modes in $SrTiO_3$”, Physical Review B **13**, 271–286 (1976).

[33] J. H. Haeni, P. Irvin, W. Chang, R. Uecker, P. Reiche, Y. L. Li, S. Choudhury, W. Tian, M. E. Hawley, B. Craigo, A. K. Tagantsev, X. Q. Pan, S. K. Streiffer, L. Q. Chen, S. W. Kirchoefer, J. Levy, and D. G. Schlom, “Room-temperature ferroelectricity in strained $SrTiO_3$”, Nature **430**, 758–761 (2004).

[34] K. Van Benthem, C. Elsässer, and R. H. French, “Bulk electronic structure of $SrTiO_3$: Experiment and theory”, Journal of Applied Physics **90**, 6156–6164 (2001).

[35] L. F. Mattheiss, “Energy bands for $KNiF_3$, $SrTiO_3$, $KMoO_3$, and $KTaO_3$”, Physical Review B **6**, 4718–4740 (1972).

[36] L. F. Mattheiss, “Effect of the 110°K Phase Transition on the $SrTiO_3$ Conduction Bands”, Physical Review B **6**, edited by Intergovernmental Panel on Climate Change, 4740–4753 (1972).

[37] D. A. Muller, N. Nakagawa, A. Ohtomo, J. L. Grazul, and H. Y. Hwang, “Atomic-scale imaging of nanoengineered oxygen vacancy profiles in $SrTiO_3$”, Nature **430**, 657–661 (2004).

[38] H. Uwe, T. Sakudo, and H. Yamaguchi, “Interband Electronic Raman Scattering in $SrTiO_3$”, Japanese Journal of Applied Physics **24**, 519 (1985).

[39] Y. Tokura and N. Nagaosa, “Orbital Physics in Transition Metal Oxides”, Science **288**, 462–468 (2000).

[40] P. Delugas, A. Filippetti, V. Fiorentini, D. I. Bilc, D. Fontaine, and P. Ghosez, “Spontaneous 2-Dimensional Carrier Confinement at the n-Type $SrTiO_3/LaAlO_3$ Interface”, Phys. Rev. Lett. **106**, 166807 (2011).

[41] A. Joshua, S. Pecker, J. Ruhman, E. Altman, and S. Ilani, “A universal critical density underlying the physics of electrons at the $LaAlO_3/SrTiO_3$ interface”, Nature Communications **3**, 1129 (2012).

[42] *$LaAlO_3$ for Research and Development, Datasheet*, http://www.crystec.de/daten/laalo3.pdf, CrysTec Kristalltechnologie GmbH (May 2018).

[43] N. Nakagawa, H. Y. Hwang, and D. A. Muller, “Why some interfaces cannot be sharp”, Nature Materials **5**, 204–209 (2006).

[44] Y. Zhang, Y. Gan, W. Niu, K. Norrman, X. Yan, D. V. Christensen, M. von Soosten, H. Zhang, B. Shen, N. Pryds, J. Sun, and Y. Chen, “Tuning the two-dimensional electron gas at oxide interfaces with ti–o configurations: evidence from x-ray photoelectron spectroscopy”, ACS Applied Materials & Interfaces **10**, PMID: 29226677, 1434–1439 (2018).

[45] D. Christensen and A. Smith, “Is γ-Al_2O_3 polar?”, Applied Surface Science **423**, 887–890 (2017).

[46] L. Qiao, T. C. Droubay, V. Shutthanandan, Z. Zhu, P. V. Sushko, and S. A. Chambers, “Thermodynamic instability at the stoichiometric $LaAlO_3$ / $SrTiO_3$ (001) interface”, Journal of Physics: Condensed Matter **22**, 312201 (2010).

[47] M. Breitschaft, V. Tinkl, N. Pavlenko, S. Thiel, C. Richter, J. R. Kirtley, Y. C. Liao, G. Hammerl, V. Eyert, T. Kopp, and J. Mannhart, “Two-dimensional electron liquid state at $LaAlO_3$-$SrTiO_3$ interfaces”, 1–4 (2009).

[48] G. Berner, M. Sing, H. Fujiwara, A. Yasui, Y. Saitoh, A. Yamasaki, Y. Nishitani, A. Sekiyama, N. Pavlenko, T. Kopp, C. Richter, J. Mannhart, S. Suga, and R. Claessen, “Direct k-space mapping of the electronic structure in an oxide-oxide interface”, Physical Review Letters **110**, 1–5 (2013).

[49] R. Pentcheva and W. E. Pickett, “Electronic phenomena at complex oxide interfaces: insights from first principles”, Journal of Physics: Condensed Matter **22**, 043001 (2010).

[50] C. Cancellieri, M. L. Reinle-Schmitt, M. Kobayashi, V. N. Strocov, P. R. Willmott, D. Fontaine, P. Ghosez, A. Filippetti, P. Delugas, and V. Fiorentini, “Doping-dependent band structure of $LaAlO_3/SrTiO_3$ interfaces by soft x-ray polarization-controlled resonant angle-resolved photoemission”, Phys. Rev. B **89**, 121412 (2014).

[51] S. Gariglio, M. Gabay, and J.-M. Triscone, “Research Update : Conductivity and beyond at the $LaAlO_3$ / $SrTiO_3$ interface”, APL Materials **4**, 060701 (2016).

[52] X. Wang, W. M. Lü, A. Annadi, Z. Q. Liu, K. Gopinadhan, S. Dhar, T. Venkatesan, and Ariando, “Magnetoresistance of two-dimensional and three-dimensional electron gas in $LaAlO_3/SrTiO_3$ heterostructures: Influence of magnetic ordering, interface scattering, and dimensionality”, Physical Review B - Condensed Matter and Materials Physics **84**, 3–6 (2011).

[53] M. Kohler, “Zur magnetischen Widerstandsänderung reiner Metalle”, Annalen der Physik **424**, 211–218 (1938).

[54] M. Kohler, “Magnetische Widerstandsänderung und Leitfähigkeitstypen. II”, Annalen der Physik **440**, 99–107 (1949).

[55] R. Gross and A. Marx, *Festkörperphysik*, 2., aktualisierte Aufl., De Gruyter StudiumDe Gruyter eBook-Paket Mathematik und Physik (De Gruyter Oldenbourg, Berlin [u.a.], 2014).

[56] H. Yuan, M. S. Bahramy, K. Morimoto, S. Wu, K. Nomura, B.-J. Yang, H. Shimotani, R. Suzuki, M. Toh, C. Kloc, X. Xu, R. Arita, N. Nagaosa, and Y. Iwasa, “Zeeman-type spin splitting controlled by an electric field”, Nature Physics **9**, 563–569 (2013).

[57] T. Khouri, U. Zeitler, C. Reichl, W. Wegscheider, N. E. Hussey, S. Wiedmann, and J. C. Maan, “Linear Magnetoresistance in a Quasifree Two-Dimensional Electron Gas in an Ultrahigh Mobility GaAs Quantum Well”, Phys. Rev. Lett. **117**, 256601 (2016).

[58] H. G. Johnson, S. P. Bennett, R. Barua, L. H. Lewis, and D. Heiman, “Universal properties of linear magnetoresistance in strongly disordered MnAs-GaAs composite semiconductors”, Phys. Rev. B **82**, 085202 (2010).

[59] A. A. Abrikosov, “Quantum linear magnetoresistance”, EPL (Europhysics Letters) **49**, 789 (2000).

[60] J. Hu and T. F. Rosenbaum, “Classical and quantum routes to linear magnetoresistance”, Nat Mater **7**, 697–700 (2008).

[61] M. M. Parish and P. B. Littlewood, “Non-saturating magnetoresistance in heavily disordered semiconductors”, Nature **426**, 162–165 (2003).

[62] M. M. Parish and P. B. Littlewood, “Classical magnetotransport of inhomogeneous conductors”, Physical Review B - Condensed Matter and Materials Physics **72**, 1–11 (2005).

[63] W. J. Wang, K. H. Gao, Z. Q. Li, T. Lin, J. Li, C. Yu, and Z. H. Feng, “Classical linear magnetoresistance in epitaxial graphene on SiC”, Applied Physics Letters **105**, 182102 (2014).

[64] F. J. Ohkawa and Y. Uemura, “Quantized Surface States of a Narrow-Gap Semiconductor”, Journal of the Physical Society of Japan **37**, 1325–1333 (1974).

[65] Y. A. Bychkov and É. I. Rashba, “Properties of a 2D electron gas with lifted spectral degeneracy”, Soviet Journal of Experimental and Theoretical Physics Letters **39**, 78 (1984).

[66] Y. A. Bychkov and E. I. Rashba, “Oscillatory effects and the magnetic susceptibility of carriers in inversion layers”, Journal of Physics C: Solid State Physics **17**, 6039 (1984).

[67] R. Winkler, *Spin-orbit coupling effects in two-dimensional electron and hole systems : with 26 tables*, Springer tracts in modern physics ; 191 (Springer, Berlin, 2003).

[68] J. J. Sakurai, *Advanced quantum mechanics*, 18. print. (Addison-Wesley, Reading, Mass. [u.a.], 1994).

[69] G. Dresselhaus, “Spin-Orbit Coupling Effects in Zinc Blende Structures”, Phys. Rev. **100**, 580–586 (1955).

[70] U. Rössler and J. Kainz, “Microscopic interface asymmetry and spin-splitting of electron subbands in semiconductor quantum structures”, Solid State Communications **121**, 313–316 (2002).

[71] P. von Allmen, “Derivation of the effective-mass equation for a superlattice: A perturbational approach”, Physical Review B **46**, 15377–15381 (1992).

[72] A. D. Caviglia, M. Gabay, S. Gariglio, N. Reyren, C. Cancellieri, and J. M. Triscone, "Tunable Rashba Spin-Orbit Interaction at Oxide Interfaces", Physical Review Letters **104**, 126803 (2010).

[73] L. E. Golub, N. S. Averkiev, and M. Willander, "Electron spin relaxation in zinc-blende heterostructures", Nanotechnology **11**, 215–217 (2000).

[74] L. Petersen and P. Hedegård, "A simple tight-binding model of spin–orbit splitting of sp-derived surface states", Surface Science **459**, 49–56 (2000).

[75] K. V. Shanavas and S. Satpathy, "Electric Field Tuning of the Rashba Effect in the Polar Perovskite Structures", Physical Review Letters **112**, 086802 (2014).

[76] Z. S. Popovi ć, S. Satpathy, and R. M. Martin, "Origin of the Two-Dimensional Electron Gas Carrier Density at the $LaAlO_3$ on $SrTiO_3$ Interface", Phys. Rev. Lett. **101**, 256801 (2008).

[77] M. Hirayama and M. Imada, "Systematic Control of Doped Carrier Density without Disorder at Interface of Oxide Heterostructures", Journal of the Physical Society of Japan **79**, 034704 (2010).

[78] A. Bournel, P. Dollfus, S. Galdin, F.-X. Musalem, and P. Hesto, "Modelling of gate-induced spin precession in a striped channel high electron mobility transistor", Solid state communications **104**, 85–89 (1997).

[79] R. Raimondi, M. Leadbeater, P. Schwab, E. Caroti, and C. Castellani, "Spin-orbit induced anisotropy in the magnetoconductance of two-dimensional metals", Physical Review B **64**, 235110 (2001).

[80] A. Fête, S. Gariglio, A. D. Caviglia, J. M. Triscone, and M. Gabay, "Rashba induced magnetoconductance oscillations in the $LaAlO_3$-$SrTiO_3$ heterostructure", Physical Review B - Condensed Matter and Materials Physics **86**, 201105 (2012).

[81] M. Diez, A. Monteiro, G. Mattoni, E. Cobanera, T. Hyart, E. Mulazimoglu, N. Bovenzi, C. W. J. Beenakker, and a. D. Caviglia, "Giant Negative Magnetoresistance Driven by Spin-Orbit Coupling at the $LaAlO_3/SrTiO_3$ Interface", Physical Review Letters **115**, 016803 (2015).

[82] S. Das, Z. Hossain, and R. C. Budhani, "Signature of enhanced spin-orbit interaction in the magnetoresistance of $LaTiO_3/SrTiO_3$ interfaces on δ doping", Phys. Rev. B **94**, 115165 (2016).

[83] A. I. Larkin and D. E. Khmel'nitskiĭ, "Anderson localization and anomalous magnetoresistance at low temperatures", Soviet Physics Uspekhi **25**, 185–187 (1982).

[84] G. Bergmann, "Weak localization in thin films", Physics Reports **107**, 1–58 (1984).

[85] B. Altshuler, A. Aronov, and D. Khmelnitsky, "Suppression of localization effects by the high frequency field and the Nyquist noise", Solid State Communications **39**, 619–623 (1981).

[86] S. Hikami, A. I. Larkin, and Y. Nagaoka, "Spin-Orbit Interaction and Magnetoresistance in the Two Dimensional Random System", Progress of Theoretical Physics **63**, 707–710 (1980).

[87] S. Maekawa and H. Fukuyama, "Magnetoresistance in two-dimensional disordered systems: Effects of Zeeman splitting and spin-orbit scattering", Journal of the Physical Society of Japan **50**, 2516–2524 (1981).

[88] B. L. Altshuler, A. G. Aronov, and D. E. Khmelnitsky, "Effects of electron-electron collisions with small energy transfers on quantum localisation", Journal of Physics C: Solid State Physics **15**, 7367–7386 (1982).

[89] R. Schäfer, *Quantendiffusionskorrekturen zum Leitwert einer ballistischen Verengung in einer mesoskopischen Goldstruktur*, ger, Köln, 1993.

[90] A. Punnoose, "Magnetoconductivity in the presence of Bychkov-Rashba spin-orbit interaction", Applied Physics Letters **88**, 1–4 (2006).

[91] Y. Aharonov and D. Bohm, "Significance of Electromagnetic Potentials in the Quantum Theory", Phys. Rev. **115**, 485–491 (1959).

[92] Y. Imry and R. A. Webb, "Quantum Interference and the Aharonov-Bohm Effect", Scientific American **260**, 56–65 (1989).

[93] G. Salis, Y. Kato, K. Ensslin, D. C. Driscoll, A. C. Gossard, and D. D. Awschalom, "Electrical control of spin coherence in semiconductor nanostructures", Nature **414**, 619 (2001).

[94] E. Ivchenko, A. Kiselev, and M. Willander, "Electronic g factor in biased quantum wells", Solid State Communications **102**, 375–378 (1997).

[95] T. P. Pareek and P. Bruno, "Spin coherence in a two-dimensional electron gas with Rashba spin-orbit interaction", Phys. Rev. B **65**, 241305 (2002).

[96] F. E. Meijer, A. F. Morpurgo, T. M. Klapwijk, T. Koga, and J. Nitta, "Competition between spin-orbit interaction and Zeeman coupling in Rashba two-dimensional electron gases", Phys. Rev. B **70**, 201307 (2004).

[97] Takasuna, Shoichi and Shiogai, Junichi and Matsuzaka, Shunichiro and Kohda, Makoto and Oyama, Yutaka and Nitta, Junsaku, “Weak antilocalization induced by rashba spin-orbit interaction in layered iii-vi compound semiconductor gase thin films”, Phys. Rev. B **96**, 161303 (2017).

[98] G. L. Bir, A. G. Aronov, and G. E. Pikus, “Spin relaxation of electrons due to scattering by holes”, Zh. Eksp. Teor. Fiz **69**, 13821397 (1975).

[99] M. I. D’yakonov and V. I. Perel’, “Spin relaxation of conduction electrons in noncentrosymmetric semiconductors”, Sov. Phys. Solid State **13**, 3023–3026 (1972).

[100] R. J. Elliott, “Theory of the effect of spin-Orbit coupling on magnetic resonance in some semiconductors”, Physical Review **96**, 266–279 (1954).

[101] Y. Yafet, “g Factors and Spin-Lattice Relaxation of Conduction Electrons”, Solid State Physics **14**, 1–98 (1963).

[102] I. Žutić, J. Fabian, and S. Das Sarma, “Spintronics: Fundamentals and applications”, Rev. Mod. Phys. **76**, 323–410 (2004).

[103] J.-N. Chazalviel, “Spin-dependent hall effect in semiconductors”, Phys. Rev. B **11**, 3918–3934 (1975).

[104] P. Boguslawski, “Electron-electron spin-flip scattering and spin relaxation in III–V and II–VI semiconductors”, Solid State Communications **33**, 389–391 (1980).

[105] G. PIKUS and A. TITKOV, “CHAPTER 3 - Spin Relaxation under Optical Orientation in Semiconductors”, in *Optical orientation*, Vol. 8, edited by F. MEIER and B. ZAKHARCHENYA, Modern Problems in Condensed Matter Sciences (Elsevier, 1984), pp. 73–131.

[106] J. Fabian and S. D. Sarma, “Spin relaxation of conduction electrons”, Journal of Vacuum Science & Technology B: Microelectronics and Nanometer Structures Processing, Measurement, and Phenomena **17**, 1708–1715 (1999).

[107] G. Koster, B. L. Kropman, G. J. H. M. Rijnders, D. H. a. Blank, and H. Rogalla, “Quasi-ideal strontium titanate crystal surfaces through formation of strontium hydroxide”, Applied Physics Letters **73**, 2920–2922 (1998).

[108] K. J. E., K. Gertjan, S. Wolter, D. David, K. Bouwe, B. J. L., Y. Chan-Ho, R. Jayakanth, R. Ramamoorthy, ten Elshof Johan E., B. D. H. A., and R. Guus, “Atomically Defined Rare-Earth Scandate Crystal Surfaces”, Advanced Functional Materials **20**, 3490–3496 (2010).

[109]D. Fuchs, K. Wolff, R. Schäfer, R. Thelen, M. Le Tacon, and R. Schneider, "Patterning of two-dimensional electron systems in $SrTiO_3$ based heterostructures using a CeO_2 template", AIP Advances **7**, 056410 (2017).

[110]F. Trier, G. E. D. K. Prawiroatmodjo, M. von Soosten, D. V. Christensen, T. S. Jespersen, Y. Z. Chen, and N. Pryds, "Patterning of high mobility electron gases at complex oxide interfaces", Applied Physics Letters **107**, 191604 (2015).

[111]G. E. Prawiroatmodjo, F. Trier, D. V. Christensen, Y. Chen, N. Pryds, and T. S. Jespersen, "Evidence of weak superconductivity at the room-temperature grown $LaAlO_3/SrTiO_3$ interface", Physical Review B **93**, 2–6 (2016).

[112]E. O. Filatova, A. S. Konashuk, F. Schaefers, and V. V. Afanas'ev, "Metallization-Induced Oxygen Deficiency of y-Al_2O_3 Layers", The Journal of Physical Chemistry C **120**, 8979–8985 (2016).

[113]M. Huijben, G. Rijnders, D. H. Blank, S. Bals, S. V. Aert, J. Verbeeck, G. V. Tendeloo, A. Brinkman, and H. Hilgenkamp, "Electronically coupled complementary interfaces between perovskite band insulators", Nature Materials **5**, 556–560 (2006).

[114]Y. Lei, Y. Li, Y. Z. S. Chen, Y. W. Xie, Y. Z. S. Chen, S. H. Wang, J. Wang, B. G. Shen, N. Pryds, H. Y. Hwang, and J. R. Sun, "Visible-light-enhanced gating effect at the $LaAlO_3/SrTiO_3$ interface", Nature Communications **5**, 5554 (2014).

[115]Y. Li, Y. Lei, B. G. Shen, and J. R. Sun, "Visible-light-Accelerated oxygen vacancy migration in strontium titanate", Scientific Reports **5**, 1–7 (2015).

[116]K. Kormondy, A. Posadas, T. Ngo, S. Lu, N. Goble, J. Jordan-Sweet, X. Gao, D. Smith, M. McCartney, J. Ekerdt, and A. Demkov, "Quasi-two-dimensional electron gas at the epitaxial alumina/$SrTiO_3$ interface: Control of oxygen vacancies", Journal of Applied Physics **117**, 105302–115303 (2015).

[117]D. Fuchs, A. Sleem, R. Schäfer, A. G. Zaitsev, M. Meffert, D. Gerthsen, R. Schneider, and H. v. Löhneysen, "Incipient localization of charge carriers in the two-dimensional electron system in $LaAlO_3/SrTiO_3$ under hydrostatic pressure", Physical Review B **92**, 155313 (2015).

[118]J. L. M. Van Mechelen, D. Van Der Marel, C. Grimaldi, A. B. Kuzmenko, N. P. Armitage, N. Reyren, H. Hagemann, and I. I. Mazin, "Electron-phonon interaction and charge carrier mass enhancement in $SrTiO_3$", Physical Review Letters **100**, 7–10 (2008).

[119]D. van der Marel, J. L. M. van Mechelen, and I. I. Mazin, "Common Fermi-liquid origin of T-squared resistivity and superconductivity in n-type $SrTiO_3$", Physical Review B **84**, 205111 (2011).

[120]P. A. Lee and T. V. Ramakrishnan, “Disordered electronic systems”, Reviews of Modern Physics **57**, 287–337 (1985).

[121]M. Ben Shalom, M. Sachs, D. Rakhmilevitch, A. Palevski, and Y. Dagan, “Tuning Spin-Orbit Coupling and Superconductivity at the $SrTiO_3/LaAlO_3$ Interface: A Magnetotransport Study”, Physical Review Letters **104**, 126802 (2010).

[122]L. Kang, B. H. Lee, W.-J. Qi, Y. Jeon, R. Nieh, S. Gopalan, K. Onishi, and J. C. Lee, “Electrical characteristics of highly reliable ultrathin hafnium oxide gate dielectric”, IEEE Electron Device Letters **21**, 181–183 (2000).

[123]X. D. Huang, J. K. O. Sin, and P. T. Lai, “Fluorinated $SrTiO_3$ as Charge-Trapping Layer for Nonvolatile Memory Applications”, IEEE Transactions on Electron Devices **58**, 4235–4240 (2011).

[124]X. D. Huang, P. T. Lai, L. Liu, and J. P. Xu, “Nitrided $SrTiO_3$ as charge-trapping layer for nonvolatile memory applications”, Applied Physics Letters **98**, 242905 (2011).

[125]Z. Q. Liu, D. P. Leusink, X. Wang, W. M. Lü, K. Gopinadhan, A. Annadi, Y. L. Zhao, X. H. Huang, S. W. Zeng, Z. Huang, A. Srivastava, S. Dhar, T. Venkatesan, and Ariando, “Carrier freeze-out induced metal-insulator transition in oxygen deficient $SrTiO_3$ films”, Physical Review Letters **107**, 146802 (2011).

[126]S. Seri, M. Schultz, and L. Klein, “Thermally activated recovery of electrical conductivity in $LaAlO_3/SrTiO_3$”, Physical Review B **87**, 125110 (2013).

[127]J. H. Barrett, “Dielectric Constant in Perovskite Type Crystals”, Physical Review **86**, 118–120 (1952).

[128]J. K. Hulm, “The dielectric properties of some alkaline earth titanates at low temperatures”, Proceedings of the Physical Society. Section A **63**, 1184 (1950).

[129]C. Guguschev, D. Klimm, F. Langhans, Z. Galazka, D. Kok, U. Juda, and R. Uecker, “Top-seeded solution growth of $SrTiO_3$ crystals and phase diagram studies in the SrO-TiO_2 system”, CrystEngComm **16**, 1735–1740 (2014).

[130]P. Gumbsch, S. Taeri-Baghbadrani, D. Brunner, W. Sigle, and M. Rühle, “Plasticity and an inverse brittle-to-ductile transition in strontium titanate”, Phys. Rev. Lett. **87**, 085505 (2001).

[131]P. Brinks, W. Siemons, J. E. Kleibeuker, G. Koster, G. Rijnders, and M. Huijben, “Anisotropic electrical transport properties of a two-dimensional electron gas at $SrTiO_3$–$LaAlO_3$ interfaces”, Applied Physics Letters **98**, 242904 (2011).

[132]Z. Q. Liu, D. P. Leusink, X. Wang, W. M. Lü, K. Gopinadhan, A. Annadi, Y. L. Zhao, X. H. Huang, S. W. Zeng, Z. Huang, A. Srivastava, S. Dhar, T. Venkatesan, and Ariando, “Metal-Insulator Transition in $SrTiO_{3-x}$ Thin Films Induced by Frozen-Out Carriers”, Physical Review Letters **107**, 146802 (2011).

[133]H. Nakamura, T. Koga, and T. Kimura, “Experimental Evidence of Cubic Rashba Effect in an Inversion-Symmetric Oxide”, Physical Review Letters **108**, 206601 (2012).

[134]Y. Kim, R. M. Lutchyn, and C. Nayak, “Origin and transport signatures of spin-orbit interactions in one- and two-dimensional $SrTiO_3$-based heterostructures”, Physical Review B - Condensed Matter and Materials Physics **87**, 1–11 (2013).

[135]P. Schütz, F. Pfaff, P. Scheiderer, Y. Z. Chen, N. Pryds, M. Gorgoi, M. Sing, and R. Claessen, “Band bending and alignment at the spinel/perovskite $\gamma-Al_2O_3/SrTiO_3$ heterointerface”, Phys. Rev. B **91**, 165118 (2015).

[136]A. Joshua, J. Ruhman, S. Pecker, E. Altman, and S. Ilani, “Gate-tunable polarized phase of two-dimensional electrons at the $LaAlO_3/SrTiO_3$ interface.”, Proceedings of the National Academy of Sciences of the United States of America **110**, 9633–8 (2013).

[137]Z. Wang, Z. Zhong, X. Hao, S. Gerhold, B. Stöger, M. Schmid, J. Sánchez-Barriga, A. Varykhalov, C. Franchini, K. Held, and U. Diebold, “Anisotropic two-dimensional electron gas at $SrTiO_3$ (110)”, Proceedings of the National Academy of Sciences **111**, 3933–3937 (2014).

[138]H. J. H. Ma, J. Zhou, M. Yang, Y. Liu, S. W. Zeng, W. X. Zhou, L. C. Zhang, T. Venkatesan, Y. P. Feng, and Ariando, “Giant crystalline anisotropic magnetoresistance in nonmagnetic perovskite oxide heterostructures”, Physical Review B **95**, 155314 (2017).

[139]A. Kawabata, “On the Field Dependence of Magnetoresistance in Two-Dimensional Systems”, Journal of the Physical Society of Japan **53**, 3540–3544 (1984).

[140]M. I. Dyakonov, “Magnetoconductance due to weak localization beyond the diffusion approximation: The high-field limit”, Solid State Communications **92**, 711–714 (1994).

[141]A. Zduniak, M. Dyakonov, and W. Knap, “Universal behavior of magnetoconductance due to weak localization in two dimensions”, Physical Review B - Condensed Matter and Materials Physics **56**, 1996–2003 (1997).

[142]K. Wolff, R. Eder, R. Schäfer, R. Schneider, and D. Fuchs, “Anisotropic electronic transport and Rashba effect of the two-dimensional electron system in (110) $SrTiO_3$-based heterostructures”, http://arxiv.org/abs/1803.02646 (2018).

[143]Z. Zhong, A. Tóth, and K. Held, “Theory of spin-orbit coupling at $LaAlO_3/SrTiO_3$ interfaces and $SrTiO_3$ surfaces”, Phys. Rev. B **87**, 161102 (2013).

---

[144] A. D. Caviglia, S. Gariglio, N. Reyren, D. Jaccard, T. Schneider, M. Gabay, S. Thiel, G. Hammerl, J. Mannhart, and J.-M. J.-M. Triscone, “Electric field control of the $LaAlO_3$/$SrTiO_3$ interface ground state.”, Nature **456**, 624–627 (2008).

[145] M. Ben Shalom, a. Ron, a. Palevski, and Y. Dagan, “Shubnikov-de Haas oscillations in $SrTiO_3$/$LaAlO_3$ interface”, Physical Review Letters **105**, 1–4 (2010).

A. Appendix

A.1. Anisotropic electronic transport of (001)-oriented AO/STO heterostructures

Table A.1.: Fitting parameters for anisotropy by step edges and dislocations in (001) AO/STO for $T = 5\,\mathrm{K}$ according to Equation 3.3.

sample	r_0 (Ω)	r_d (Ω)	r_t (Ω)	w$_t$ (nm)	ω_c (°)
MJ2465a/b	632.83	0	145.24	45	135
MJ2466a/b	681.28	0	144.53	45	45
B290	909.00	516.05	129.00	120	85
B291	1088.00	207.00	77.00	190	35
B338a	869.68	211.63	0.00	200	0
B338b	814.81	14.78	48.43	200	90

Table A.2.: Fitting parameters for $R(T)$ according to Equation 3.2 for (001) AO/STO.

	bridge	A (Ω/K^2)	T_A (K)	T_0 (K)	T_1 (K)	B (Ω/K^2)
B290	A	0.35	20.69	-51.45	24.22	0.13
	B	0.29	21.67	-59.55	24.51	0.14
	C	0.26	22.44	-66.27	25.13	0.14
	D	0.28	22.11	-61.11	24.92	0.13
	E	0.40	24.26	-37.75	34.36	0.10
B291	A	0.21	23.65	-62.07	26.23	0.10
	B	0.21	23.54	-64.74	26.15	0.10
	C	0.18	24.45	-70.50	27.01	0.10
	D	0.15	25.61	-76.87	28.11	0.10
	E	0.17	25.80	-72.32	28.33	0.09
B338a	C	0.44	16.40	-35.38	18.26	0.10
	D	0.35	18.76	-41.89	21.18	0.10
	E	0.35	18.87	-41.88	21.30	0.10
	F	0.34	19.28	-42.98	21.68	0.11
	G	0.25	23.10	-54.38	25.50	0.10
B338b	C	0.44	16.40	-35.38	18.26	0.10
	D	0.35	18.76	-41.89	21.18	0.10
	E	0.35	18.87	-41.88	21.30	0.10
	F	0.34	19.28	-42.98	21.68	0.11
	G	0.25	23.10	-54.38	25.50	0.10
MJ2465a	A	0.19	18.33	-45.87	22.78	0.20
	C	0.22	19.81	-35.51	28.74	0.21
	E	0.17	20.07	-45.55	30.16	0.20
MJ2465b	C	0.16	20.93	-64.34	23.52	0.16
	F	0.19	19.65	-54.51	22.25	0.16
	G	0.14	23.34	-67.99	26.21	0.16
MJ2466a	A	0.14	23.43	-60.21	26.39	0.20
	C	0.15	23.75	-60.95	26.71	0.22
	E	0.08	24.88	-73.30	27.96	0.16
MJ2466b	C	0.14	22.05	-72.84	24.78	0.18
	F	0.13	23.47	-74.42	26.42	0.21
	G	0.19	20.41	-55.33	22.92	0.19

Table A.3.: Fitting parameters for WAL at $T = 2\,\mathrm{K}$ according to Equation 3.6 for (001) AO/STO.

		B_i (mT)	B_{so} (mT)	γ (-)
B290	A	79.99	963.76	0.10
	B	77.59	1138.38	0.10
	C	85.59	2016.84	0.11
	D	80.09	1511.88	0.10
	E	70.79	480.88	0.10
B291	A	76.32	1336.37	0.10
	B	79.35	1600.01	0.10
	C	82.76	1634.07	0.11
	D	81.88	1269.14	0.11
	E	77.23	786.51	0.10
B338a	C	74.55	388.41	0.11
	D	53.17	308.86	0.09
	E	51.73	433.25	0.08
	F	57.44	394.42	0.10
	G	70.00	364.59	0.10
B338b	C	56.16	363.77	0.09
	D	53.09	359.85	0.09
	E	54.48	376.73	0.09
	F	55.69	344.53	0.09
	G	52.95	364.94	0.09
MJ2465a	A	32.12	486.31	0.07
	C	26.77	440.33	0.06
	E	32.91	452.42	0.07
MJ2465b	C	48.01	631.23	0.08
	F	43.25	555.56	0.08
	G	44.71	786.81	0.08
MJ2466a	A	44.62	790.21	0.08
	C	45.31	760.51	0.08
	E	26.25	1033.37	0.06
MJ2466b	C	48.49	710.48	0.08
	F	47.87	667.89	0.08
	G	33.58	365.55	0.07

A.2. Anisotropic electronic transport of (110)-oriented AO/STO heterostructures

Table A.4.: Fitting parameters for $R(T)$ according to Equation 3.2 for (110) AO/STO for $T \leq 80\,\mathrm{K}$.

	bridge	A (Ω/K^2)	T_A (K)	T_0 (K)	T_1 (K)	B (Ω/K^2)
B297	A	0.60	24.53	-40.97	36.73	0.11
	B	0.68	26.01	-33.77	41.46	0.07
	C	0.75	25.71	-30.23	40.75	0.02
	D	0.88	19.84	-30.63	26.23	0.00
	E	0.85	18.48	-32.48	22.94	0.00

Table A.5.: Fitting parameters for WAL at $T = 2\,\mathrm{K}$ according to Equation 3.6 for (110) AO/STO.

	bridge	B_i (mT)	B_{so} (mT)	γ (-)
B297	A	0.18	1.52	0.00
	B	0.17	1.56	0.00
	C	0.16	1.72	0.00
	D	0.15	2.18	0.00
	E	0.14	2.93	0.00

A.3. Anisotropic electronic transport of (111)-oriented AO/STO heterostructures

Table A.6.: Fitting parameters for $R(T)$ according to Equation 3.2 for (111) AO/STO for $T \leq 100\,\mathrm{K}$.

	bridge	A (Ω/K^2)	T_A (K)	T_0 (K)	T_1 (K)	B (Ω/K^2)
B296	A	0.70	21.37	-122.28	23.98	0.00
	B	0.74	21.25	-116.05	23.83	0.00
	C	0.72	21.46	-114.83	24.02	0.00
	D	0.68	21.42	-120.27	23.93	0.00
	E	0.74	21.00	-112.37	23.48	0.00

Table A.7.: Fitting parameters for WAL at $T = 2\,\mathrm{K}$ according to Equation 3.6 for (111) AO/STO.

	bridge	B_i (mT)	B_{so} (mT)	γ (-)
B296	A	287.20	1389.97	1.42
	B	296.18	1499.36	1.50
	C	292.80	1434.81	1.42
	D	291.53	1415.86	1.44
	E	279.48	1204.61	1.29

Acknowledgments

At the end of this PhD thesis, I want to express my gratitude and thanks to:

Dr. Dirk Fuchs, for being a great supervisor and for the support during this thesis, for his patience, motivations and scientific guidance.

Prof. Dr. H. v. Löhneysen, for granting me this opportunity of doing research at the IFP and for being the first reviewer and his helpful remarks.

Prof. Dr. M. le Tacon, for his continuing support at the IFP and for being the co-reviewer and for the valuable comments.

Dr. R. Eder who performed the LCAO calculations and can make the most complicated things sound easy.

Dr. R. Schäfer for the many fruitful discussions on electronic transport.

Dr. R. Schnneider for the nice atmosphere in the weekly group meetings.

M. Meffert and Prof. Dr. D. Gerthsen (LEM) for the TEM characterization of the samples.

The workshops for their help with the liquid helium supply.

I also thank the old master and the gnomes, for all the discussions on and off physics and their company.

Finally, I am grateful for my wife Franziska, for her support, for her constructive remarks, for her patience and for everything.

So long, and thanks for all the fish.